https://lib.uliege.be https://matheo.uliege.be

Master thesis and internship[BR]- Master's Thesis : Coupling of a single-mode fiber with a deformable mirror in a space-based nulling interferometer[BR]- Internship (linked to master's thesis)

Auteur : Aït Hocine, Farouk
Promoteur(s) : Loicq, Jerome
Faculté : Faculté des Sciences appliquées
Diplôme : Master en ingénieur civil en aérospatiale, à finalité spécialisée en "aerospace engineering"
Année académique : 2019-2020
URI/URL : http://hdl.handle.net/2268.2/10470

Avertissement à l'attention des usagers :

Tous les documents placés en accès ouvert sur le site le site MatheO sont protégés par le droit d'auteur. Conformément aux principes énoncés par la "Budapest Open Access Initiative"(BOAI, 2002), l'utilisateur du site peut lire, télécharger, copier, transmettre, imprimer, chercher ou faire un lien vers le texte intégral de ces documents, les disséquer pour les indexer, s'en servir de données pour un logiciel, ou s'en servir à toute autre fin légale (ou prévue par la réglementation relative au droit d'auteur). Toute utilisation du document à des fins commerciales est strictement interdite.

Par ailleurs, l'utilisateur s'engage à respecter les droits moraux de l'auteur, principalement le droit à l'intégrité de l'oeuvre et le droit de paternité et ce dans toute utilisation que l'utilisateur entreprend. Ainsi, à titre d'exemple, lorsqu'il reproduira un document par extrait ou dans son intégralité, l'utilisateur citera de manière complète les sources telles que mentionnées ci-dessus. Toute utilisation non explicitement autorisée ci-avant (telle que par exemple, la modification du document ou son résumé) nécessite l'autorisation préalable et expresse des auteurs ou de leurs ayants droit.

Coupling of a single-mode fiber with a deformable mirror in a space-based nulling interferometer

Aït Hocine Farouk

Thesis presented for the degree of
Master in Aerospace Engineering

Faculty of Applied Sciences
University of Liege
Academic year 2019-2020

Coupling of a single-mode fiber with a deformable mirror in a space-based nulling interferometer

Aït Hocine Farouk

Abstract

This master thesis is dedicated to the design of single mode fibers (SMF) installed in a spaced-based nulling interferometer working in the infrared region. The SMF is used as a spatial filter in order to relax the requirements on the wavefront quality that an adaptive system needs to achieve. For this purpose a mathematical model of the coupling efficiency is developed and numerical simulations are performed. The effect of static aberrations on the performance of the fiber is analysed as well as the effect of non-common path aberrations. Finally, the effect of phase correction by a deformable mirror is analysed.

Acknowledgements

First, I would like to thank Jérôme Loicq for the time dedicated to this master thesis. Thank you for the trust placed in me and for your continuous support.

Then, I would like to thank Colin Dandumont for beeing available to answer my questions.

Also, I would like to thank my friends who supported me during all these years. Thank you Neil for beeing there every time i needed. Thank you Adrien for reviewing my thesis.

Finally I would like to thank my family who always believed in me. Thank you mom and dad for everything you did for me.

Contents

1 Introduction

2 Nulling interferometry: State of the art **1**

2.1 Detection of exoplanet 1

2.2 Infrared observation 2

2.3 Why observing in space ? 5

2.4 Interferometers 7

2.4.1 Nulling interferometers 8

2.4.2 Interferometer rotation 10

2.4.3 Geometric stellar leakage 11

2.4.4 Instrumental stellar leakage 12

2.5 Modal filtering by a single mode fiber 13

2.5.1 Relaxation of the requirements 14

2.6 Coupling efficiency 14

2.7 Deformable mirror for space application 15

2.7.1 Principles of adaptive/active optic 16

2.7.2 MEMS DMs 17

2.7.3 Monomorphe deformable mirrors 19

2.8 Thesis objectives 20

3 Fundamental concepts about imaging optics **22**

3.1 Propagation of light 23

3.1.1 Scalar diffraction theory 23

3.1.2 Helmholtz equation 23

3.1.3 Rayleigh-Sommerfeld solution 24

3.1.4 Fresnel approximation 25

3.1.5 Fraunhofer diffraction 26

3.2 Diffraction-limited optics 26

3.2.1 Imaging system 27
3.2.2 Concept of coherence and application in stellar interferometry 27
3.2.3 Coherent illumination 29
3.2.4 Incoherent illumination 30
3.2.5 Resolution criterion 30
3.3 Aberration theory 31
3.3.1 Sources of aberrations in space 31
3.3.2 Generalized pupil function 33
3.3.3 Strehl ratio 34
3.3.4 Zernike circle polynomials 35

4 Single mode fiber 39
4.1 Guiding light principle 39
4.2 Materials selection 41
4.3 Applications 41
4.4 LP modes 41
4.5 Single mode fibers 43
4.5.1 Numerical aperture 44
4.5.2 Normalized frequency 45
4.6 LP_{01} profile 45
4.6.1 General expression 45
4.6.2 Gaussian approximation 46

5 Optical system 48
5.1 Waveband 48
5.2 Telescope configuration 48
5.3 Coupling efficiency 50

6 Diffraction limited design 55
6.1 General considerations 55
6.1.1 Point spread function 55
6.1.2 Electric field 56
6.1.3 Coupling efficiency 59
6.2 Design of the f-number 61
6.2.1 Case 1: the core radius is variable 62
6.2.2 Case 2: the core radius is fixed 65
6.3 Conclusion 68

7 Study of static aberrations **69**
7.1 Effect of the aberration's strength 69
7.1.1 Piston 70
7.1.2 Tip/Tilt 70
7.1.3 Defocus and spherical aberrations 72
7.1.4 Coma aberrations 74
7.1.5 Astigmatism aberrations 77
7.1.6 Other types of aberrations 77
7.1.7 Conclusion 77
7.2 Effect of the obstruction 81
7.3 Effect of the wavelength 85
7.4 Non-common path aberrations and their correction 87

8 Conclusion **90**

List of Figures

2.1 Cumulative detections per year [2]. 2
2.2 Gemini Planet Imager at Gemini South Observatory in Cerro Pachon, Chilie. Photo by J. Chilcote [5]. 3
2.3 Picture of 51 Eridani taken by Gemini Planet Imager [6]. 3
2.4 SPHERE in the assembly laboratory at IPAG with all instruments integrated [7]. 4
2.5 Predicted planet/star flux ratios versus wavelength. The flux ratio is dominated by reflection in the optical (Rayleigh scattering and clouds), and by emission in the infrared. Complete description of these graphs is presented in [9]. 5
2.6 Effect of a turbulent atmosphere on the resolution when the diameter D increases. $r_0 = 10$ cm. 6
2.7 Atmospheric opacity in function of the wavelength. 6
2.8 Principle of inteferometry: two telescopes separated by a baseline of length B are equivalent to a telescope with a diameter B [12]. 7
2.9 VLT array in Chile. 8
2.10 Schematic view of a Bracewell nulling interferometer [60]. The interferometer consists of two pupils collecting the light and a system that transport the light in two different arms where a phase shift of π is introduced to get the desired transmitted map. 9
2.11 Gometrical configuration of the interferometer and the exoplanet system. The position of the planet is given by the coordinates (θ, α)[17]. 10
2.12 Modulation of the planet signal thanks to the rotation of the nulling interferometer [22] 11

2.13 Representation of an adaptive system. The light from the telescope reachs a deformable mirror. Then, a part of the light is sent to the wavefront sensor thanks to a beamsplitter. The wavefront sensor measures the aberration of the wavefront and the control system deforms the mirror to compensate the aberration. 16
2.14 MEMS DM concept. The intermediate diaphragm is locally deformed by the action of the electric force generated by the electrode. Then the deformation is transmitted to the membrane mirror by the attachment post [24]. 17
2.15 PICTURE optical layout [26]. 18
2.16 Boston Micromachines Mini DM with 140 actuators [24]. 18
2.17 DeMi CubeSat deployed from the International Space Station on 13 July 2020 (image credit: NASA) 19
2.18 Unimorph mirror concept. The disk of piezoelectric ceramics is deformed when a voltage is applied to the electrodes. The optical plane is deformed due to transverse piezoelectric effect of the piezoelectric disk [28]. 19
2.19 The CILAS 188 actuators bimorph mirror installed in the 8.2 m Subaru telescope [28]. 20
2.20 Timeline of the development of space-based interferometry missions [32]. 20
2.21 Representation of the single mode fiber at the focus of a telescope. D is the aperture of the telescope. f the focal length. E_B the electric field of the incoming light and F_B the electric field of the fundamental mode of the SMF. 21

3.1 Propagation geometry [49]. 25
3.2 Basic model of an imaging system [51]. 27
3.3 Principle of visibility. (defrere lecture) 28
3.4 Point spread function of a circular aperture. The figure is known as Airy pattern. 31
3.5 Rayleigh criterion [55]. 31
3.6 Thermal loads on a spacecraft orbiting around the Earth. 32
3.7 State of art of small pointing accuracy [32]. 33

3.8 Wavefront aberration function. The ideal wavefront defining a diffraction limited system is the spherical reference surface. The wavefront aberration function Φ at point is the difference between the aberrated wavefront and the surface. 34
3.9 38

4.1 Incident light ray is first refracted in the core and then undergoes multiple total internal reflections at the core–cladding interface. This occurs for $\theta < \theta_{max}$ defining the acceptance cone [33] 40
4.2 Schematic view of a step-index fiber. 40
4.3 Electric field amplitude profiles for all the guided modes of a step-index fiber. The two colors indicate different signs of the electric field values [34]. 43
4.4 Normalized electric field distribution for a step index fiber at the normalized frequency V=2.2. The solid line is the exact electric field distribution. The dashed line represents the Gaussian approximation with $\omega_G/a = 1.162$. ω_G is the mode radius and q is the radial coordinate [31]. 47

5.1 Representation of FKSI. Two telescopes of diameter 0.5 m separated by a distance of 12.5 m [53]. 49
5.2 Hubble Space Telescope (HST) [57] 49
5.3 DeMi optical design with ray trace overlaid in red for the DeMi mission (image credit: DeMi Team). 50
5.4 Schematic view of a single mode fiber at the focus of a telescope. E_A is the incoming electric field at the aperture, F_A the back-propagated fundamental mode of the SMF, E_B the electric field at the focus of the telescope, F_B the electric field of the fundamental mode of radius ω_0. D_1 represents the diameter of the aperture and D_2 the diameter of a central obstruction typical of a Cassegrain telescope. 52

6.1 PSF representations at focal distance $f = 3.83$ m for a primary mirror $D = 1$ m with no obstruction $\alpha = 0$ at the observing wavelength $\lambda = 5$ μm. 56
6.2 PSF representations at focal distance $f = 4.48$ m for an aperture $D = 1$ m with a central obstruction $\alpha = 0.436$ at the observing wavelength $\lambda = 5$ μm. 57

6.3 PSF normalized by the pic value of the unobstructed PSF in function of the radial distance. $\lambda = 5\ \mu m$, $D = 1\ m$. $f = 3.83\ m$ for $\alpha = 0$ and $f = 4.48\ m$ for $\alpha = 0.436$. 58
6.4 Comparison between the normalized electric field at the focus of the telescope E_B and the normalized mode of the fiber LP_{01} in function of the radial distance. $\alpha = 0$, $f = 3.83\ m$, $\omega_0 = 13.7\ \mu$m, $\lambda = 5\ \mu$m, $D = 1\ m$. The mismatch of the two profiles explains the loss of energy at the output of the fiber. 58
6.5 Coupling efficiency in function of β for different value of the obstruction α. 59
6.6 Value of β that maximizes the coupling efficiency in function of the central obstruction. 60
6.7 Optimum coupling efficiency in function of the central obstruction at cutoff frequency 61
6.8 Optimum core radius in function of wavelength 62
6.9 Coupling efficiency in function of the f number for different value of the obstruction α. 64
6.10 Optimum f-number in function of the central obstruction. 64
6.11 Optimum f-number in function of the wavelength λ for different value of the obstruction α. 66
6.12 Coupling efficiency in function of wavelength for different values of the obstruction α. 67

7.1 Comparison of the PSF of unobstructed circular pupil when the system is not aberrated and aberrated by a tilt. The only effect of the tilt is to shift the PSF. 70
7.2 Normalized coupling efficiency in function of the RMS wavefront error for horizontal tilt. 71
7.3 Normalized coupling efficiency in function of the RMS wavefront error for horizontal and vertical tilt. 71
7.4 Comparison of the PSF of unobstructed circular pupil when the system has a defocus and a spherical aberration. The two PSF preserve their symmetry. 72
7.5 Normalized coupling efficiency in function of the RMS wavefront error for defocus and spheric aberration. 73

7.6 Comparison of the PSF of unobstructed circular pupil when the system has a defocus and a spherical aberration. The two PSF preserve their symmetry. 75
7.7 Normalized coupling efficiency in function of the RMS wavefront error for horizontal coma and 2nd-order coma. 75
7.8 Normalized coupling efficiency in function of the RMS wavefront error for 2nd-order coma. 76
7.9 Comparison of the PSF of unobstructed circular pupil when the system has oblique astigmatism and vertical 2nd-order astigmatism. 77
7.10 Normalized coupling efficiency in function of the RMS for oblique astigmatism and vertical 2nd-order astgmatism. 78
7.11 Comparison of the PSF of unobstructed circular pupil when the system has a defocus and a spherical aberration. The two PSF preserve their symmetry. 79
7.12 Normalized coupling efficiency in function of the wavefront RMS error for oblique trefoil, quadrafoil and pentafoil. 80
7.13 Normalized coupling efficiency in function of the wavefront RMS error for different types of aberrations. 80
7.14 Normalized coupling efficiency in function of the wavefront RMS error for different types of aberrations and different values of the obstruction. 82
7.15 Normalized coupling efficiency in function of the central obstruction for different types of aberrations. The strength of the aberration is fixed to 1 rad. 83
7.16 Normalized coupling efficiency in function of the central obstruction for different types of aberrations and different values of wavefront RMS error. 84
7.17 Normalized coupling efficiency in function of the wavelength when $\sigma_{rms} = 1$ rad for different values of the central obstruction. 85
7.18 Normalized coupling efficiency in function of the wavelength when $\sigma_{rms} = 0.5$ rad for different values of the central obstruction. 86
7.19 Example of randomly generated Zernike coefficients for non common path aberrations. 87
7.20 Example of phase map for aberrations encountered in space. 88
7.21 Residual phase map after correction by a deformable mirror. A RMS wavefront error $\sigma_{rms} < 0.1$ rad is obtained when the first 115 Zernike polynomials are corrected. 89

List of Tables

3.1 Zernike circle polynomials. Noll ordering from radial mode 1 to 5. . . 37

4.1 Typical values of numerical aperture of single mode fiber. 44

6.1 Comparison of f-number 66

Chapter 1

Introduction

This master thesis is dedicated to the study of single mode fibers as spatial filter in a space-based nulling interferometer. They are used to decrease the requirements on the wavefront quality that an adaptive system needs to achieve.

First, the principles of nulling interferometry are described with an emphasis on the utility of the use of single mode fibers and deformable mirrors in space.

Next, the fundamentals concepts about imaging optics needed to understand the following work are presented. Concepts about propagation of light and the representations of aberrations will be widely used in this paper.

After that, the principles of single mode fiber are introduced. The condition to have a single mode fiber is presented and the profile of the fundamental mode LP_{01} is discussed.

Then, the optical system is defined. The telescopes configuration and the waveband of observation are discussed. Then a mathematical model of the coupling efficiency is developed.

Afterwards, simulations of the coupling efficiency are performed with Matlab in order to estimate the diffraction limited performances.

Finally, the system subjected to static aberrations is analysed and aberrations encountered in space are simulated. The chapter ends by a discussion on the performance of the system when a deformable mirror corrects some Zernike modes.

Chapter 2

Nulling interferometry: State of the art

2.1 Detection of exoplanet

In 1995 Mayor and Queloz discovered the first exoplanet orbiting around a star similar to the sun thanks to the 1.93 m telescope of the Haute Provence Observatory [1]. Since then, detections techniques improved significantly leading to many new discoveries each year. Today thousands exoplanets have been reported and humankind has never been that close to understand the origin of life.
In Figure 2.1 the cumulative detections per year and the associated detection technique are displayed.

Nowadays, 75% of known exoplanets have been found thanks to the transits method. This method takes advantage of the periodic decrease in luminosity of the parent star when its exoplanets is passing between the observer and the star. This is one of the indirect methods that leads to the detection without receiving direct photon from the planet. Others important indirect methods are: radial velocity and microlensing. Radial velocity is the method used by Mayor and Queloz to find 51 Pegasi b. This technique measures the perturbation of the star motion induced by the exoplanet graviting around. On the other hand microlensing technique is based on the general relativity concept that a light undergoes a deviation when a heavy body is on its path.

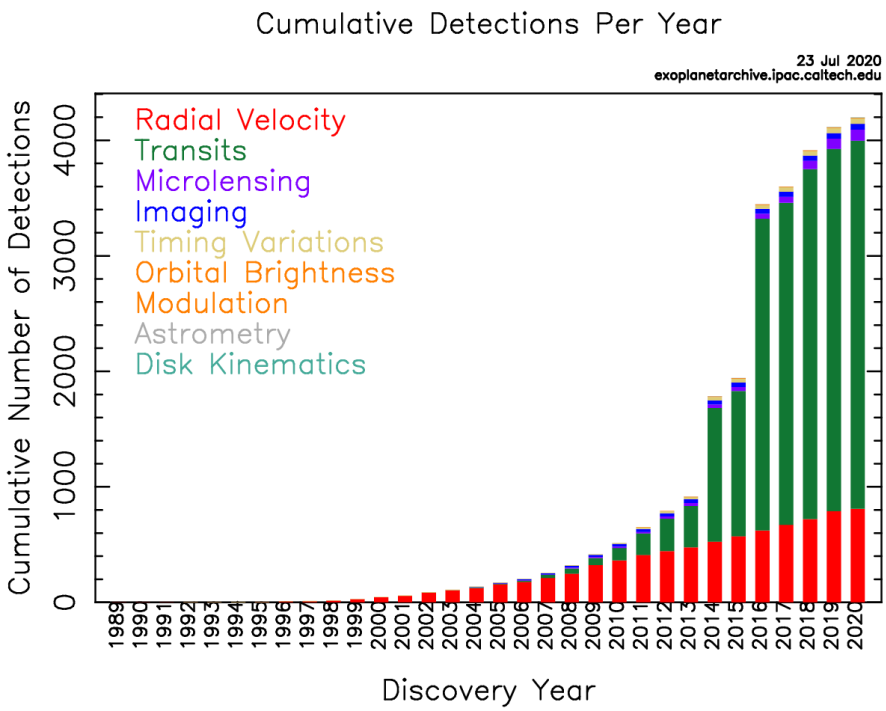

Figure 2.1: Cumulative detections per year [2].

2.2 Infrared observation

The main goal of exoplanet detection is finding habitable planets where life could exist. For this purpose astronomers look for gases like the one presents in our atmosphere by assuming that the condition of life would be the same anywhere in the universe. With this idea some molecules have an important interest for scientist. These molecules are: H_2O, CO_2 , O_3 , CH_4, and N_2O. Adding that these molecules have spectral emission in the mid-infrared region: 5-20 μm [3], it is admitted by all scientists that the observation in the infrared region is fundamental.

A first example of instrument working in the infrared is the Gemini Planet Imager (GPI). This is a high contrast imaging instrument installed on the 8.1-meter telescope at the Gemini South Observatory in Chile in 2013. It is designed specifically to detect young gas giants via their thermal emission in the near-infrared region [0.9-2.4] μm. The system includes a high-order adaptive optics system to correct in real time atmospheric turbulent effects, a coronagraph to suppress the light of the bright star, a calibration interferometer, and an integral field spectrograph which separates the light according to wavelength allowing the characterization of the atmosphere. The instrument is expected to detect exoplanets separated to their host star by 0.2-1

arcseconds [4].
In Figure 2.2 a picture of GPI mounted on the Gemini South Observatory.

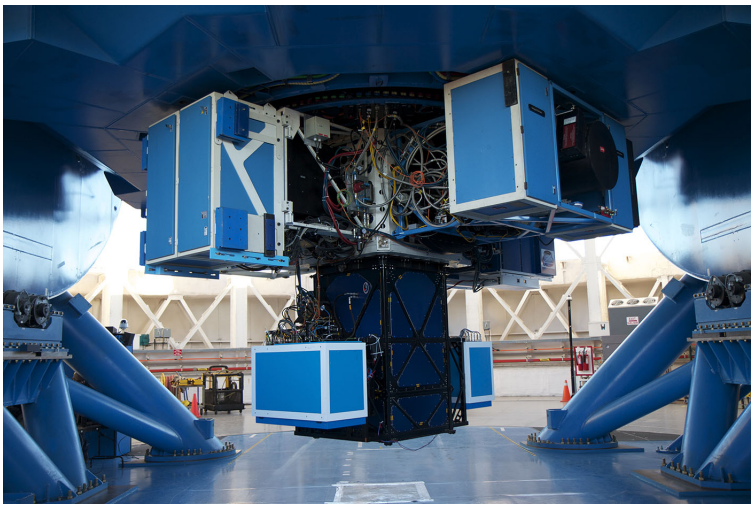

Figure 2.2: Gemini Planet Imager at Gemini South Observatory in Cerro Pachon, Chilie. Photo by J. Chilcote [5].

In August 2015 the young-jupiter planet 51 Eridani b is the first exoplanet discovered by GPI. Many others has been discovered since then. A picture of 51 Eridani b taken by GPI is shown in Figure 2.3.

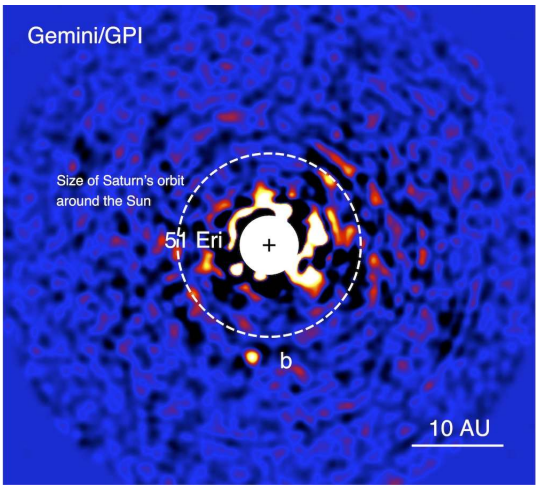

Figure 2.3: Picture of 51 Eridani taken by Gemini Planet Imager [6].

A second example of infrared telescope is the Spectro Polarimetric High contrast Exoplanet REsearch (SPHERE). It is an extreme adaptive optics system coupled with a coronagraph at the VLT. Its scientific goal is to image exoplanet systems and characterize them at optical and near-infrared wavelengths. The polarimetric differential imaging mode of SPHERE allows to isolate a dusty disc (or a planet) from the star. It is based on the principle that the light of the star is unpolarized while a reflected light on a obstacle, in that case, the disk, is polarized. This difference in polarization allows SPHERE to isolate the starlight from the reflected light [7]. In July 2017 SPHERE discovers its first exoplanet, HIP 65426 b.

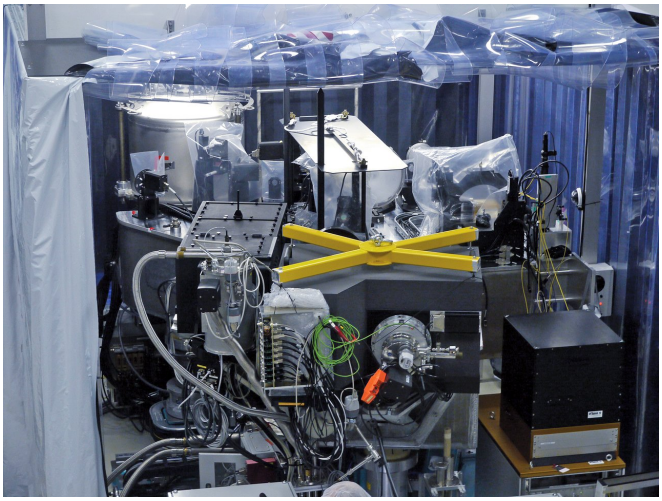

Figure 2.4: SPHERE in the assembly laboratory at IPAG with all instruments integrated [7].

Another argument in favor of observation in infrared region is the great advantage in term of contrast (star/planet flux ratio). Indeed, one major difficulty in the observation of exoplanets is the huge luminosity of the star that outshines the exoplanet. However, the contrast is wavelength dependant and one can take advantage of it to relax mission requirements. Typical Earth-Sun system has contrast in the order of 10^{10} in the visible and 10^{7} at 10 μm [8]. In Figure 2.5 a model that predicts planet/star flux ratios versus wavelength is displayed. It shows the wavelength dependency of the flux ratio and the decrease of it for wavelength bigger than 3 μm. A detail description of the graphs can be found in [9].

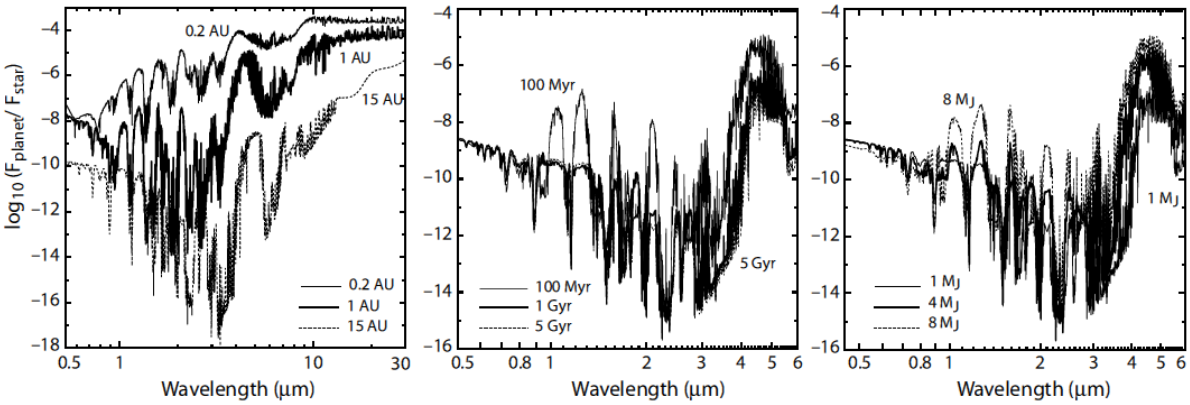

Figure 2.5: Predicted planet/star flux ratios versus wavelength. The flux ratio is dominated by reflection in the optical (Rayleigh scattering and clouds), and by emission in the infrared. Complete description of these graphs is presented in [9].

2.3 Why observing in space ?

Observing in the infrared from the ground is challenging for multiple reasons. First, the turbulence of the atmosphere blurs the image and limits the resolution. Indeed, without a system that corrects the fluctuations of the wavefront, images produced by any telescope is limited by the Fried parameter r_0. This parameter measures the quality of the optical transmission through the turbulent atmosphere. It is wavelength dependant and in a Kolmogorov turbulent model of the atmosphere, it is given by [10],[11]

$$r_0 \sim \lambda^{6/5} \tag{2.1}$$

Typical value of r_0 are 15 cm at good site in the visible and 1 m at 2 μm [9].

This parameter has the effect of decreasing the resolution of the telescope which was give by

$$\theta = 1.22\lambda/D \tag{2.2}$$

for a cicular aperture of diameter D at the wavelength λ.

Indeed, when looking at a star, the fluctuations of the refractive index in the atmosphere limit the resolution to a diameter $D = r_0$

$$\theta = 1.22\lambda/r_0 \tag{2.3}$$

Therefore, any telescope is not better than a one with a diameter of 20 cm. This is

only understandable when atmospheric effects are taken account since the resolution should increase with D according to Equation 2.2. The field of optic that studies the impact of the atmosphere on the propagation of light is called adaptive optic.

In Figure 2.6 the effect of r_0 on the image quality is represented. It shows that increasing the diameter of the telescope decreases the resolution. Blurring effect becomes important when $D = r_0 = 10$ cm. This effect is generally named the seeing.

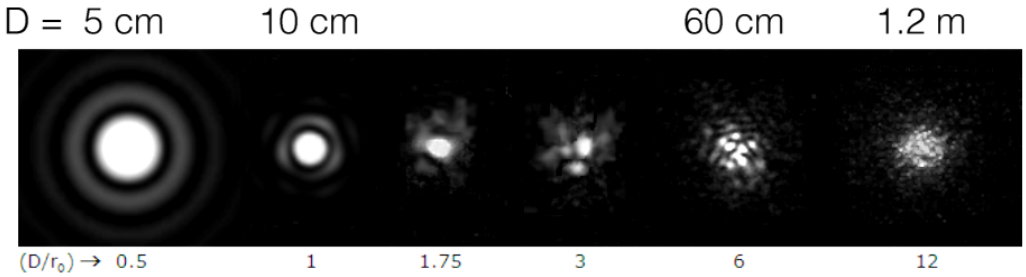

Figure 2.6: Effect of a turbulent atmosphere on the resolution when the diameter D increases. $r_0 = 10$ cm.

The second reason that limits observation from the ground is the opacity of the atmosphere. Indeed the atmosphere does not transmit all the light coming from a star. In fact, because of the molecular absorptions of H_2O and CO_2, the Earth's atmosphere can be considered opaque in the infrared. Therefore it is very difficult from the ground to make observations in this region. To overcome these issues, access to space seems mandatory [3].

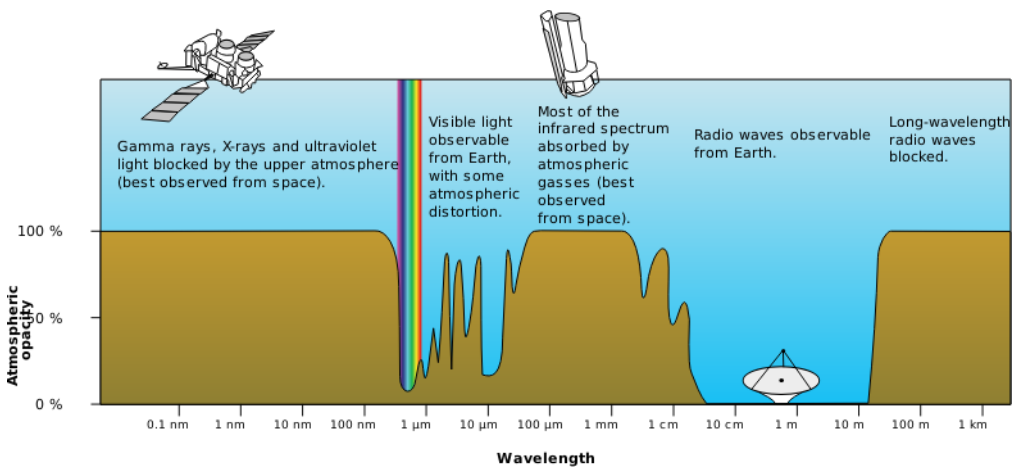

Figure 2.7: Atmospheric opacity in function of the wavelength.

2.4 Interferometers

Another difficulty when it comes to the detection of exoplanets is the star–planet angular separation $\Delta\theta$. Indeed exoplanets are very close to their parent star. Typically, their angular separation is $\sim$ 0.1 arcsec. It corresponds to a distance of 1 AU between the planet and the star seen from a distant of 10 pc. Such an angular separation would require an aperture of

$$D = 1.22\lambda/\Delta\theta \sim 25m \tag{2.4}$$

at the observing wavelength $\lambda = 10$ μm.

At the current time no telescope of this size exists. The largest telescope is the Large Binocular Telescope (LBT) with an effective aperture of 11.9 m. However some telescopes with extremely large aperture are under development. The Extremely Large Telescope (ELT), a telescope with a 39.3-m diameter, is expected for 2024.

A way to increase the spatial resolution, without increasing the diameter, is to use the principle of interferometery. The concept is based on Fizeau principle that says that two small apertures distant of B are equivalent to a single large aperture of diameter B.

The angular resolution of such a configuration is given by

$$\theta = \frac{\lambda}{2B} \tag{2.5}$$

with B, the distance between the two telescopes, named the baseline. In Figure 2.8 the principle of interferometry is represented. The combination of the light recolted at the two apertures gives the fringes of interference.

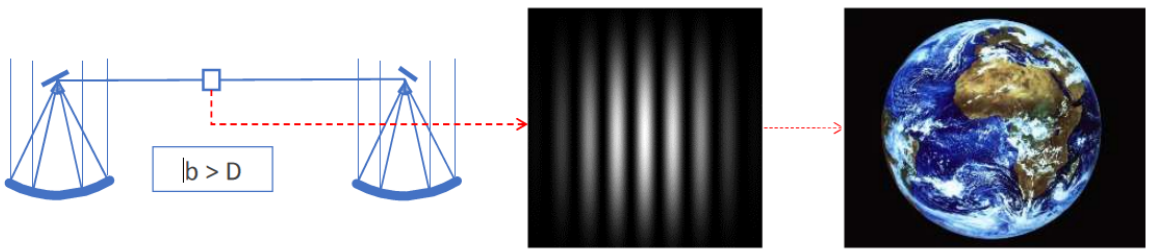

Figure 2.8: Principle of inteferometry: two telescopes separated by a baseline of length B are equivalent to a telescope with a diameter B [12].

One example of interferometer is the ESO Very Large Telescope Interferometer (VLTI) at Cerro Paranal in Chile. It consists of four VLT Unit Telescopes of 8 m and four moveable 1.8 m Auxiliary Telescopes. The VLTI provides milli-arcsec angular resolution at near and mid-infrared wavelengths over a 200-m baseline. The light recombination is performed by the PIONIER and GRAVITY instruments in the near infrared and by MATISSE in the mid-infrared [13].

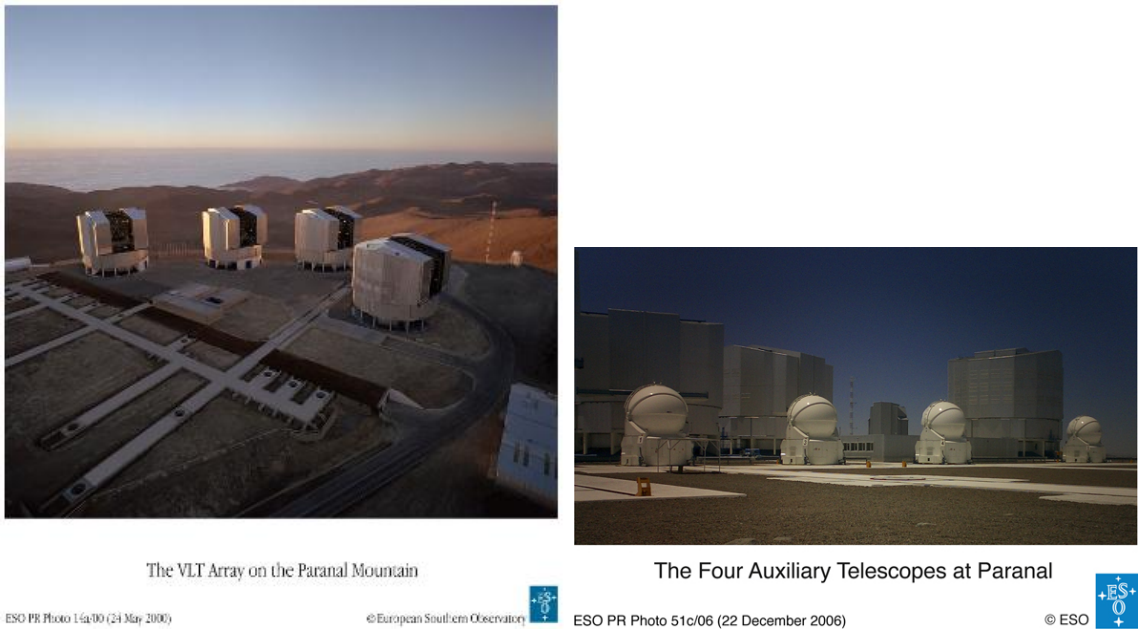

(a) The four Unit Telescopes. (b) The four Auxiliary Telescopes.

Figure 2.9: VLT array in Chile.

2.4.1 Nulling interferometers

In order to overcome the problem of the high contrast, a special interferometer, called the nulling interferometer, has been proposed by Bracewell in 1978 [14].

In the simple case of two identical telescopes pointing toward a star, with an null optical phase difference between the arms, the figure of interference is a succession of bright and dark fringes with the first bright fringe at the center of the transmission map (the detected intensity in function of the angular position [15]). Meanwhile, in a nulling interferometer, thanks to a phase shift of π introduced in one arm, the null occurs at the center of the transmission map. Then, if the length of the baseline is such that the OPD, resulting from the angular separation between the star and the exoplanet, equals $\lambda/2$, i.e a phase shift of π, the light of the planet recombines

constructively. Thereby, the planet is located on the first bright fringe of the transmission map. In this configuration, the starlight is extinguished destructively while the light of the exoplanet is transmitted to the detector. Therefore, a nulling interferometer solves the problem of the high contrast between a star and its exoplanet. In Figure 2.10 a schematic view of the Bracewell nulling interferometer is presented.

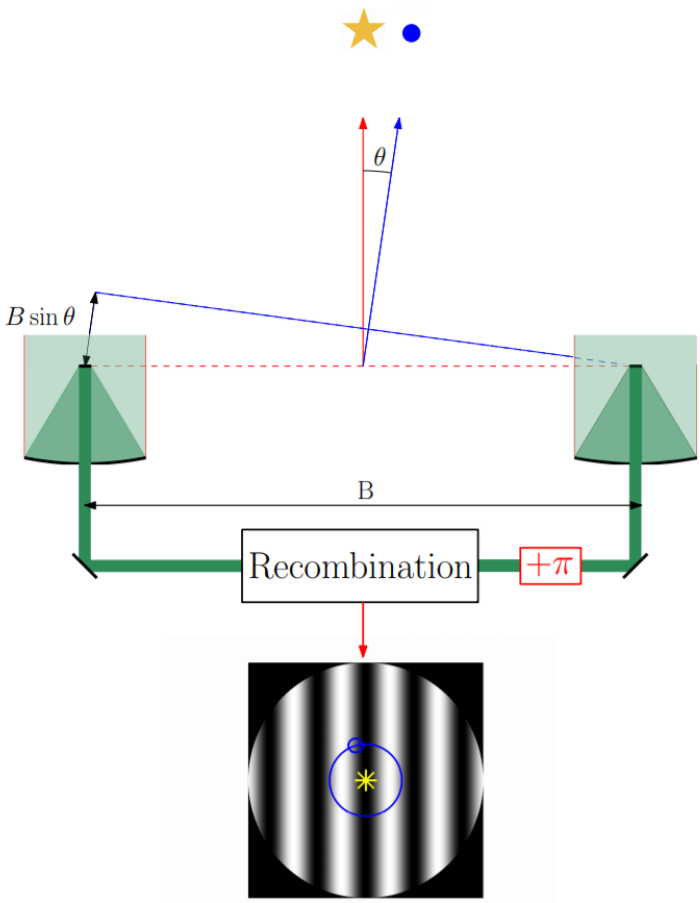

Figure 2.10: Schematic view of a Bracewell nulling interferometer [60]. The interferometer consists of two pupils collecting the light and a system that transport the light in two different arms where a phase shift of π is introduced to get the desired transmitted map.

The intensity response $R(\theta, \alpha)$ that defines the transmission map has been developed by many authors. According to the notation of Figure 2.12, assuming the two telescopes are of unitary size and each pupil collects the same amount of light, the intensity response is given by [17]

$$R(\theta, \alpha) = 2\sin^2\left(\pi\frac{b\theta}{\lambda}\cos\alpha\right) \tag{2.6}$$

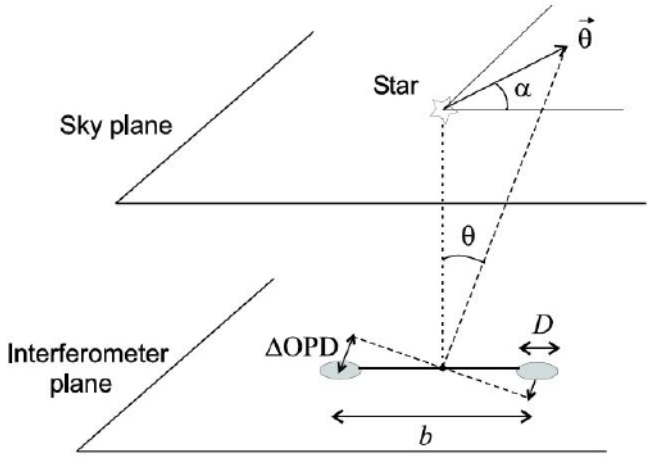

Figure 2.11: Gometrical configuration of the interferometer and the exoplanet system. The position of the planet is given by the coordinates (θ, α)[17].

2.4.2 Interferometer rotation

However, although the nulling interferometer allows to decrease the contrast, it is generally not possible to detect exoplanet in the infrared with a static array configuration. In fact, the signal of the planet is dominated by many other signals which compromises the detection. Such source of noises can be generated by the telescope itself (dark current, readout noise) or by the space environment. In the Solar system, a local zodiacal emission is present between the orbit of Mercury and Jupiter. It is generated by a dust at 300 K. For exoplanetary system, such a dust can also exists. It is named exozodiacal disk and also contributes to the noises.

For this reason, the nulling interferometer proposed by Bracewell is designed to rotate around its optical axis. Thanks to this rotation, the modulation of the signal of the planet can be performed by alternatively crossing the white and dark fringes in the transmission map while the stellar signal and the background emission remain constant. Thus, by synchronous demodulation, the signal of the planet can be retrieved [3].

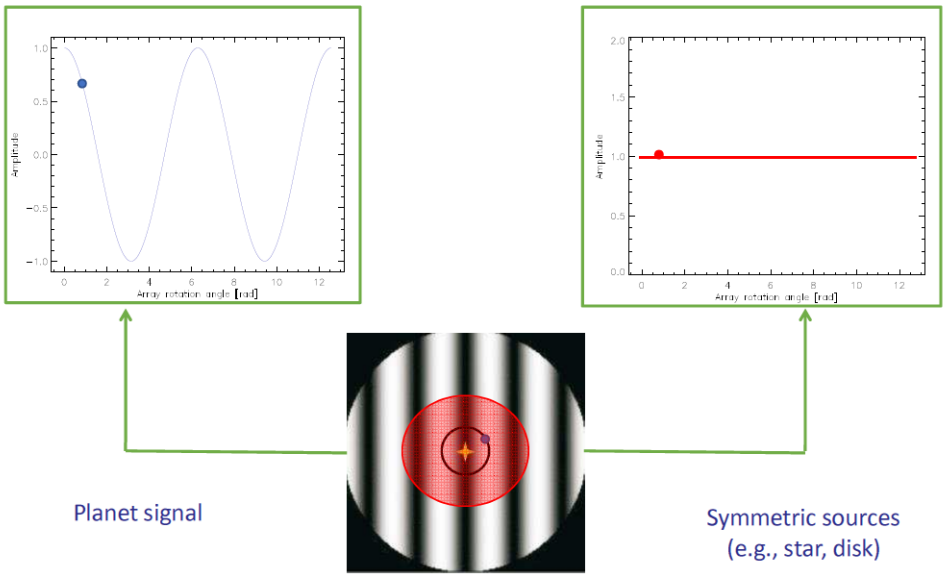

Figure 2.12: Modulation of the planet signal thanks to the rotation of the nulling interferometer [22]

2.4.3 Geometric stellar leakage

The performance of a nulling interferometer is described by its capability to suppress the light of the star at the center of the transmission map. Indeed, the expression of the transmission map Equation 2.6 can be approximated by

$$R(\theta, \alpha) \approx 2\left(\pi \frac{b\theta}{\lambda} \cos \alpha\right)^2 \tag{2.7}$$

for $\theta << \lambda/b$.

Therefore the null occurs only on the optical axis where $\theta = 0$. This has the consequence that even if the star is perfectly on the optical axis, the final extent of the stellar photosphere will result in a transmission of undesired light. This effect is called *geometric stellar leakage*.

One common way to evaluate the efficiency of the nuller is by defining the *nulling ratio* N defined as the ratio between the transmitted flux and the flux at the input of the beam combiner. Since the transmitted flux is generally equal to the total flux collected by the inteferometer, the definition is equivalent to the ratio between the destructive and constructive output:

$$N = \frac{I_{min}}{I_{max}} \tag{2.8}$$

For the case of the observation of a stellar photosphere at the observing wavelength λ with $\theta_\star$ its angular radius, the nulling ratio can be expressed as follows:

$$N = \frac{\pi^2}{4}(\frac{b\theta_\star}{\lambda}) \tag{2.9}$$

The *rejection ratio* is defined ρ as the inverse of the nulling ratio

$$\rho = \frac{1}{N} = \frac{I_{max}}{I_{min}} \tag{2.10}$$

2.4.4 Instrumental stellar leakage

However the geometrical leakage is not the only phenomenon which results in a transmission of undesired stellar light. Another effect which is not depending on photosphere diameter is what is called the *instrumental leakage*. This contribution comes from the mismatch between the beam of light reaching the different pupils. The source of this error can be the atmospheric turbulence for the case of an inteferometer on the ground, or the imperfections in the optics for a space interferometer.

Theses deviations from the ideal scenario result in the modification of the expression of the null ratio (or rejection ratio).
Autors had already investigated the effect of aberrations on the transmission map. Three main types of instrumental leakage have been recognized: phase error, intensity mismatch and polarization error [16].

Phase error

If a small phase error $\Delta\Phi$ exists between the two beams, the fringes are shifted in the transmission map resulting in a stellar leak at the center of the map, given by [18]

$$R(0,0) = \frac{\Delta\Phi^2(\lambda)}{4} \tag{2.11}$$

If the wavefronts coming from the two pupils are aberrated with a phase variance $\sigma^2_{\Phi_{1,2}}(\lambda)$, the center of the intensity map is given by [19]

$$R(0,0) = \frac{1}{4}\big(\sigma^2_{\Phi_1}(\lambda) + \sigma^2_{\Phi_2}(\lambda)\big) \tag{2.12}$$

Phase defects include pointing errors (represented by tip/tilt Zernike mode), low order optical aberrations like asphericity and higher spatial frequency defects like polishing errors.

Intensity mismatch

A mismatch in intensity between the two interferometric arms also results in a leak. If $\Delta I(\lambda)$ is the relative intensity between the two beams, the leak at the null is given by [18]

$$R(0,0) = \frac{\Delta I^2(\lambda)}{16} \tag{2.13}$$

The intensity mismatch can be due to inhomogeneous coatings or by the alteration of the coating [19].

Polarization error

Finally a polarization error brings a stellar leakage according to [46]

$$R(0,0) = \frac{1}{4}\big(\Delta\Phi^2_{s-p}(\lambda) + \alpha^2_{rot}(\lambda)\big) \tag{2.14}$$

where $\Delta\Phi_{s-p}$ is the differential s-p phase delay and α_{rot} the relative polarization rotation angle between the two beams.

2.5 Modal filtering by a single mode fiber

Since aberrations in the wavefront lead to an increase of the intensity at the center of the transmission map, the nulling ratio also varies.

If one telescope is considered free of aberration and the other with a small phase variance a_i^2 , the nulling ratio is given by [19]

$$N = \frac{a_i^2}{4} \tag{2.15}$$

Therefore, if the goal of the interferometer is to reach a null ratio of 10^{-5}, the standard deviation a_i (=RMS if the mean of the aberration equals 0) across the pupil has to satisfy

$$a_i < 6.3\ 10^{-3} \text{ radian} \tag{2.16}$$

which corresponds to a $\lambda/1000$ wavefront quality.

In conclusion, to achieve a nulling ratio of 10^{-5}, the interferometer needs to be free of aberration greater than $\lambda/1000$.

2.5.1 Relaxation of the requirements

In order to relax the requirements on the wavefront quality, Mennesson et al.[19] proposed to use single mode fibers (SMF) as spatial filter.

The principle of the use of a single mode fiber relies on the fact that, inside a single mode fiber, the shape of the electric field is constant during the propagation regardless the electric profile of the light injected. This profile is called the fundamental mode and has approximately the shape of a Gaussian. This mode is denoted LP_{01}. Therefore, any aberration at the input will be corrected at the output of the fiber in order to adopt the shape of the fundamental mode. Then, by putting a SMF at the focus of each telescope of the nulling interferomer, the lights will interfer coherently at the recombination stage leading to a better nulling ratio.

According to [19], if one pupil of the two telescopes is perfect and the other one has a small phase variance a_i^2, the nulling ratio is given by

$$N = \frac{a_i^4}{16} \tag{2.17}$$

Therefore to reach a nulling ratio of 10^{-5}, the standard deviation should satisfy

$$a_i < 0.11 \text{ rad} \tag{2.18}$$

which corresponds to a $\lambda/56$ wavefront quality.

In conclusion, the presence of a single mode fiber at the focus of a telescope decreases by twenty the requirements on the wavefront quality. The use of single mode fibers in a nulling interferometer is therefore of great interest.

2.6 Coupling efficiency

Unfortunately, the injection in a SMF comes with a drawback: a loss of energy. Indeed, when a light is injected in a single mode fiber, the energy at the input is not equal to the energy at the output. Part of the energy is distributed into the

fundamental mode while the other part is lost. In fact, no energy is lost in one particular case: when the light injected has exactly the profile of the fundamental mode.

This loss of energy, due to the mismatch between the electric field at the input and the LP_{01} mode, has a fundamental role in the detection of exoplanets. Indeed, one major limitation of a telescope is its capability to recolt enough photons of faint objects in comparison to the noises. Then, in order to maximize the signal to noise ratio SNR, the maximum of planet's light needs to be transmitted to the detector.

The coupling efficiency characterize this loss and can be defined as the ratio of the energy between output and input of the single mode fiber. An equivalent definition in function of the electric fields is used here. The definition states that the coupling efficiency ρ is the overlap integral between the electric field at the entrance of the fiber and the mode LP_{01} of the SMF.

$$\rho = \frac{|\int\int_S E_B^*(x,y)F_B(x,y)ds|^2}{\int\int_S |E_B(x,y)|^2 ds \int\int_S |F_B(x,y)|^2 ds} \tag{2.19}$$

with E_B the electric field of the incoming light in the focal plane on the fiber core, E_B^* the complex conjugate of E_B and F_B the electric field of the mode LP_{01} [31].

In fact, it has been demonstrated that the coupling efficiency is limited to 78% for a plane wave focusing on the fiber core [45]. This value results from the fact that the shape of the electric profile at the focus of a telescope, when looking at celestial body, is a Bessel function. The mismatch with the Gaussian shape of the fundamental mode of the fiber thus results in a loss of 22%. This value of the coupling efficiency is achievable when the fiber and the telescope are properly designed. Indeed, the value of the coupling efficiency depends on multiple parameters defining the single mode fiber and the telescope. Therefore, the study of the coupling efficiency in function of design parameters, that need to be defined, is of utmost importance in order to optimize the performance of the injection.

2.7 Deformable mirror for space application

It was shown that the use of single mode fibers is very useful to relax the requirements on the wavefront quality. A maximum standard deviation across the pupil of 0.11 radian was needed to achieve a null ratio of 10^{-5}. However such a quality is still

challenging since it is close to the diffraction limited case. Indeed, according to the Marechal approximation, the Strehl ratio is

$$S = \exp\left(-\sigma^2\right) = 0.99 \tag{2.20}$$

Therefore, in space environement, where sources of aberrations are multiple, the use of an adaptive system to correct the wavefront is mandatory.

2.7.1 Principles of adaptive/active optic

An adaptive or active optic system consists of three main components, a deformable mirror to correct the optical disturbances by phase conjugation, a wavefront sensor to detect these disturbances, and a control system to give the desirable shape of the DM by interpreting the wavefront sensor informations [48]. In Figure 2.13 a schematic view of a conventional adaptive system is represented.

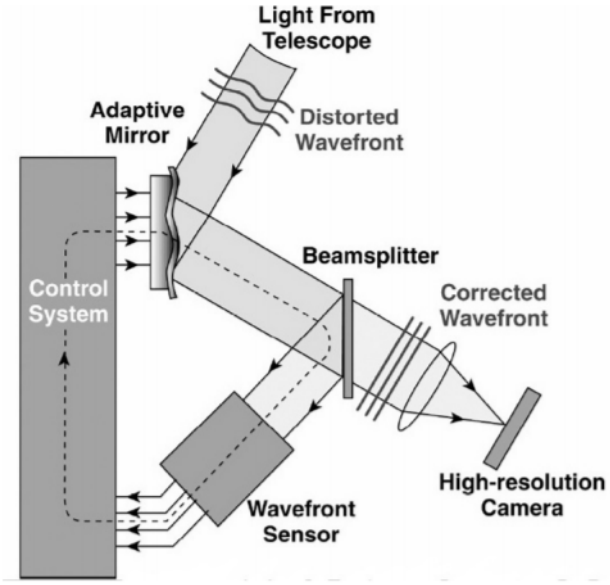

Figure 2.13: Representation of an adaptive system. The light from the telescope reachs a deformable mirror. Then, a part of the light is sent to the wavefront sensor thanks to a beamsplitter. The wavefront sensor measures the aberration of the wavefront and the control system deforms the mirror to compensate the aberration.

2.7.2 MEMS DMs

Deformable mirrors (DM) have already been proved useful for ground based operations. Frequently used DM are piezoelectric and lead-magnesium-niobate (PMN) stacked array mirrors. It consists of stacks of individual plates made of PZT or PMN that deform longitudinally, when a voltage is applied between the electrodes of the actuator, and pushs the DM [27]. VLT and Gemini are two examples of ground based telescope equipped with such a DM.

However, another class of DM seems to be more suitable for space applications: Microelectromechanical systems (MEMS) deformable mirrors. Indeed, MEMS mirrors offer many advantages. They are cheaper and more compact allowing the reduction of the size and the mass of the payload. Also, their low actuator mass makes them resilient to launch-induced vibrations [21]. MEMS concepts relies on a reflecting surface which is deformed by an electrostatic or a magnetic field. In Figure 2.16 one example of the MEMS DM concept is represented.

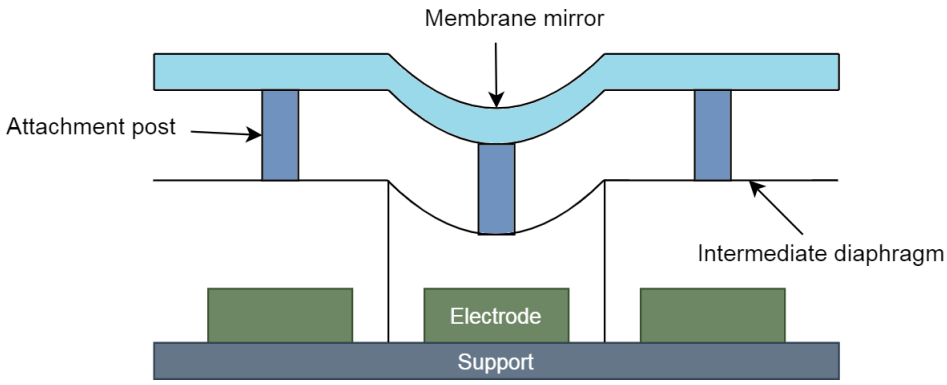

Figure 2.14: MEMS DM concept. The intermediate diaphragm is locally deformed by the action of the electric force generated by the electrode. Then the deformation is transmitted to the membrane mirror by the attachment post [24].

At the current time, MEMS DM have flown in space. One example is the Planet Imaging Concept Testbed Using a Rocket Experiment (PICTURE) mission. It is a sounding rocket for high-contrast imaging with a visible nulling coronagraph from Nasa. Its mission is to observe the warm dust disk inferred around Epsilon Eridani [25]. Besides a nulling interferometer, PICTURE carries an ultralightweight 0.5 m diameter primary mirror, a wavefront control system with a 32x32 element MEMS DM

manufactured by Boston Micromachines Corporation and a milliarcsecond pointing control system. In Figure 2.15 the optical layout of PICTURE is represented.

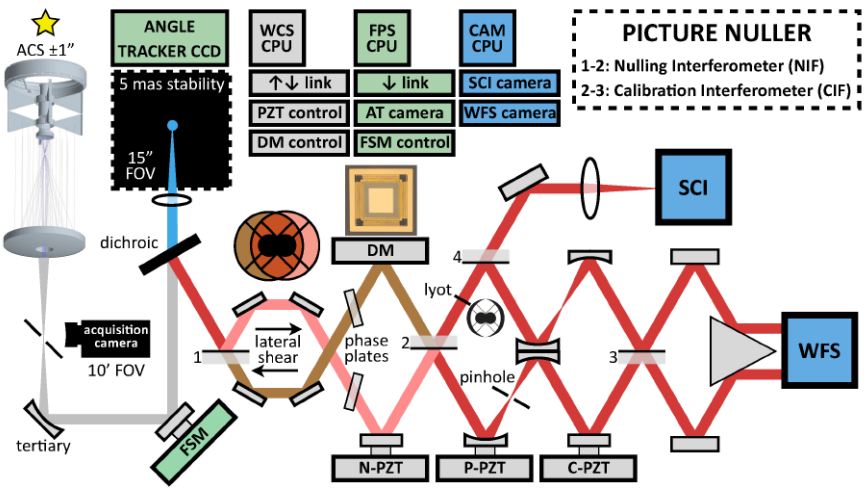

Figure 2.15: PICTURE optical layout [26].

A second example of MEMS DM in space is the satellite DeMi [21]. Deformable Mirror Demonstration Mission (DeMi) is a 6U (30 cm x 20 cm x 10 cm) CubeSat that was launched the 15 February 2020. It is a nanosatellite that will serve as an on-orbit testbed for the MEMS deformable mirror technology. The DeMi is based on the Blue Canyon Technologies XB6 platform. The bus includes the XACT ADCS (Attitude Determination and Control System) which allows a pointing accuracy of 10 arcseconds in all directions. The DM on board is the Boston Micromachines Mini DM with 140 actuators and 5 mm aperture. In Figure 2.16 a picture of this DM. In Figure 2.19 the CubeSat seen from the International Space Station (ISS).

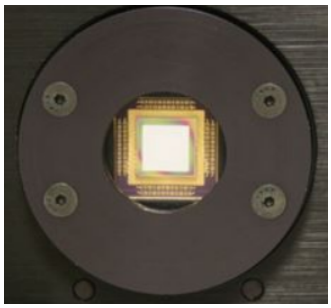

Figure 2.16: Boston Micromachines Mini DM with 140 actuators [24].

The mission should raise the technology readiness level (TRL) of MEMS DMs

from 6 (qualification in a relevant environement) to at least 7 (qualification in a operational environement).

Figure 2.17: DeMi CubeSat deployed from the International Space Station on 13 July 2020 (image credit: NASA)

2.7.3 Monomorphe deformable mirrors

Another type of deformable mirror that is promising for space applications is the monomorphe DM. The mirror consists of a layer of one piezoelectric disk that can deform thanks to the piezoelectric effect when the electrodes are activated. Then, the optical plate is deformed thanks to the transverse deformation in the piezoelectric disk.

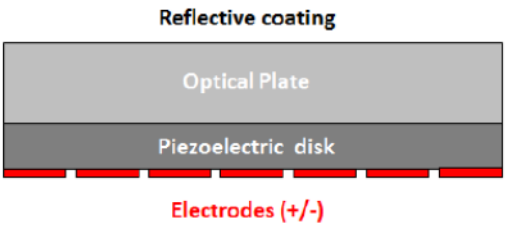

Figure 2.18: Unimorph mirror concept. The disk of piezoelectric ceramics is deformed when a voltage is applied to the electrodes. The optical plane is deformed due to transverse piezoelectric effect of the piezoelectric disk [28].

The french company CILAS (Compagnie Industrielle des Lasers) is the pioneer for this technology. They obtained a TRL 6 in 2017. Their mirror offers wavefront

error $\sim 10\ nm$ RMS after correction with a high efficiency (90% up to 7th order).

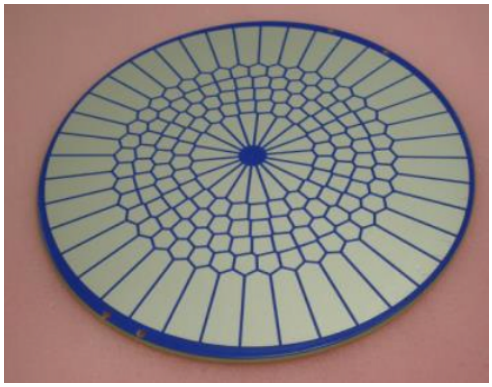

Figure 2.19: The CILAS 188 actuators bimorph mirror installed in the 8.2 m Subaru telescope [28].

2.8 Thesis objectives

Since 2005 several space-based interferometry missions have been considered. However they were all canceled. Figure 2.20 presents the five main space interferometry projects and their date of cancellation.

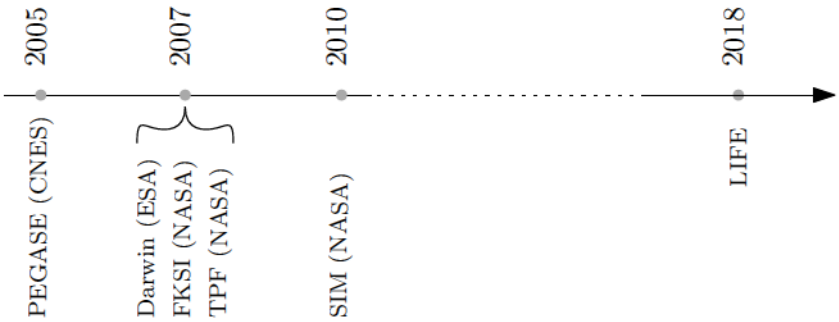

Figure 2.20: Timeline of the development of space-based interferometry missions [32].

Nevertheless, in 2018 a new project is considered: LIFE (Large Interferometer For Exoplanets). The goal of this project is to launch a large space-based MIR nulling interferometer in order to detect and characterize exoplanets.

In this context the University of Liège and the Centre Spatial de Liège (CSL) are developing a space-based nulling interferometer on a CubeSat platform in order to

demonstrate the feasibility of the LIFE project [60].

This master thesis is a contribution to this small satellite project. Its purpose is to analyse the coupling efficiency of a single mode fiber placed at the focus of one of the two telescopes of a nulling interferometer. The coupling efficiency is analysed in function of design parameters like the f-number (ratio of the focal length over the pupil diameter), the central obstruction (if the telescope is Cassegrain, the secondary mirror obstructs the primary mirror and the central obstruction is defined as the ratio of the secondary mirror diameter over the primary mirror diameter). The fiber will be optimized in order to maximize the coupling efficiency. A schematic view of the system that will be analysed is presented in Figure 2.21.

The second purpose of the thesis is to study the coupling efficiency when static aberrations degrade the system. It will allow us to determine which aberrations have to most impact on the performance of the system. The coupling efficiency is analysed when the system has aberrations typically encountered in space. They represent slowly varying aberrations like misalignment of the optics, pointing and polishing errors. They are defined as non-common path aberrations (NCPA) and can be considered as static aberrations [52], [23]. The effect of the correction by a deformable mirror is also analysed. The goal is to achieve RMS wavefront error below ~ 0.1 rad since it is the requirement to get a null ratio of 10^{-5}.

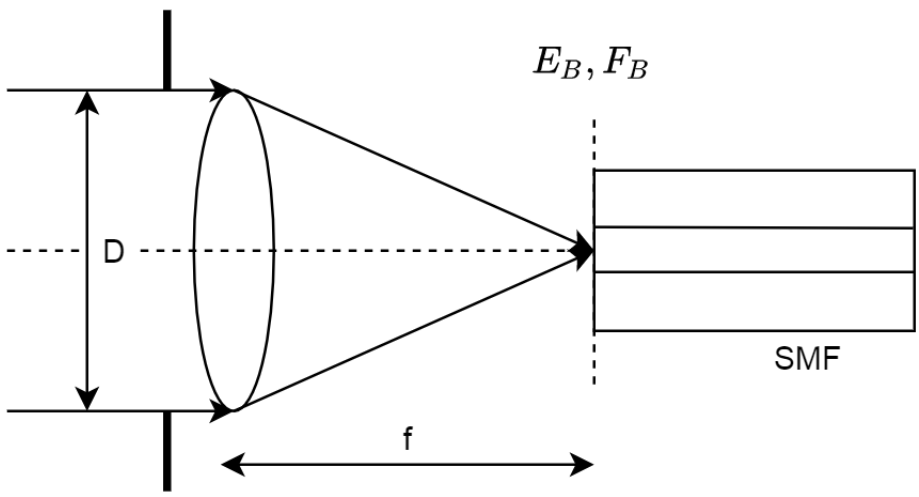

Figure 2.21: Representation of the single mode fiber at the focus of a telescope. D is the aperture of the telescope. f the focal length. E_B the electric field of the incoming light and F_B the electric field of the fundamental mode of the SMF.

Chapter 3

Fundamental concepts about imaging optics

As stated in the first chapter, the objective of this thesis is to study the coupling efficiency of a single mode fiber placed at the focus of a telescope. Since the coupling efficiency is defined as the overlap integral between the electric field at the input of the fiber and the fundamental mode of the fiber, it is mandatory to know exactly the electric field profile of the light injected. Therefore, this chapter aims to remind the fundamental principles of optics needed to understand how to compute the electric field. It is based on the Fourier optics theory developed by Goodman in his book Introduction to Fourier Optics [50].

The discussion starts with a brief description of the Rayleigh-Sommerfeld scalar diffraction theory. Then the definition of a diffraction limited system is presented with an emphasis on the definition of the point spread function. Afterwards the Rayleigh resolution criterion is presented. The third section aims to present the aberration theory of light. This section will be useful later to estimate the loss of coupling efficiency when the light is aberrated. It starts by defining the wavefront aberration function thanks to the spherical reference surface. Follows the definition of the generalized pupil function. Then the Strehl ratio is defined. Finally Zernike circle polynomials are presented.

3.1 Propagation of light

Since the work of Maxwell in 1860, it is accepted that light is an electromagnetic wave which propagates according to four equations, called Maxwell's equations. This wave behaviour results in the diffraction phenomenon defined by Sommerfeld as "any deviation of light rays from rectilinear paths which cannot be interpreted as reflection or refraction."[20] Such effect can be observed when a wave interacts with an obstacle that restrains its spatial extent, like for example an aperture. Diffraction phenomena are more important when the obstacle is in the order of the wavelength of the light.

3.1.1 Scalar diffraction theory

Under some hypotheses the propagation of light can be described by the scalar diffraction theory of Sommerfeld. These hypotheses state that the light is propagating in a dielectric medium which is linear, homogeneous, isotropic, nondispersive and nonmagnetic. According to these assumptions, the electric field (E_x, E_y, E_z) and magnetic field (H_x, H_y, H_z) components are no longer coupled. Therefore each component of the electric or magnetic fields can be expressed independently from the other components. Each component is then solution of the scalar wave equation

$$\nabla^2 u(P,t) = \frac{n^2}{c^2}\frac{\partial^2 u(P,t)}{\partial t^2} \tag{3.1}$$

where $u(P,t)$ represents any of electric and magnetic field components at the position P, c the speed of light in the vacuum and n the refractive index of the medium.

Scalar diffraction theory is well suited for describing transmission of light through space or the atmosphere. It finds thus lot of applications in remote sensing or astronomical observations.

3.1.2 Helmholtz equation

A monochromatic light propagating in an isotropic medium can be expressed by

$$u(P,t) = A(P)\cos(2\pi\nu t - \Phi(P)) \tag{3.2}$$

where $A(P)$ is the complex amplitude, $\Phi(P)$ is the phase of the wave and ν is the temporal frequency.

An equivalent formulation is

$$u(P,t) = \Re\{A(P)\exp\left[j\Phi(P)\right]\exp(-j2\pi\nu t)\} \tag{3.3}$$

where $\Re\{\}$ represents the real part of the complex function.

In a linear medium the temporal frequency stay constant and it is thus convenient to study only the spatial contribution of the field, often called the phasor,

$$U(P) = A(P)\exp[j\Phi(P)] \tag{3.4}$$

Putting Eq.3.4 in Eq.3.1 it follows that U must satisfy the Helmholtz equation

$$(\nabla^2 + k^2)U = 0 \tag{3.5}$$

with $k = \frac{2\pi}{\lambda}$ the wave number.

3.1.3 Rayleigh-Sommerfeld solution

For the case of monochromatic wave coming from a 2D plane source to the 2D observation plane, a solution to the Helmholtz equation is given by the first Rayleigh-Sommerfeld diffraction solution

$$U_2(x,y) = \frac{A}{j\lambda}\int\int_{\sum}\frac{\exp(jkr_{12})}{r_{12}}\cos(\mathbf{n},\mathbf{r}_{12})d\xi d\eta \tag{3.6}$$

with (ξ,η) the coordinates in the source plane, (x,y) the coordinates in the observation plane, $\sum$ the illuminated aperture, $\mathbf{n}$ the normal vector of the source plane at (ξ,η), $r_{12} = \sqrt{z^2 + (x-\xi)^2 + (y-\eta)^2}$ the distance between the point (x,y) and the point (ξ,η), A the amplitude of the homogeneous electric field of the source plane.

This solution expresses the Huygens-Fresnel principle which stipulates that each point of the aperture act like a a spherical wave source. Indeed the integral represents the observed field $U_2(x,y)$ as a superposition of diverging spherical waves $A\exp(jkr_{12})/r$ originating from secondary sources located on each point within the aperture.

For an arbitrary amplitude $U_1(\xi,\eta)$ and after developing the cosine function, the Rayleigh-Sommerfeld solution can be expressed by

$$U_2(x,y) = \frac{z}{j\lambda}\int\int_{\sum}U_1(\xi,\eta)\frac{\exp(jkr_{12})}{r_{12}^2}d\xi d\eta \tag{3.7}$$

where z is the distance between the centers of the source and observation coordinate systems.

In Figure 3.1 the propagation of the light coming from the source plane to the observation plane is represented.

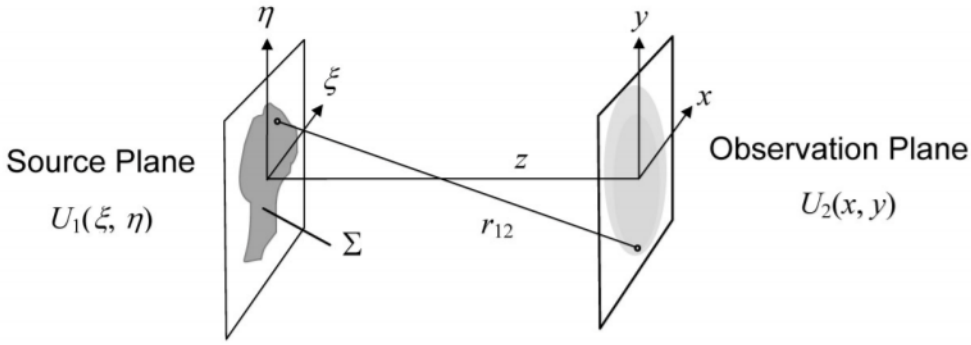

Figure 3.1: Propagation geometry [49].

In the definition of r_{12} the square root makes the computation of the Rayleigh-Sommerfeld solution difficult to obtain. In order to simplify the problem two different approximations on can be made.

3.1.4 Fresnel approximation

The Fresnel approximation (or near field) is based on the Taylor series expansion of $r_{12} = \sqrt{z^2 + (x-\xi)^2 + (y-\eta)^2}$:

$$r_{12} \approx z\Big[1 + \frac{1}{2}(\frac{x-\xi}{z})^2 + \frac{1}{2}(\frac{y-\eta}{z})^2\Big] \tag{3.8}$$

This approximation is used in the argument of the exponential and describes the point sources as parabolic radiation wave emitters. Moreover with the approximation $r_{12} = z$ in the denominator of Eq.3.7 the Fresnel diffraction expression is given after factorization by

$$U_2(x,y) = \frac{\exp(jkz)}{j\lambda z} \exp\Big[j\frac{k}{2z}(x^2+y^2)\Big] \times \int\int U_1(\xi,\eta) \exp\Big[j\frac{k}{2z}(\xi^2+\eta^2)\Big] \exp\Big[-j\frac{2\pi}{\lambda z}(x\xi + y\eta)\Big] \tag{3.9}$$

Then, aside from a multiplicative factor, the electric field at the observation plane is the Fourier transform of the product of the field $U_1(\xi,\eta)$ by a quadratic phase

exponential.

3.1.5 Fraunhofer diffraction

In addition to Fresnel approximation, the Fraunhofer approximation is

$$z \gg \left(\frac{k(\xi^2+\eta^2)}{2}\right)_{max} \tag{3.10}$$

which leads to Fraunhofer diffraction expression:

$$U_2(x,y) = \frac{\exp(jkz)}{j\lambda z}\exp\left[j\frac{k}{2z}(x^2+y^2)\right] \times \int\int U_1(\xi,\eta)\exp\left[-j\frac{2\pi}{\lambda z}(x\xi+y\eta)\right] \tag{3.11}$$

The approximation is known as the far field approximation since the condition on z requires very long propagation distances. However Fraunhofer diffraction expression can be used for much smaller distance.

A very important result is that at the focus of a telescope the diffraction pattern is the Fraunhofer diffraction pattern of the pupil function [30].
This result will be used in the following work to describe the electric field at the focus of a telescope. It will makes possible the numerical computation of the coupling efficiency of a single mode fiber situated at the focus of the telescope.

3.2 Diffraction-limited optics

A fundamental concept in optic is the notion of diffraction-limited. By definition an imaging system is said to be diffraction-limited if a diverging spherical wave, emanating from a point-source object, is converted by the system into a new wave, again perfectly spherical, that converges towards an ideal point in the image plane given by geometrical optics [50]. A system respecting this condition is said to be diffraction limited.
To understand the meaning of the term "limited " in this definition it is important to introduce the relation between the object and its image in a imaging system.

3.2.1 Imaging system

Since the work of Ernst Abbe in 1873 it is known that the diffraction effect of an imaging system can be viewed as the result of the spatial limitation of the wavefront at the entrance pupil. On the other side Lord Rayleigh in 1896 presented the equivalent result that the diffraction effects is induced by the spatial limitation of the wavefront at the exit pupil. These results are equivalent due to the fact that the entrance and exit pupil are images of each other.

A consequence of this is that the propagation of light between the two planes can be described by geometrical optics. Therefore an imaging system can be viewed as a black box such that the significant properties of the system can be completely described by specifying only the proprieties at the pupil planes. Figure 3.2 represents the concept of the black box.

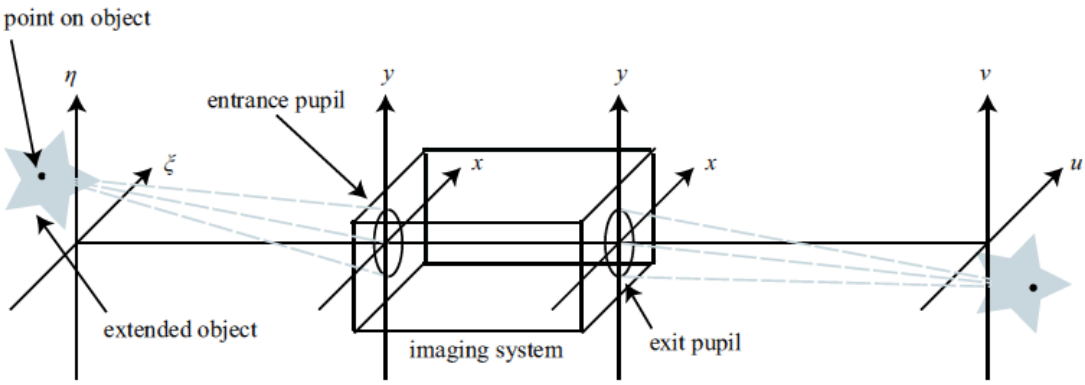

Figure 3.2: Basic model of an imaging system [51].

Two cases of illumination need to be discussed in order to define the fundamental concept of the point spread function: coherent and incoherent illumination.

3.2.2 Concept of coherence and application in stellar interferometry

An illumination is said to be coherent if it exists a constant relative phase between the wave trains emitted by the source. Coherent illumination is therefore obtained whenever light appears to originate from a single point. Indeed, for the case of an extended source, the different points on its surface randomly emit wave trains which create uncorrelated phases between the trains. As a consequence, monochromatic

light source are always coherent. However such a source does not exist. Even laser emitting at a single wavelength possesses a bandwidth which creates incoherence. Nevertheless, coherent illumination represents an interesting approximation that need to be discussed.

In interferometry the concept of coherence is fundamental. It can be used for the determination of the angular separation between two celestial bodies, the angular diameter of the source or the nature of the source.

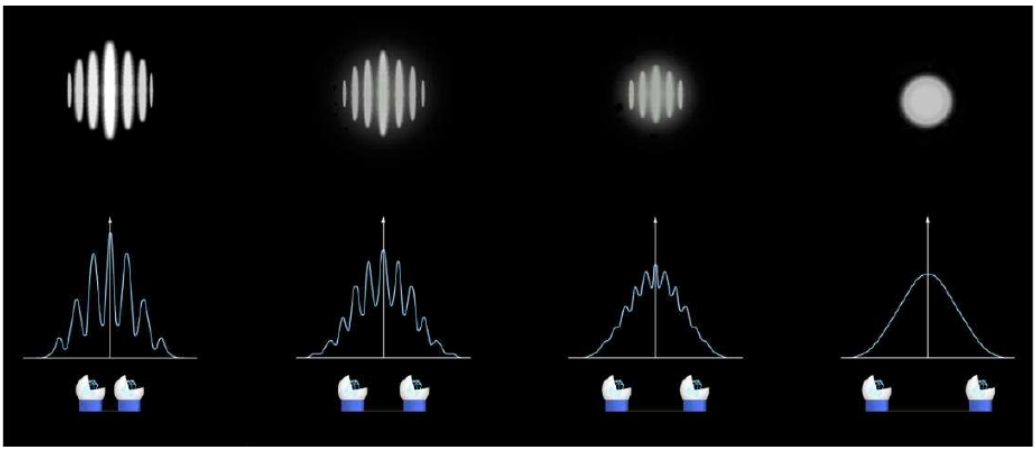

Figure 3.3: Principle of visibility. (defrere lecture)

Since interferences occur when the sources are coherent, two points are resolved when the fringes of interference completely disappear. Moreover, it is proved that it is the case when

$$\alpha = \frac{\lambda}{2B} \tag{3.12}$$

with B the length of the baseline. Then, to determine the angular separation, for example between a star and a exoplanet, the length of the baseline is adjusted until the fringes disappear. Putting this value of B in Equation 3.12 gives the angular separation.

The information of the intensity of the fringes is given by the visibility (or contrast)

$$V = \frac{I_{max} - I_{min}}{I_{max} + I_{min}} \tag{3.13}$$

A contrast of 1 occurs when $I_{max} = 1$ and $I_{min} = 0$ which is the case when the light interfer perfectly destructively and and constructively. This is only the case for

perfect coherent sources. In Figure 3.3 the visibility in function of the baseline length is represented.

3.2.3 Coherent illumination

It can be shown that coherent light induces an imaging system to be linear in amplitude.

By defining the reduced coordinates $(\overline{\xi}, \overline{\eta})$ in the object space

$$\overline{\xi} = M\xi \tag{3.14}$$

$$\overline{\eta} = M\eta \tag{3.15}$$

with M the magnification, the image amplitude is given by the convolution product

$$U_i(u,v) = \int\int h(u-\overline{\xi}, v-\overline{\eta}) U_g(\overline{\xi}, \overline{\eta}) d\overline{\xi} d\overline{\eta} \tag{3.16}$$

where

$$U_g(\overline{\xi}, \overline{\eta}) = \frac{1}{|M|} U_0\Big(\frac{\overline{\xi}}{M}, \frac{\overline{\eta}}{M}\Big) \tag{3.17}$$

represents the ideal image predicted by the geometrical optic and h is the impulse response (or amplitude spread function) defined by

$$h(u,v) = \frac{A}{j\lambda z_i} \int\int P(x,y) \exp\Big[-j\frac{2\pi}{\lambda z_i}(ux+vy)\Big] dxdy \tag{3.18}$$

where P is the pupil function equals to one inside the aperture and zero outside. The impulse response is the response of the system to a point source. In astronomical observation a star is viewed as the point object.

Thus the image can be evaluated by the convolution product of the impulse response, which is given by the Fraunhofer diffraction pattern of the exit pupil, with the image predicted by geometrical optics.

Therefore the role of the impulse response in Eq.3.16 is to spread U_g on the image plane. This effect has the consequence to limit the resolution of the imaging system since the image of a point source will not be a point image but a diffraction pattern depending on the shape of the aperture. In other words diffraction impose a physical limit for the resolution of an optical system.

This limit is more detailed in the next section with the introduction of the point spread function.

3.2.4 Incoherent illumination

For incoherent illumination no linear relation exists between the image amplitude and the object amplitude. In fact an incoherent imaging system is linear in intensity such that

$$I_i(u,v) = \kappa \int\int_{-\infty}^{+\infty} |h(u-\overline{\xi}, v-\overline{\eta})|^2 I_g(\overline{\xi},\overline{\eta}) d\overline{\xi} d\overline{\eta} \tag{3.19}$$

with κ a real constant, I_g the ideal image intensity and $|h|^2$ the point spread function (PSF).

For a circular aperture of radius R, i.e $P(x,y) = 1$ for $\sqrt{x^2+y^2} = r \leq R$,

$$PSF = \left(\frac{R^2}{\lambda z}\right)^2 \left[\frac{J_1(2\pi\xi)}{\xi}\right]^2 \tag{3.20}$$

with $\xi = \frac{rR}{\lambda z}$ and r the radial distance from the center in the observation plane.

This PSF is referring as the Airy pattern. It corresponds to a central bright spot of radius $1.22\lambda/D$, called the Airy disc. Within this disk 83.8% of the total power is present while the remaining energy is spread into the diffraction rings [47].

3.2.5 Resolution criterion

Based on the Airy pattern of a circular aperture, a common way to describe the resolution of an optical system is the Rayleigh criterion.

This criterion stipulates that two point sources can be resolved if the distance between them is larger than the distance between the pick intensity of one and the first minimum of the second. Therefore two points are resolved when their angular separation $\Delta\theta$ follows

$$\Delta\theta \geq 1.22\lambda/D \tag{3.21}$$

The Rayleigh criterion is represented in Figure 3.5.

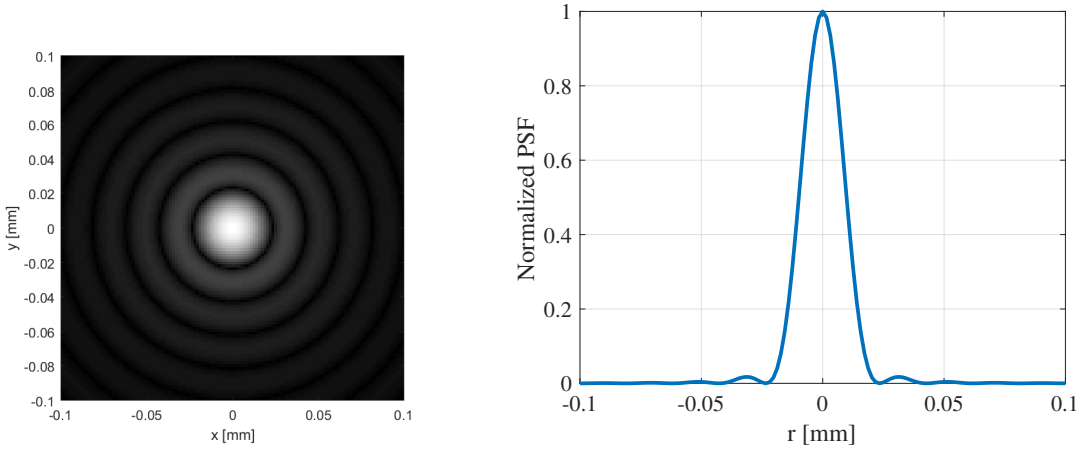

Figure 3.4: Point spread function of a circular aperture. The figure is known as Airy pattern.

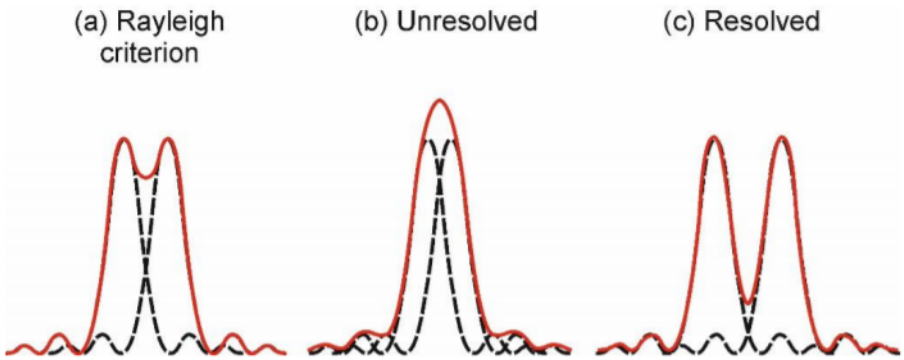

Figure 3.5: Rayleigh criterion [55].

3.3 Aberration theory

If in the presence of a point-source object, like a star, the wavefront leaving the exit pupil departs significantly from ideal spherical shape, then the imaging system is said to have aberrations.

3.3.1 Sources of aberrations in space

Aberrations can occur for many reasons. It can be caused by defect in the optics like irregularities created during the polishing. Also, aberrations can be inherent to the shape of the optics. Spherical aberration is a good example since it is present in common mirrors and lenses with spherical curvatures.
Aberrations can also appear because of external loads like heat.

Indeed, a satellite experiences many heat loads during its journey. For a spacecraft orbiting the Earth, the major contribution is the direct solar flux. For a plane facing the sun at 1 UA, the solar flux is approximately 1367 W/m^2 over a year. The second heat source is the albedo flux. It is due to the reflection of the sunlight by the Earth. The third environmental source is the Earth infrared radiation. This radiation comes from the fact that the Earth can be approximated by a blackbody at 255 K. Also, electronic components can generate heat by Joule effect. The main heat fluxes are represented in Figure 3.6. These loads can have a tremendous impact on the optical performance since heat could deform optical components. Therefore, the thermal study of the spacecraft needs to be performed in order to make sure that the telescope works as intended. A study of this nature is currently performed by Arthur Scheffer [59].

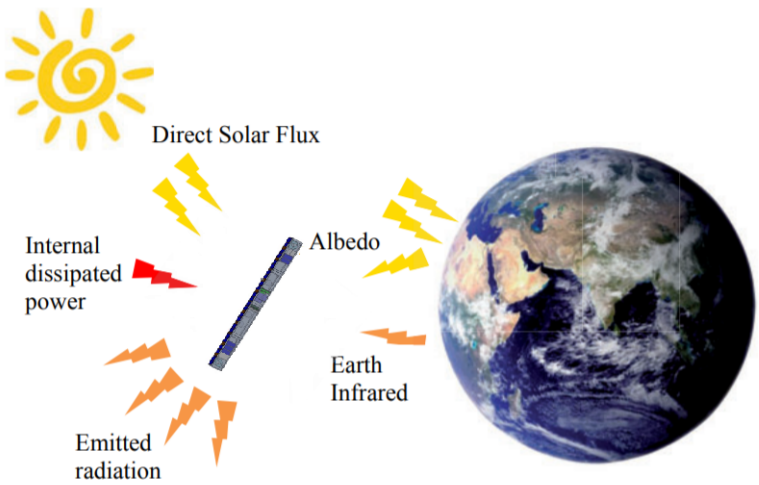

Figure 3.6: Thermal loads on a spacecraft orbiting around the Earth.

Another concern about the detection of exoplanets is the pointing accuracy of the spacecraft. Indeed, error in the pointing will result in a shift of the focal plane resulting in a diminution of the coupling efficiency.

Unfortunately pointing accuracy of spacecraft is limited. It is even more true for small spacecraft. In Figure 3.7 the state of the art of pointing accuracy is displayed. It shows that for cubesat platform, Blue Canyon Technologies provides the best pointing accuracy: 0.002°.

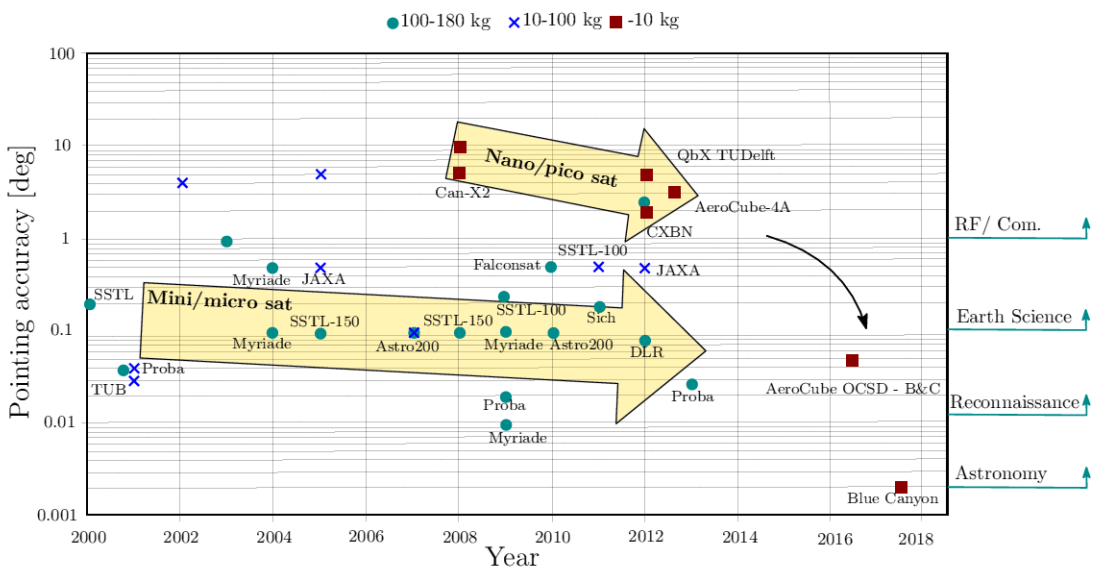

Figure 3.7: State of art of small pointing accuracy [32].

3.3.2 Generalized pupil function

When an imaging system is diffraction limited, the (amplitude) point-spread function has been seen to consist of the Fraunhofer diffraction pattern of the exit pupil, centered on the ideal image point. In the case of aberrations this result is still valid with the proper definition of the pupil function.

When an aberrated wavefront reaches the exit pupil the wavefront leaving the pupil can be regarded as a aberration-free wavefront which passed through a phase-shifting plate in the aperture.

If Φ represents the wavefront error as defined in Figure 3.8, the impulse response is expressed by

$$h(u,v) = \frac{A}{j\lambda z_i} \int\int \mathcal{P}(x,y) \exp\left[-j\frac{2\pi}{\lambda z_i}(ux+vy)\right] dxdy \tag{3.22}$$

with $\mathcal{P}$ the generalized pupil function:

$$\mathcal{P}(x,y) = P(x,y) \exp\left[j\Phi(x,y))\right] \tag{3.23}$$

where $P(x,y)$ is the pupil function defined previously.

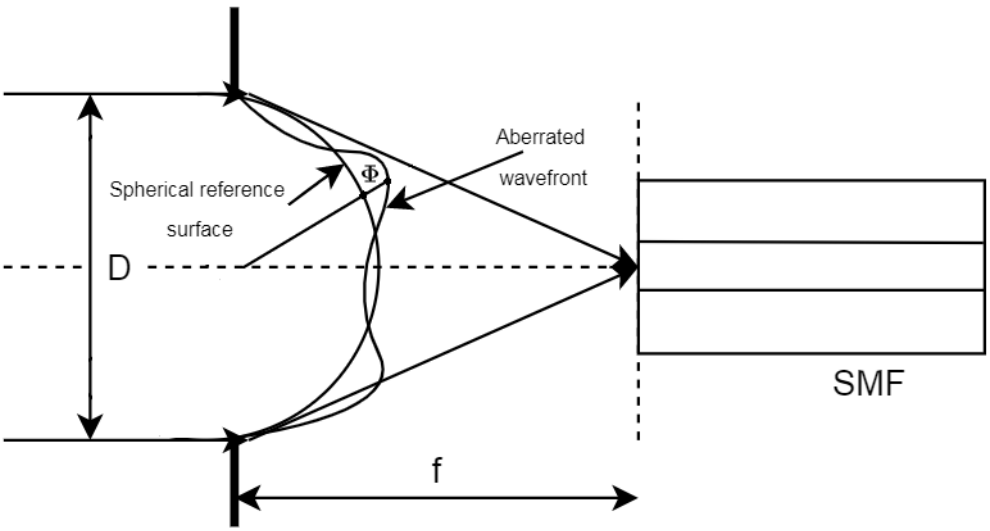

Figure 3.8: Wavefront aberration function. The ideal wavefront defining a diffraction limited system is the spherical reference surface. The wavefront aberration function Φ at point is the difference between the aberrated wavefront and the surface.

3.3.3 Strehl ratio

Another performance parameter that need to be considered is the Strehl ratio (S). It is defined as the ratio of central irradiance with and without aberration

$$S = \frac{I(0)_{\Phi}}{I(0)_{\Phi(0)}} = \left| \left\langle \exp[i(\Phi - \langle \Phi \rangle)] \right\rangle \right|^2 \tag{3.24}$$

For small aberration the Strehl ratio can be expressed in term of the variance σ_{Φ}^2 by the Marechal formula

$$S = (1 - \frac{1}{2}\sigma_{\Phi}^2)^2 \tag{3.25}$$

with $\sigma_{\Phi}^2 = \langle \Phi^2 \rangle - \langle \Phi \rangle^2$ and

$$\langle \Phi^n \rangle = \frac{1}{\pi} \int_0^1 \int_0^{2\pi} \Phi^n(r, \theta) r dr d\theta \tag{3.26}$$

Note that the root mean square $RMS = \sqrt{\langle \Phi^2 \rangle}$ equals the standard deviation σ_{Φ} if the mean aberration is zero.

3.3.4 Zernike circle polynomials

Usually the phase $\Phi(r,\theta)$ is decomposed in the based of the Zernike circular polynomials Z_i [11]:

$$\Phi(r,\theta) = \sum_{i=1}^{\infty} a_i Z_i(r,\theta) \tag{3.27}$$

where a_i are the Zernike expansion coefficients , representing the weight (or strength) of Z_i in the overall aberrated phase Φ.

These polynomials are defined on a unit circle and are well suited for the theory of aberration since the low order Zernike polynomials has the same shape that common aberrations.
It is convenient to use the polar coordinate to represent them since they can be decomposed in a product of a radial function with an angular function. A common way to order the polynomials is the Noll convention defined as follows [11]:

$$\begin{aligned} Z_i(r,\theta) &= \sqrt{n+1}R_0^n(r), && \text{if } m=0 \\ Z_i(r,\theta) &= \sqrt{n+1}R_n^m(r)\sqrt{2}\cos(m'\theta), && \text{if } m>0\text{, i even} \\ Z_i(r,\theta) &= \sqrt{n+1}R_n^m(r)\sqrt{2}\sin(m'\theta), && \text{if } m<0\text{, i odd} \end{aligned} \tag{3.28}$$

$$R_n^m(r) = \sum_{l=0}^{(n-m')/2} \frac{(-1)^l (n-l)!}{l!\Big[(n+m')/2-l\Big]!\Big[(n-m')/2-l\Big]!} r^{n-2l} \tag{3.29}$$

where r is the radial coordinate ranging from 0 to 1, θ the azimutal coordinate ranging from 0 to 2π, n is the radial order, m the azimutal order. The value of n, m are integer respecting $m \leq n$ and $n - m' =$ even with $m' = |m|$. Therefore only polynomials with particular combination of (n,m) exist and form the so called Zernike modes.
In Table.3.1 the first 21 polynomials are listed. In Figure 3.9 the Zernike polynomials from i=2 to i=15 are represented in 2D.

One characteristic of these polynomials are their orthogonality property over a circular pupil:

$$\int_0^{2\pi}\int_0^1 Z_i(r,\theta)Z_j(r,\theta) r dr d\theta = \pi\delta_{ij} \tag{3.30}$$

This property makes easy the computation of the RMS and phase variance. The determination of the wavefront RMS is made by simply summing the squares of the Zernike coefficients and taking the square root. Indeed the root mean square is

$$\begin{aligned} RMS \equiv \sqrt{\langle \Phi^2 \rangle} &= \sqrt{\frac{1}{\pi}\int_0^{2\pi}\int_0^1 \Phi^2(r,\theta) r dr d\theta} \\ &= \sqrt{\frac{1}{\pi}\sum_{i=1}^{\infty}\sum_{j=1}^{\infty}\int_0^{2\pi}\int_0^1 a_i Z_i(r,\theta) a_j Z_j(r,\theta) r dr d\theta} \\ &= \sqrt{\sum_{i=1}^{\infty} a_i^2} \end{aligned} \tag{3.31}$$

Also,

$$\langle \Phi \rangle = \frac{1}{\pi}\int_0^1\int_0^{2\pi} \Phi(r,\theta) dr d\theta = a_1 \tag{3.32}$$

It means that the mean value of the wavefront phase is the first coefficient of the Zernike expansion. This terms is known as piston.

Therefore the phase variance is given by:

$$\begin{aligned} \sigma^2 &= \langle (\Phi - \langle \Phi \rangle)^2 \rangle \\ &= \frac{1}{\pi}\int_0^{2\pi}\int_0^1 \Big[\Phi(r,\theta) - \langle \Phi(r,\theta) \rangle\Big]^2 r dr d\theta \\ &= \sum_{i=2}^{\infty} a_i \end{aligned} \tag{3.33}$$

i	n	m	$Z_i(r,\theta)$	Description
1	0	0	1	Piston
2	1	1	$r\cos\theta$	Horizontal tilt
3	1	-1	$r\sin\theta$	Vertical tilt
4	2	0	$2r^2-1$	Defocus
5	2	-2	$r^2\sin 2\theta$	Oblique astigmatism
6	2	2	$r^2\cos 2\theta$	Horizontal astigmatism
7	3	-1	$(3r^3-2r)\sin\theta$	Vertical coma
8	3	1	$(3r^3-2r)\cos\theta$	Horizontal coma
9	3	-3	$r^3\sin 3\theta$	Vertical trefoil
10	3	3	$r^3\cos 3\theta$	Oblique trefoil
11	4	0	$6r^4-6r^2+1$	Primary spherical
12	4	2	$(4r^4-3r^2)\cos 2\theta$	Vertical 2nd-order astigmatism
13	4	-2	$(4r^4-3r^2)\sin 2\theta$	Oblique 2nd-order astigmatism
14	4	4	$r^4\cos 4\theta$	Quadrafoil
15	4	-4	$r^4\sin 4\theta$	Quadrafoil
16	5	1	$(10r^5-12r^3+3r)\cos\theta$	2nd-order coma
17	5	-1	$(10r^5-12r^3+3r)\sin\theta$	2nd-order coma
18	5	3	$(5r^5-4r^3)\cos 3\theta$	
19	5	-3	$(5r^5-4r^3)\sin 3\theta$	
20	5	5	$r^5\cos 5\theta$	Pentafoil
21	5	-5	$r^5\sin 5\theta$	Pentafoil

Table 3.1: Zernike circle polynomials. Noll ordering from radial mode 1 to 5.

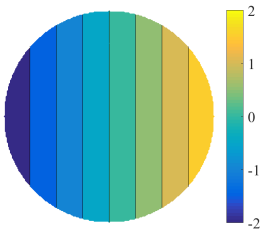

(a) Z_2, n=1, m=1

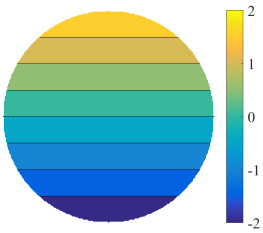

(b) Z_3, n=1, m=-1

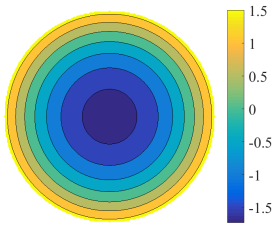

(c) Z_4, n=2, m=0

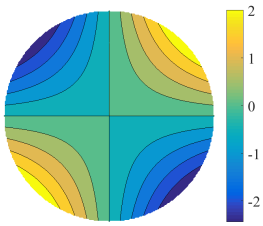

(d) Z_5, n=2, m=-2

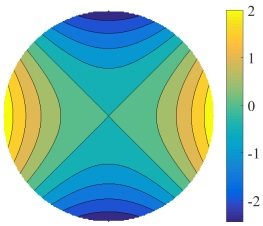

(e) Z_6, n=2, m=2

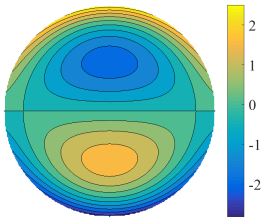

(f) Z_7, n=3, m=-1

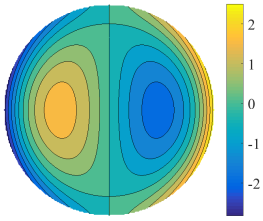

(g) Z_8, n=3, m=1

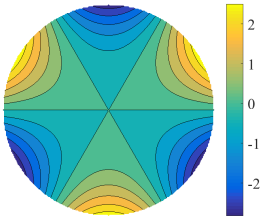

(h) Z_9, n=3, m=-3

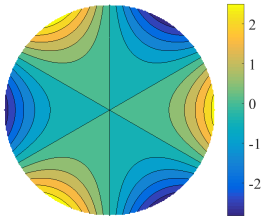

(i) Z_{10}, n=3, m=3

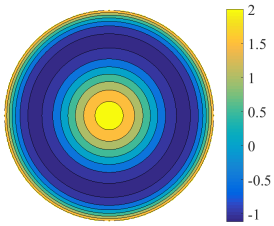

(j) Z_{11}, n=4, m=0

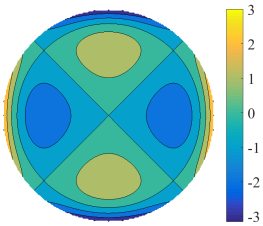

(k) Z_{12}, n=4, m=2

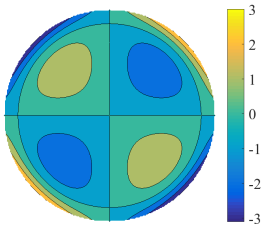

(l) Z_{13}, n=4, m=-2

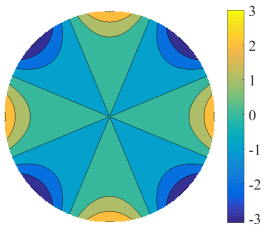

(m) Z_{14}, n=4, m=4

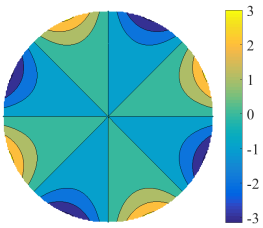

(n) Z_{15}, n=4, m=-4

Figure 3.9

Chapter 4

Single mode fiber

In the second chapter the theory needed to determine the electric field profile at the input of the fiber was presented. Therefore, to determine the coupling efficiency, the remaining electric profile to characterize is the one propagated in the SMF.
The goal of this chapter is to describe this profile. It will lead in the next chapter to the description of the methodology adopted to compute the overlap integral.

4.1 Guiding light principle

Optical fibers are circular dielectric materials that can transport energy and information by means of multiple internal reflections. They are constituted of two regions: a central core with a refractive index n_{core} surrounded by a concentric cladding made of a material with a smaller refractive index n_{clad} [35]. Fibers with a homogeneous cladding and core are called step-index and will be exclusively considered in this work. A schematic view of the fiber is represented in Figure 4.1.

Two common parameters defining the step-index profile in the fiber are the index difference Δn and the relative index difference Δ defined by

$$\Delta n = n_{core} - n_{clad} \tag{4.1}$$

and

$$\Delta = \frac{n_{core}^2 - n_{clad}^2}{2n_{core}^2} \tag{4.2}$$

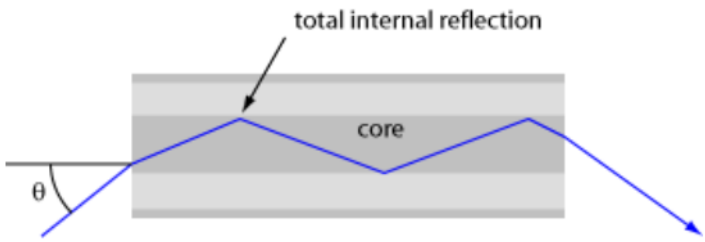

Figure 4.1: Incident light ray is first refracted in the core and then undergoes multiple total internal reflections at the core–cladding interface. This occurs for $\theta < \theta_{max}$ defining the acceptance cone [33]

.

Typical values of the relative index difference are $\Delta \approx 0.3 - 1\%$. Such small values can be explained by the fact that refractive index are obtained by doping the glass with oxide. This process limits the refractive index since the scattering losses increases with the doping level. The second reason is that the cone of acceptance of the fiber decreases when Δ increases. This has the consequence to increase the splice and connector (two methods for joining fibers) losses since it requires more precision to align fibers with smaller field diameter [31].

In Figure 4.2 a schematic view of the fiber cross section is represented with the refractive index profile.

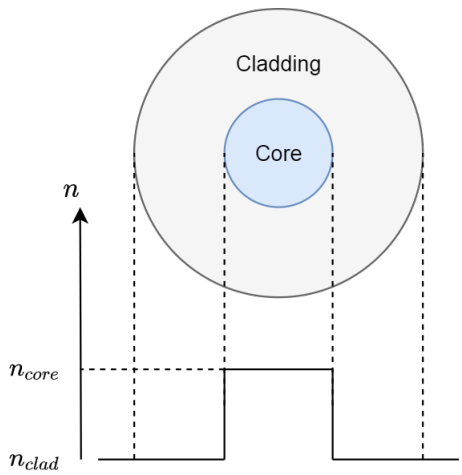

Figure 4.2: Schematic view of a step-index fiber.

4.2 Materials selection

The most used material for fibers optics is the silica (SiO_2) in different forms (e.g. germanosilicate or aluminosilicate glass). Theses glasses are widely used for their low propagation losses and their high mechanical strength (a polymer coating on thin silica enable bending without failure) [36]. Moreover other types of glasses like fluoride glasses (fluoroaluminate or fluorozirconate glasses) exist. This glasses are made of cation usually coming from heavy metals such as zirconium or lead, resulting in lower phonons energies. One consequence is that fluoride fibers are highly optically transparent at mid-infrared wavelengths compared to silica fibers which absorb light beyond $\approx 2\ \mu m$ [37]. This propriety makes the fluoride glass interesting for infrared observation.

Single-mode fibers based on fluoride glasses have already been qualified on stellar interferometers for wavelength up to 5 μm. For longer wavelengths, SMF based on chalcogenide based (up to 12 μm) or halogenide based (up to 20 μm or more) are considered [19], [3].

4.3 Applications

Optical fibers find an important numbers of applications. In optical fiber communications fluoride glasses are widely used. It allows the quick transport of data for long distance in a safe way (the signal guided is protected from its surroundings for a better electromagnetic compatibility).
Other examples among many are fiber lasers. Theses fibers find an interesting role in medical applications e.g. in ophthalmology and dentistry.

4.4 LP modes

A general concept that need to be understood for optical fibers design is the concept of modes. In the field of optical fibers, modes designate the transverse electric field distributions which remain constant during propagation in the fiber.

In a right-handed coordinates system attached to the fiber center, if it assumed that the electric field is polarized linearly in the x-direction and propagates in the z-direction, the phasor $E_x(r, \phi, z)$ of the x-component of the electric field of the LP_{lm} mode is given by

$$E_x(r, \phi, z) = E(r)\cos(l\phi)\exp(-j\beta z) \tag{4.3}$$

where $|E(r)\cos(l\phi)|$ represents the transverse amplitude distribution and $E(r)$ is solution of the scalar wave equation [38]

$$\frac{dE}{dr^2} + \frac{1}{r}\frac{dE}{dr} + \left(n^2(r)k^2 - \frac{l^2}{r^2} - \beta^2\right)E(r) = 0 \tag{4.4}$$

with $n(r)$ the refractive index profile, $k = 2\pi/\lambda$ the wave-number and β a phase constant depending on $n(r)$ and the operating wavelength λ [31].

l determines the number of full periods of the cosine function passed through when ϕ increases by 2π while m gives the number of intensity maxima in the core [31].

In Figure 4.3, electric field distribution for some modes at the exit of a step index fiber are displayed.

Guided modes are mainly located in the fiber core although some energy can propagate within the fiber cladding which is usually lost after some distance of propagation. [36] [34] For this reason cladding modes are also designate as radiation modes [35].

Optical fibers are generally classified in two categories, single-mode fibers (SMF) and multimode fibers (MMF), depending on whether the fiber carries one mode or more modes respectively.

On one hand single-mode fibers usually have a relatively small core ($\approx\mu m$) and can guide only the single spatial mode LP_{01} (one for each polarization direction) called the fundamental mode. The particularity of SMF, as mentionned in the first chapter, is that the electric field at the output of the fiber is independent on the electric profile at the input. Indeed, the electric profile is constant through its propagation in the fiber and the injection conditions only affects the power given to the guided mode (evaluated by the coupling efficiency).

On the other hand multimode fibers have a larger core ($\approx 50\mu m$) and/or a larger index difference between core and cladding. Contrary to SMF, the electric profile of light exiting the fiber core depends on the injection conditions. Depending on the shape of the incoming wavefront, some modes are exited and carry more or less energy [36].

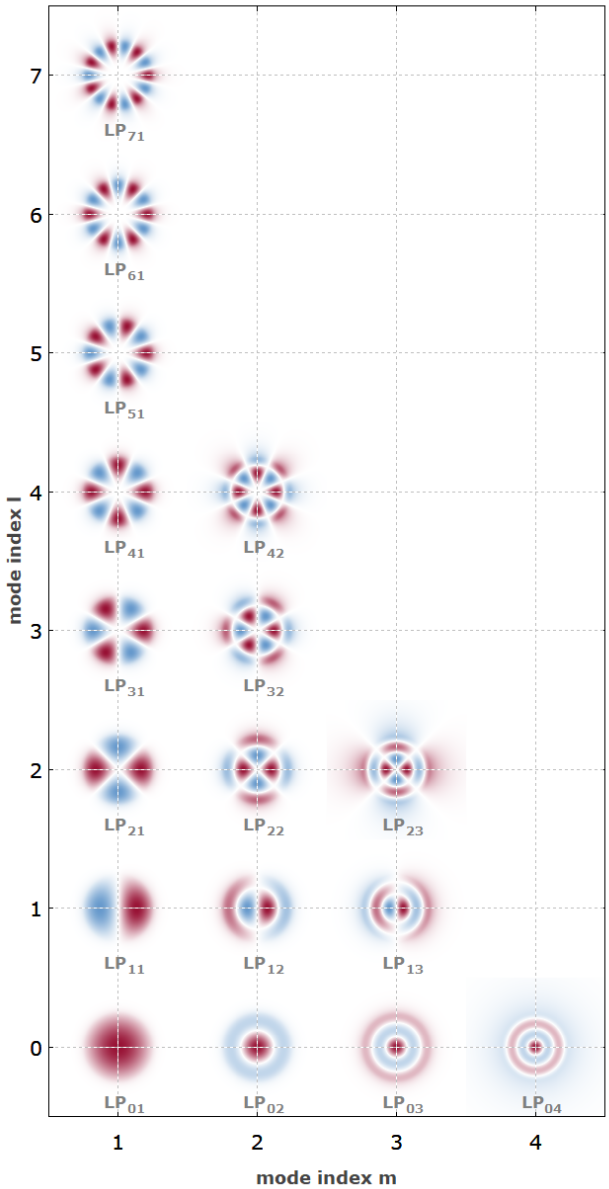

Figure 4.3: Electric field amplitude profiles for all the guided modes of a step-index fiber. The two colors indicate different signs of the electric field values [34].

4.5 Single mode fibers

Since the output of a single mode fiber is independent of the launching conditions, injecting an aberrated beam of light in a SMF would result theoretically in the correction of the light at the output of the fiber.

However this correction comes at the price of a reduction of the energy propagated

through the fiber. In fact, only a beam of light with the exact electric field distribution of the fundamental mode would result in a perfect transmission of the energy through the fiber.

This filtering process is used as an important application in astronomical interferometer. This is one of the main components in the recombination of light.
The feasibility of the SMF use for in recombination of ligth in stellar interferometry was demonstrated thanks to FLUOR (Fiber Linked Unit for Optical Recombination) in the near infrared [43].

4.5.1 Numerical aperture

As said previously, depending on some parameters, a fiber can be monomode or multimode. Therefore, some parameters need to be defined.

The numerical aperture NA is defined by

$$NA = \sqrt{n_{core}^2 - n_{clad}^2} \tag{4.5}$$

with n_{core} the index of refraction in the core and n_{clad} the index of refraction in the cladding region.

In the case of multimode fiber operation, the numerical aperture is linked to the maximum angle θ_{max} by which the light can be injected in the core of the fiber without light leakage in the cladding by the following formula:

$$\sin(\theta_{max}) = NA \tag{4.6}$$

Typical values of numerical aperture for multimode fibers ranges from 0.20 to 0.29 [41]. In the other side, SMF has typical NA between 0.12 and 0.14 [42].
Examples of single mode fibers are listed in Table 4.1.

Manufacturer	Fiber Type	NA	Wavelength
Fibercore	SM300	0.12 - 0.14	375 nm
Nufern	S630-HP	0.12	630 nm
Corning	SMF-28	0.14	1550 nm

Table 4.1: Typical values of numerical aperture of single mode fiber.

4.5.2 Normalized frequency

Another essentiel parameter to define the working condition of the SMF fiber is the normalized frequency V.
V is defined by

$$V = \frac{2\pi a NA}{\lambda} \tag{4.7}$$

with λ the wavelength of the injected light and a the fiber core radius.
The normalized frequency combines in a very useful manner the information about three important experimental design variables: the core radius, the numerical aperture, and the wavelength. It is called normalized frequency because it is inversely proportional to λ and because it is adimentional. This parameter defines completely the number of modes propagated by the fiber. If the fiber is used in condition such that $V \leq 2.405$, one mode is propagated, the fundamental one LP_{01} and the fiber is said single mode. If $V > 2.405$, higher order modes are propagated and the fiber is said multimode. The value of $V = 2.405$ is defined as the cutoff frequency V_c and correspond to the smallest frequency that supports LP_{11} mode.

4.6 LP_{01} profile

Since SMF are studied in this thesis, it is capital to study the fundamental mode LP_{01}.

The mode is obtained by solving Equation 4.4 when $l = 0$ and $m = 1$

$$\frac{dE}{dr^2} + \frac{1}{r}\frac{dE}{dr} + \left(n^2(r)k^2 - \beta^2\right)E(r) = 0 \tag{4.8}$$

This equation admits analytical solutions for special index profiles like the widely used step-index profile. For non conventional $n(r)$ direct numerical integration can be useful.

4.6.1 General expression

The profile of the LP_{01} of a SMF with a step index profile is a Bessel function in the core and a modifield Hankel function in the cladding [39],[40]:

$$E(r) = \begin{cases} J_0(\frac{Ur}{a}), & \text{if } r \leq a \\ \frac{J_0(U)}{K_0(W)} K_0(\frac{Wr}{a}), & \text{if } r > a \end{cases} \tag{4.9}$$

with U and W two parameters satisfying the conditions

$$U \frac{J_1(U)}{J_0(U)} = W \frac{K_1(W)}{K_0((W)} \tag{4.10}$$

$$U^2 + W^2 = V^2 \tag{4.11}$$

which describe the matching of the tangential components of the electric field and of the magnetic field at the core-cladding interface [31].

Note that the system of equations 4.10, 4.11 admits a unique solution only for V values smaller than 2.405. This value corresponds to the first zero of the Bessel function $J_0(x)$. This explains the condition for single mode operation stated earlier.

4.6.2 Gaussian approximation

When operating near cutoff frequency, the profile can be well approximated by a Gaussian with 1% error, [31],[29]

$$F_{01} \sim \exp[-\left(\frac{r}{\omega_0}\right)^2] \tag{4.12}$$

with the only parameter ω_0 which is the fundamental mode radius of the fiber well approximated by the following relation [43]

$$w_0 = a\left(0.65 + \frac{1.619}{V^{3/2}} + \frac{2.879}{V^6}\right) \tag{4.13}$$

This approximation has the advantage to use only one function to characterize the electric field in the fiber instead of two. Indeed the profile is the same in the cladding and the core with only one parameter to characterize it, the mode radius ω_0. Also this approximation is very useful since it allows an analytical expression for the coupling efficiency of non aberrated beam of light [43]. In Figure 4.4 the true electric field profile and the Gaussian approximation is displayed.

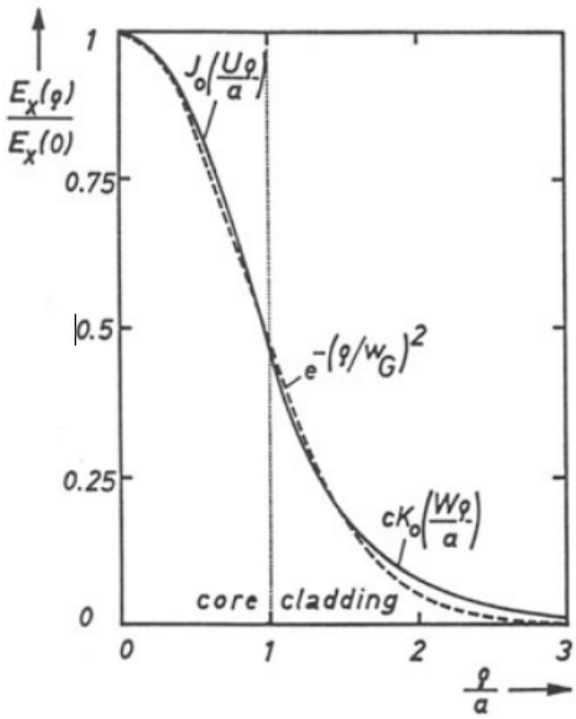

Figure 4.4: Normalized electric field distribution for a step index fiber at the normalized frequency V=2.2. The solid line is the exact electric field distribution. The dashed line represents the Gaussian approximation with $\omega_G/a = 1.162$. ω_G is the mode radius and q is the radial coordinate [31].

Chapter 5

Optical system

In this chapter the optical system considered is presented. It starts with the assumptions on the light and the choice of the waveband. Then a description of the telescope design. Next, the overlap integral is analysed and an equivalent formulation to the one presented in the first chapter is developed. This definition will be useful to decrease the cost of the simulations.

5.1 Waveband

In the following chapters, the light will be considered monochromatic while the medium linear, homogeneous, isotropic, nondispersive and nonmagnetic. According to these assumptions, the scalar diffraction theory of Sommerfeld can be applied and the results of chapter two will be used. Moreover since the goal is to study exoplanets in the infrared region, the waveband considered is $[3-7]\ \mu m$.

The choice of this waveband is an inspiration from the Fourier-Kelvin Stellar interferometer (FKSI) which was designed to study hot extrasolar giant planets at $[3-8]\ \mu m$ [53].

5.2 Telescope configuration

The study of the coupling efficiency is performed for one of the two telescopes present in the nulling interferometer. At this stage of the project the type of the telescope is not decided. It could be on-axis telescope like a Ritchey-Chretien (improved Cassegrain). It consists of two hyperboloid shaped mirrors. This configuration allows the elimination of the spherical aberration and the coma that are present with

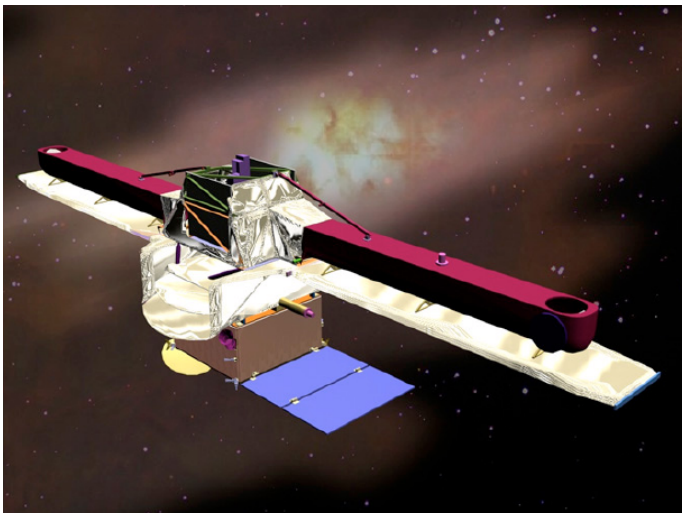

Figure 5.1: Representation of FKSI. Two telescopes of diameter 0.5 m separated by a distance of 12.5 m [53].

paraboiloid shaped mirrors. One example of this configuration is the Hubble Space Telescope (HST) represented in Figure 5.2

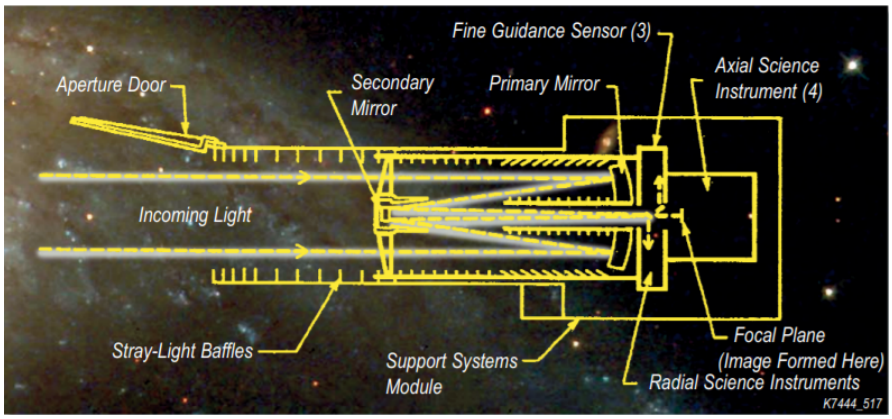

Figure 5.2: Hubble Space Telescope (HST) [57]

Another configuration could be an off-axis design. Such a configuration was used in the DeMi cubesat. It has the advantage to increase the throughput of the system since there is no obstruction blocking the photons entering the aperture. Also it avoids the diffraction effects produced by the interaction of the light with the back of the secondary mirror. The configuration of the DeMi satellite is represented in Figure 5.3.

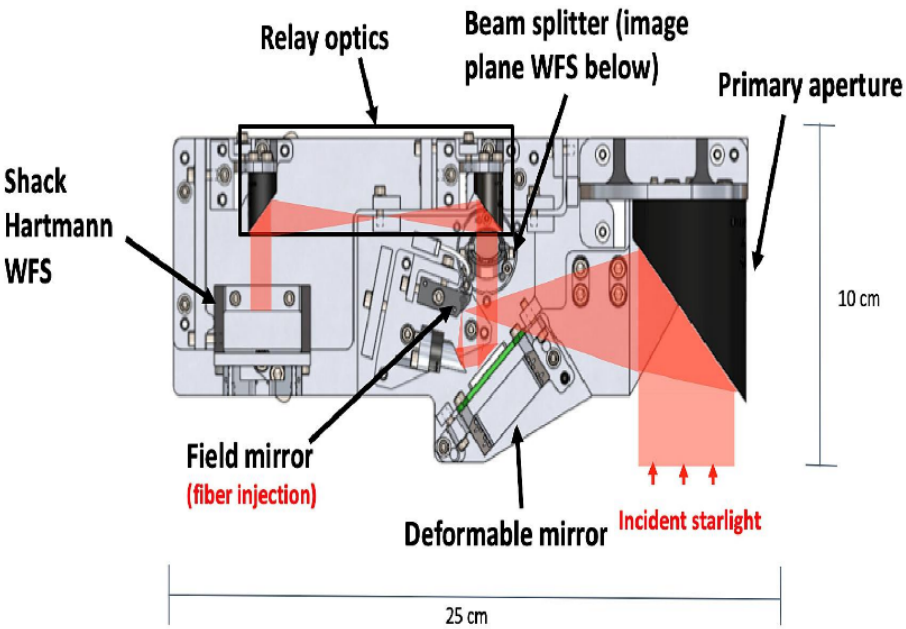

Figure 5.3: DeMi optical design with ray trace overlaid in red for the DeMi mission (image credit: DeMi Team).

Whatever the true configuration of the telescope is, the system can be schematized like a Cassegrain telescope. If the telescope is on-axis then the central obstruction equals the ratio between the secondary and primary mirrors diameter. If the telescope is off-axis then the obstruction equals zero.

5.3 Coupling efficiency

The coupling efficiency was defined in the first chapter as the overlap integral between the incoming electric field and the electric field in the single mode fiber. The coupling efficiency ρ is given by

$$\rho = \frac{|\int\int_S E_B^*(x,y)F_B(x,y)ds|^2}{\int\int_S |E_B(x,y)|^2 ds \int\int_S |F_B(x,y)|^2 ds} \tag{5.1}$$

with E_B the electric field of the incoming light in the focal plane on the fiber core, E_B^* the complex conjugate of E_B and F_B the electric field of the mode LP_{01} [31].

This definition is equivalent in the aperture plane. Indeed, in the chapter two, the electric field at the focus of a telescope was recognized as the Fourier transform of the aperture function $\mathcal{P} = P(x,y)\exp[j\phi(x,y)]$

$$E_B \sim \mathcal{F}\{\mathcal{P}\} = \mathcal{F}\{P(x,y)\exp[j\phi(x,y)]\} \tag{5.2}$$

And since the Parseval-Plancherel theorem states the equivalence of the scalar product computed in the space domain and the frequency domain

$$\int_{-\infty}^{+\infty} f(x)\overline{g}dx = \int_{-\infty}^{+\infty} \mathcal{F}\{f(\xi)\}\overline{\mathcal{F}\{g(\xi)\}}d\xi \tag{5.3}$$

the coupling efficiency can be computed in the aperture plane

$$\rho = \frac{|\int\int_S E_A^*(x,y)F_A(x,y)ds|^2}{\int\int_S |E_A(x,y)|^2 ds \int\int_S |F_A(x,y)|^2 ds} \tag{5.4}$$

with $E_A(x,y)$ the electric field of the incoming light in aperture plane

$$E_A(x,y) = P(x,y)\exp[j\phi(x,y)] \tag{5.5}$$

,

$$P(x,y) = \begin{cases} 1, & \text{if } \alpha D_1/2 \leq \sqrt{x^2+y^2} \leq D_1/2 \\ 0 & otherwise \end{cases} \tag{5.6}$$

$\alpha = D_2/D_1$ the central obstruction and F_A the electric field of the mode LP_{01} back-propagated to the aperture plane.

As stated in the third chapter, the electric field of the fundamental mode is approximated by a Gaussian. Since the Fourier transform of a Gaussian function is also a Gaussian, the back-propagated electric field is given by [44]

$$F_A \sim \exp[-\left(\frac{r}{\omega_a}\right)^2] \tag{5.7}$$

with

$$\omega_a = \frac{\lambda f}{\pi\omega_0} \tag{5.8}$$

with f the focal length and ω_0 the mode radius defined by Equation 4.13.

In Figure 5.4, a schematic view of the single mode fiber at the focus of the telescope is displayed.

To simulate the coupling efficiency when the system is aberrated the definition of the overlap integral at the aperture plane is used. This definition has the advantage to avoid the computation of the Fourier transform of Zernike functions and their

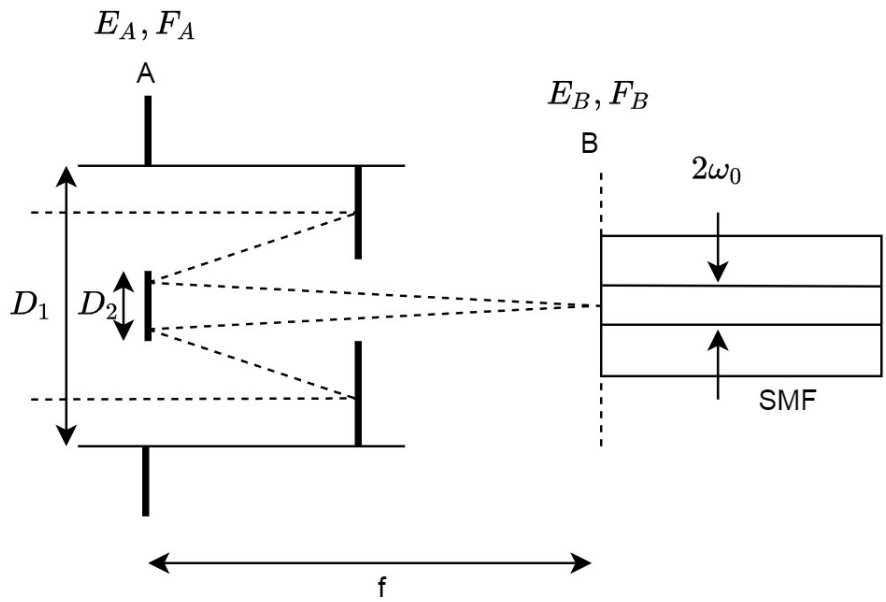

Figure 5.4: Schematic view of a single mode fiber at the focus of a telescope. E_A is the incoming electric field at the aperture, F_A the back-propagated fundamental mode of the SMF, E_B the electric field at the focus of the telescope, F_B the electric field of the fundamental mode of radius ω_0. D_1 represents the diameter of the aperture and D_2 the diameter of a central obstruction typical of a Cassegrain telescope.

numerical integrations projected on the fiber mode. Indeed, in chapter two, the aberrated phase Φ was decomposed in the Zernike circular polynomials $Z_i(r, \theta)$

$$\Phi(r, \theta) = \sum_{i=1}^{\infty} a_i Z_i(r, \theta) \tag{5.9}$$

In order to simplify the expression of the coupling efficiency, the electric field $F_A(x, y)$ can be normalized.

If

$$F_A(x, y) = \frac{2}{\sqrt{\pi \omega_a^2}} \exp\left[-\frac{x^2 + y^2}{\omega_a^2} \right] \tag{5.10}$$

then, the norm of F_A is

$$
\begin{aligned}
||F_A|| &= \sqrt{\int_{\infty} |F_A|^2 dA} \\
&= \frac{2}{\sqrt{\pi\omega_a^2}} \sqrt{\int_0^{2\pi} \int_0^{\infty} r \exp(-\frac{2r^2}{\omega_a^2}) dr d\theta} \\
&= \frac{2}{\sqrt{\pi\omega_a^2}} \sqrt{\frac{\pi\omega_a^2}{2}} \\
&= 1
\end{aligned}
\tag{5.11}
$$

and Equation 5.4 can be written

$$
\rho = \frac{1}{S} \left| \int\int_S P(x,y) \exp[j\phi(x,y)] \sqrt{\frac{2}{\pi\omega_a^2}} \exp\Big[-\frac{x^2+y^2}{\omega_a^2} \Big] ds \right|^2 \tag{5.12}
$$

Therefore, for the pupil operation

$$
\rho = \frac{2}{S\pi\omega_a^2} \left| \int_0^{2\pi} \int_{\alpha D_1/2}^{D_1/2} r \exp[j\phi(r,\theta)] \exp\Big[-\frac{r^2}{\omega_a^2} \Big] dr d\theta \right|^2 \tag{5.13}
$$

with $S = \pi(D_1/2)^2 - \pi(\alpha D_1/2)^2$

In the next chapter the system will be considered diffraction-limited. In such case $\Phi = 0$ and the coupling efficiency is giveny by

$$
\rho = \frac{2}{S\pi\omega_a^2} \left| \int_0^{2\pi} \int_{\alpha D_1/2}^{D_1/2} r \exp\Big[-\frac{r^2}{\omega_a^2} \Big] dr d\theta \right|^2 \tag{5.14}
$$

This integral admits an analytical solution giveny by [43]

$$
\rho(\alpha,\beta) = 2 \left[\frac{\exp(-\beta^2) - \exp(-\beta^2\alpha^2)}{\beta(1-\alpha^2)^{1/2}} \right]^2 \tag{5.15}
$$

with

$$
\beta = \frac{\pi}{2} \frac{D}{\lambda} \frac{\omega_0}{f} \tag{5.16}
$$

This solution will be used to optimize the coupling efficiency.

In chapter six, the coupling efficiency is studied when the system is subjected to static aberrations. The computation of the integral 5.13 will be performed with Matlab. It will allows us to determine the coupling efficiency in function of the standard deviation a_i for any Zernike polynomials. Also, the point spread functions will be computed thanks to the fast fourier transform (FFT) algorithm. Thanks to this code the coupling efficiency for typical phase aberrations encountered in space will be analysed. Finally, the coupling efficiency when a deformable mirror corrects some Zernike modes will be discussed.

Chapter 6

Diffraction limited design

This chapter aims to simulate the system free of aberrations.

The discussion begins with a study of the point spread function. To do so, the analytical expression of the PSF for a circular aperture with a central obstruction is used. Next, the electric field of the focused light and the LP_{01} mode are analysed for a better intuitive understanding of the injection problem. Finally the coupling efficiency is analysed.

6.1 General considerations

6.1.1 Point spread function

As mentioned previously the point spread function of an optical system is the square modulus of the impulse response h. This function characterizes the ability of the system to resolve a point like source and for this reason it is often used in optic design.

The PSF of a pupil of diameter D with a central circular obstruction α, at the distance z, for the observing wavelength λ is

$$PSF = \left(\frac{D^2}{4\lambda z}\right)^2 \left[\frac{J_1(2\pi\xi)}{\xi} - \alpha^2 \frac{J_1(2\pi\alpha\xi)}{\alpha\xi}\right]^2 \tag{6.1}$$

with $\xi = rD/(2\lambda z)$ and r the radial distance from the center in the observation plane.

In Figure 6.1 the PSF of an unobstructed pupil ($\alpha = 0$) of diameter $D = 1$ m is represented in 3D and 2D. The image plane is at $z = f = 3.83$ m and the wavelength is

$\lambda = 5\ \mu m$. The PSF is normalized by its pick value situated at the center. The figures shows the well known Airy pattern of concentric rings with a high concentration of energy within the first ring.

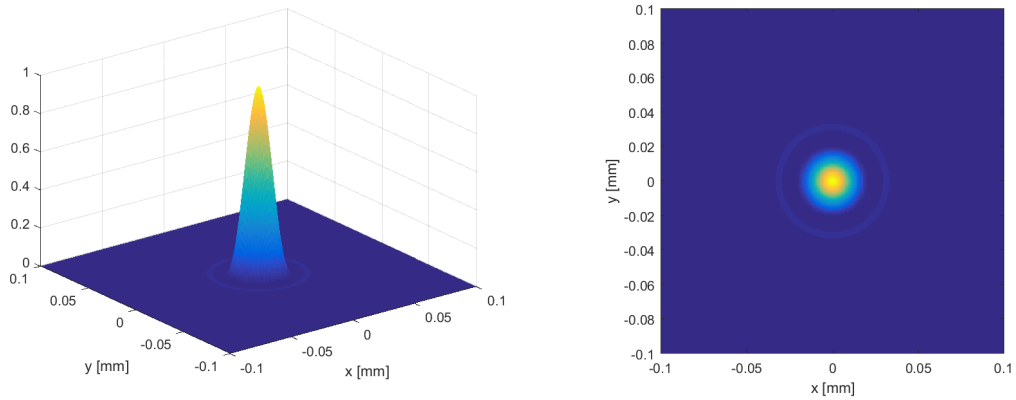

(a) 3D representation of the normalized PSF. (b) 2D representation of the normalized PSF.

Figure 6.1: PSF representations at focal distance $f = 3.83$ m for a primary mirror $D = 1$ m with no obstruction $\alpha = 0$ at the observing wavelength $\lambda = 5\ \mu$m.

In Figure 6.2 the PSF of a pupil of diameter $D = 1$ with a central obstruction $\alpha = 0.436$ m is represented in 3D and 2D. This value of the central obstruction corresponds to the one of the 3.6 m ESO telescope corrected with the ADONIS adaptive optics system at La Silla observatory [54]. The image plane is at $z = f = 4.48\ m$ and the wavelength is $\lambda = 5\ \mu m$. The PSF is normalized by its pick intensity situated at the center.
These figures show that the obstruction has the effect of reinforcing the side lobes of the Airy pattern. Therefore less energy is present within the first ring.

Moreover the obstruction has the effect of decreasing the overall energy since the obstruction blocks some photons. This effect can be seen in Figure 6.3 where the PSF are represented and both normalized by the pick intensity of the Airy pattern corresponding to $\alpha = 0$.

6.1.2 Electric field

Since the coupling efficiency depends on the electric field profile of the incoming light and the mode of the fiber LP_{01}, it is necessary to analyse them.

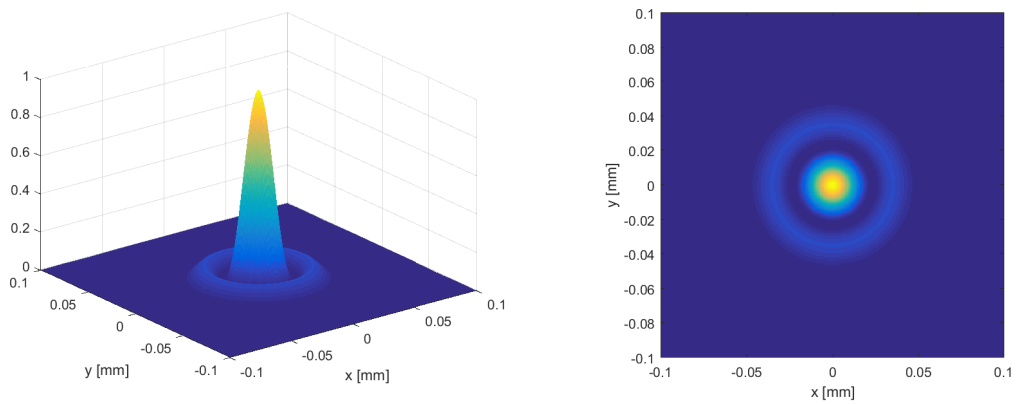

(a) 3D representation of the normalized PSF. (b) 2D representation of the normalized PSF.

Figure 6.2: PSF representations at focal distance $f = 4.48\ m$ for an aperture $D = 1\ m$ with a central obstruction $\alpha = 0.436$ at the observing wavelength $\lambda = 5\ \mu$m.

As said in the second chapter, the electric field at the focus of the telescope is given by the Fraunhofer diffraction pattern of the aperture function. It gives [50]

$$E_B(x,y) = \frac{\exp(jkz)}{j\lambda z} \exp\left[j\frac{k}{2z}(x^2+y^2)\right]\left(\frac{D^2}{4\lambda z}\right)\left[\frac{J_1(2\pi\xi)}{\xi} - \alpha^2\frac{J_1(2\pi\alpha\xi)}{\alpha\xi}\right] \tag{6.2}$$

On the other side, the electric field of the single mode fiber is given by the Gaussian approximation

$$F_B(x,y) = \frac{2}{\sqrt{\pi\omega_0^2}} \exp\left[-\frac{x^2+y^2}{\omega_0^2}\right] \tag{6.3}$$

In Figure 6.4 the normalized electric fields are represented. The dashed line in blue represents the electric field at the focus of the telescope E_B, where the fiber is situated. The solid line in red represents the fundamental mode of the fiber LP_{01}. The working wavelength, the focal distance, the aperture are the same as before. The obstruction α is 0 and the radius of LP_{01} is $\omega_0 = 13.7\ \mu$m.

The mismatch between the two profiles is clearly visible. It results in a loss of the coupling efficiency as explained previously. Moreover it can be seen that the mismatch is stronger at the first lobe which indicates that the presence of an obstruction will result in a loss of the coupling efficiency since the obstruction increase the size of the lobe.

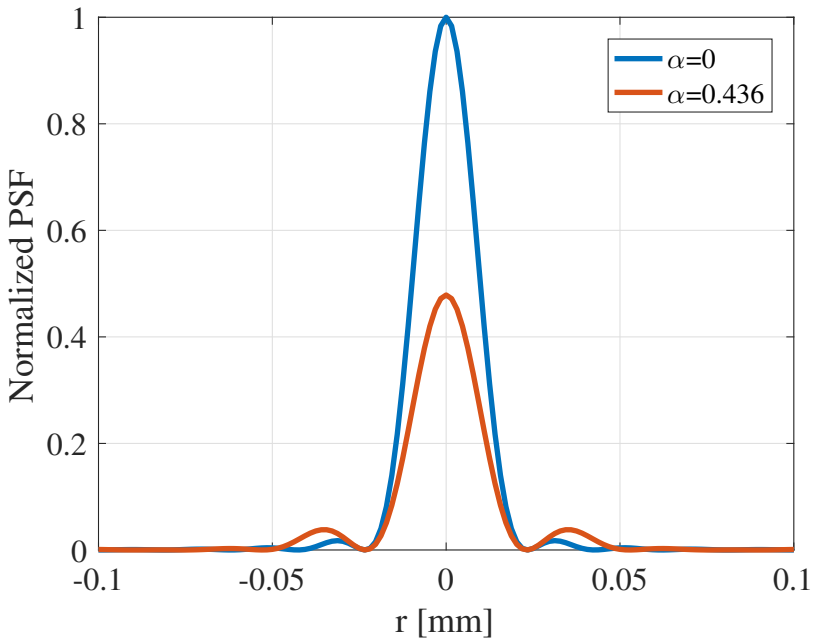

Figure 6.3: PSF normalized by the pic value of the unobstructed PSF in function of the radial distance. $\lambda = 5\ \mu m$, $D = 1\ m$. $f = 3.83\ m$ for $\alpha = 0$ and $f = 4.48\ m$ for $\alpha = 0.436$.

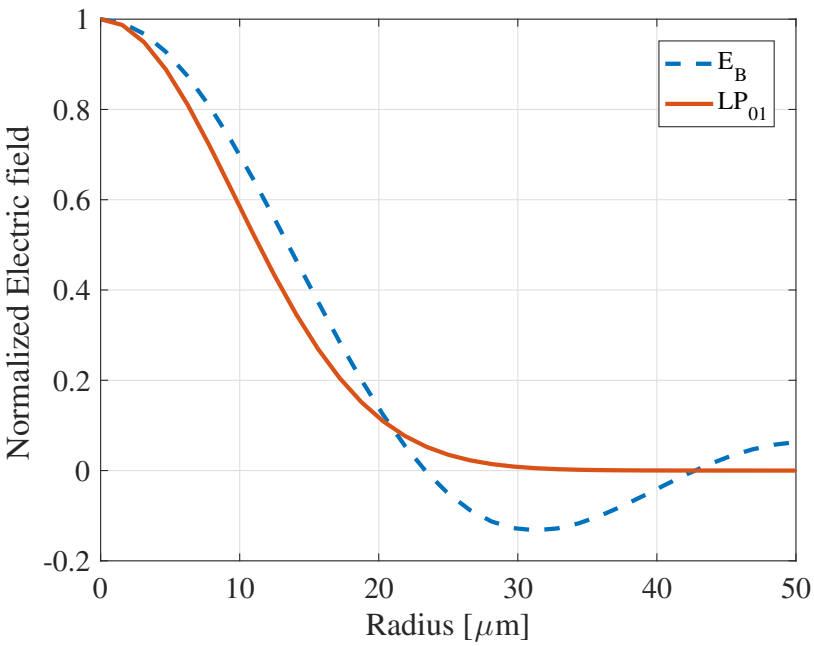

Figure 6.4: Comparison between the normalized electric field at the focus of the telescope E_B and the normalized mode of the fiber LP_{01} in function of the radial distance. $\alpha = 0$, $f = 3.83\ m$, $\omega_0 = 13.7\ \mu$m, $\lambda = 5\ \mu$m, $D = 1\ m$. The mismatch of the two profiles explains the loss of energy at the output of the fiber.

6.1.3 Coupling efficiency

If a perfect plane wave of wavelength λ reachs a pupil of diameter D with a circular central obstruction α, and focuses at the distance f on a single mode fiber, an analytical expression of the coupling efficiency, for the Gaussian approximation $LP_{01} \sim \exp(\frac{-r^2}{\omega_0^2})$, exists and is given by [43]:

$$\rho(\alpha, \beta) = 2\left[\frac{\exp(-\beta^2) - \exp(-\beta^2\alpha^2)}{\beta(1-\alpha^2)^{1/2}}\right]^2 \tag{6.4}$$

with

$$\beta = \frac{\pi}{2}\frac{D}{\lambda}\frac{\omega_0}{f} \tag{6.5}$$

This formula stipulates that the coupling efficiency is function of five parameters: α, D, λ, f, ω_0. Four of them are sum up into one, β.

In Figure 6.5, $\rho(\alpha, \beta)$ is represented for different values of the central obstruction α : $\alpha = 0$, $\alpha = 0.25$, $\alpha = 0.436$, corresponding to DKIST telescope [56], HST [57] and 3.6 ESO telescope respectively.

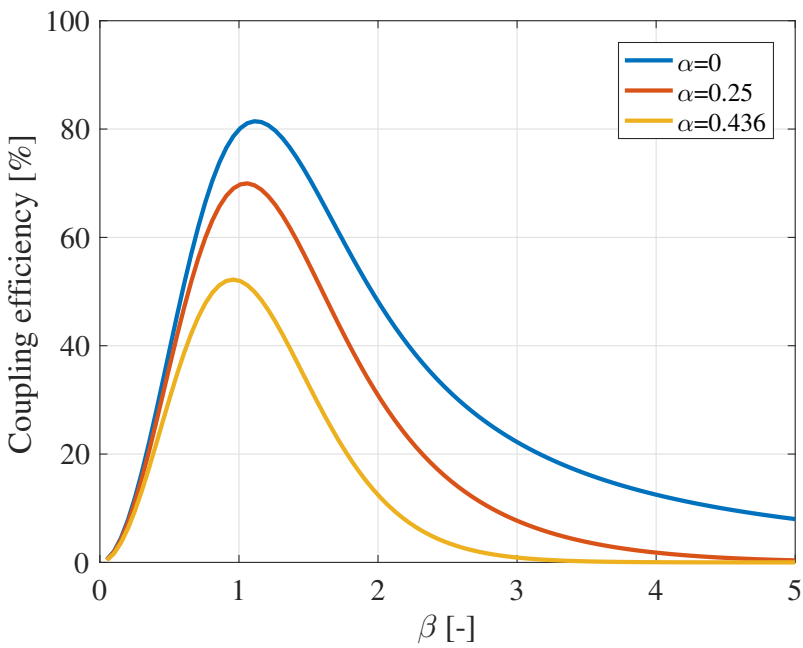

Figure 6.5: Coupling efficiency in function of β for different value of the obstruction α.

The figure shows that for a fixed central obstruction the coupling efficiency has a maximum value for one β. This value of β tends to decrease when α increases. Also, when the central obstruction increases the maximum coupling efficiency decreases. It confirms what was established earlier on the effect of α. The maximum achievable coupling efficiency is when $\alpha = 0$. Indeed for no central obstruction, the coupling efficiency is 81.45% for $\beta = 1.12$. It means that, to get the maximum coupling efficiency, α, D, λ, f and ω_0 have to be designed such that

$$\beta = \frac{\pi}{2}\frac{D}{\lambda}\frac{\omega_0}{f} = 1.12 \tag{6.6}$$

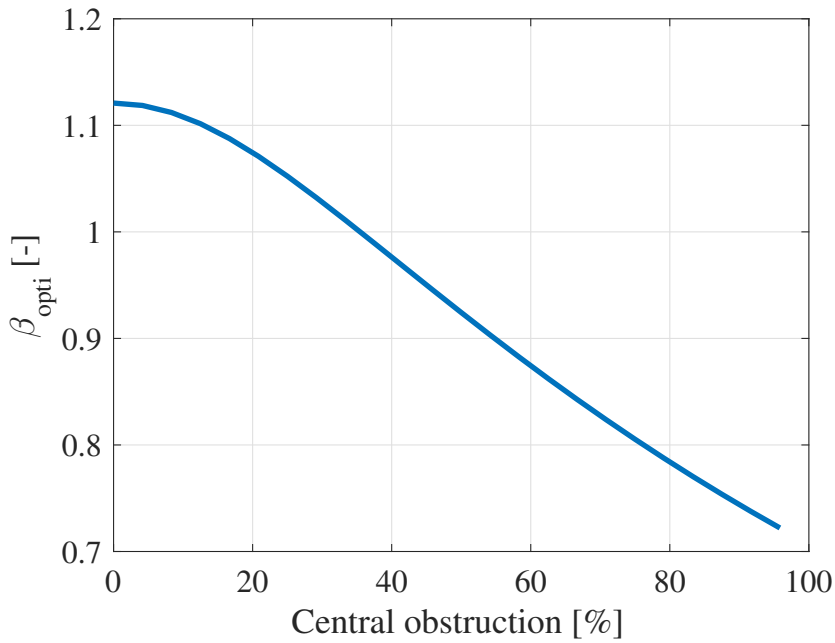

Figure 6.6: Value of β that maximizes the coupling efficiency in function of the central obstruction.

Therefore, β can be seen as the design parameter that needs to be optimized, for a fixed central obstruction, in order to achieve the best injection into the single mode fiber. On the other hand, the central obstruction is the parameter that sets the physical limit of the achievable coupling efficiency. The optimized value of β in function of the central obstruction is displayed in Figure 6.6.

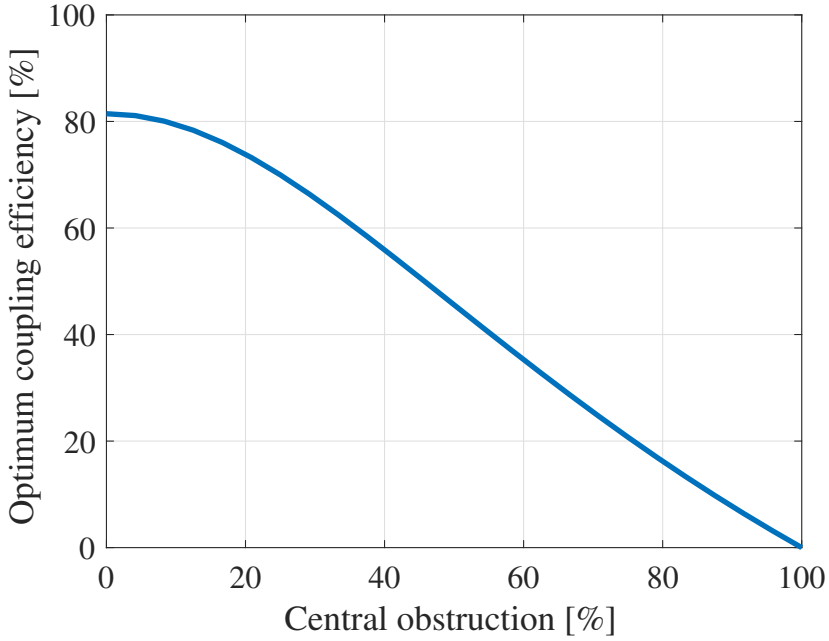

Figure 6.7: Optimum coupling efficiency in function of the central obstruction at cutoff frequency

In Figure 6.7 is represented the optimum coupling efficiency in function of the central obstruction. This value of ρ is obtained by taking the optimum design parameter β_{opti} for each α.

It shows that the coupling efficiency is maximum for $\alpha = 0$ (i.e. when there is no obstruction) and is null for $\alpha = 1$ (i.e. when the diameter of the obstruction equals the diameter of the primary mirror). The maximum is 81.45% as mentioned previously. It shows that the decrease of ρ is small for $\alpha < 20\%$ where at this stage ρ has dropped of only 8%. Then the optimum ρ decreases linearly. For $\alpha = 40\%$ the optimum ρ has lost around 25%.

This value of 81.45 % differs from the theoretical value of 78 % that was stated in the first chapter. This difference is due to the Gaussian approximation and the fact that the Fresnel reflection on the head's fiber was not considered in the model [43].

6.2 Design of the f-number

As stated in chapter three, the fiber is single mode only if the normalized frequency $V = \frac{2\pi a NA}{\lambda} \leq 2.405$. Moreover, in the same chapter, it was said that the Gaussian approximation of the mode LP_{01} is good only near cutoff frequency $V_c = 2.405$. For these reasons it would be a good idea to fix the normalized frequency to 2.405.

However V is function of the wavelength and as stated in chapter 4 it was decided to work on the waveband $[3-7]$ μm. Consequently, it is not possible to fix $V = \frac{2\pi aNA}{\lambda} = 2.405$ in the waveband unless aNA equals $\frac{2.405\lambda}{2\pi}$ for every λ in the waveband. Naturally the core radius and the numerical aperture can not be variable. They are fixed during the design and do not change afterwards. However it was decided to study two different cases. The first one, the numerical aperture is fixed to $NA = 0.16$ and the core diameter a is variable. a is chosen such that $V = 2.405$ for all the wavelength in the waveband. Therefore it is an ideal case. The second case represents a realistic scenario where the core radius is fixed. Here again NA is fixed to 0.16.

6.2.1 Case 1: the core radius is variable

To fix the normalized frequency at 2.405 for all the wavelengths, the core radius is artificially adapted according to

$$a = \frac{2.405\lambda}{2\pi NA} \tag{6.7}$$

Figure 6.8 displays the core radius a in function of the wavelength for a numerical aperture $NA = 0.16$. It shows the linear relation between the core radius and the wavelength. The order of magnitude of a is the micron in the infrared region.

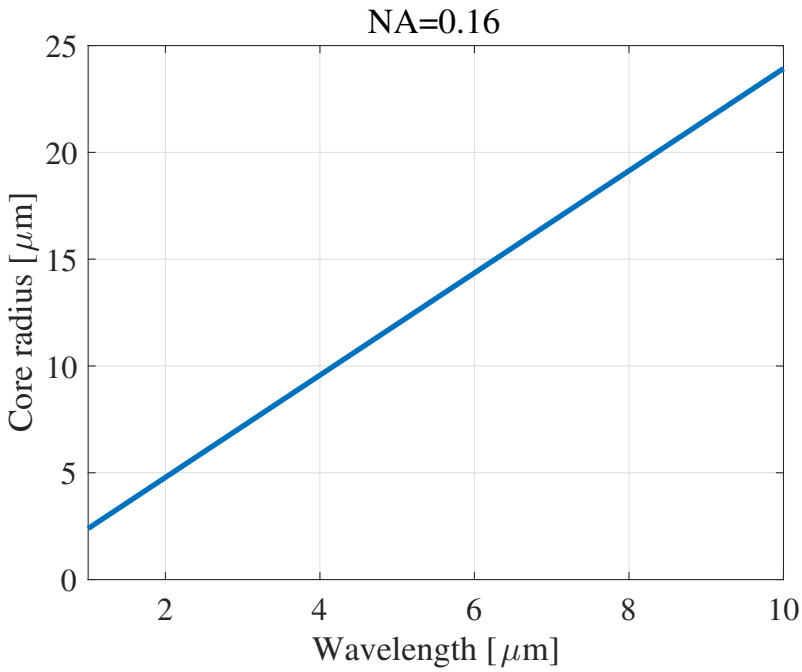

Figure 6.8: Optimum core radius in function of wavelength

An interesting consequence is that the coupling efficiency is independent of the wavelength. As stated earlier, the coupling efficiency is function of α and $\beta = \frac{\pi}{2}\frac{D}{\lambda}\frac{\omega_0}{f}$ according to Equation 6.4. So one would expect a coupling efficiency varying with λ since β is function of λ.

However, according to the definition of ω_0

$$\begin{aligned} w_0 &= a\left(0.65 + \frac{1.619}{V^{3/2}} + \frac{2.879}{V^6}\right) \\ &= \frac{2.405\lambda}{2\pi NA}\left(0.65 + \frac{1.619}{V^{3/2}} + \frac{2.879}{V^6}\right) \end{aligned} \tag{6.8}$$

This results in

$$\begin{aligned} \beta &= \frac{\pi}{2}\frac{\omega_0 D}{\lambda f} \\ &= \frac{\pi D}{2\lambda f}\frac{2.405\lambda}{2\pi NA}\left(0.65 + \frac{1.619}{V^{3/2}} + \frac{2.879}{V^6}\right) \\ &= \frac{2.405}{4NA}\frac{D}{f}\left(0.65 + \frac{1.619}{V^{3/2}} + \frac{2.879}{V^6}\right) \end{aligned} \tag{6.9}$$

which is independent of the the wavelength since $V = 2.405$ and $NA = 0.16$.

Therefore, the coupling efficiency is only dependant of α and the f-number. The central obstruction will fix the maximum coupling achievable and the performance of the system will depend on the choice of f/D.

In Figure 6.9 the coupling efficiency in function of the f-number is represented for different value of the central obstruction α. It shows that f/D increases when the obstruction increases. It is coherent with the discussion on the Figure 6.5 since $f/D \sim 1/\beta$.

In Figure 6.10 the f-number in function of the central obstruction is displayed. This optimum f-number corresponds to the value of f/D for which β maximize $\rho(\alpha, \beta)$ when the core radius is adapted to work at the cutoff frequency. It can be seen that for no central obstruction the optimum f-number equals 3.68 and increases with α. Note that the optimum f-number is not defined for a central obstruction $\alpha = 1$ since no light reachs the fiber and therefore the coupling efficiency equals zero no matter what the value of f/D is.

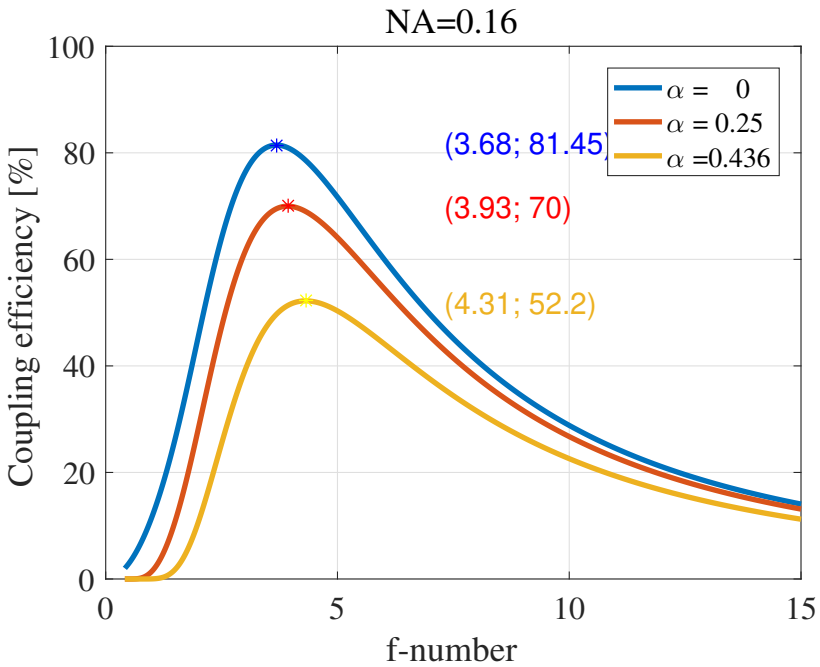

Figure 6.9: Coupling efficiency in function of the f number for different value of the obstruction α.

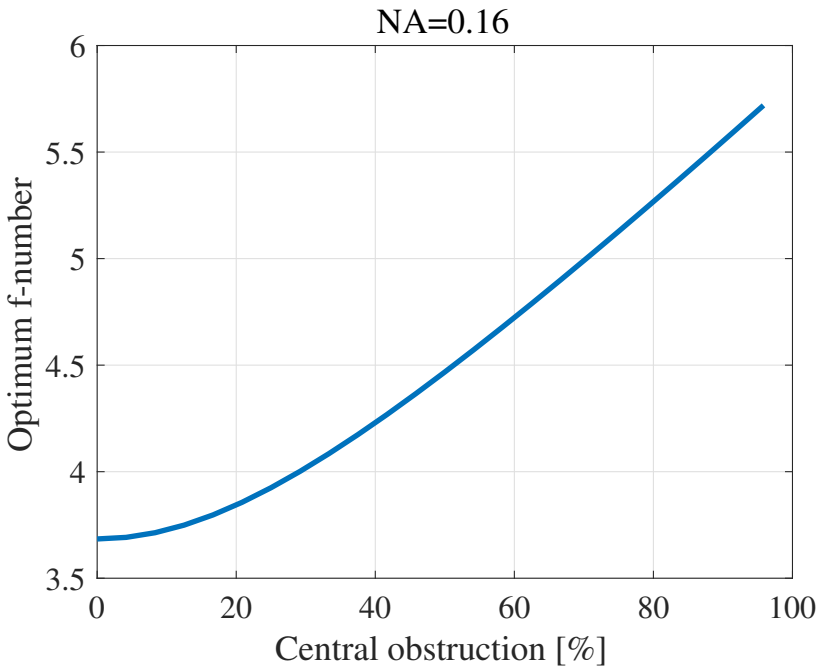

Figure 6.10: Optimum f-number in function of the central obstruction.

6.2.2 Case 2: the core radius is fixed

As discussed before, in a real system the core radius can not be adjusted to every wavelengths of the waveband of observation. This means that the result of the independence of coupling efficiency according to wavelength is no longer true. The direct consequence of this is that the coupling efficiency can not be optimized for every wavelength in [3-7] μm. It can be optimum only in a finite wavelength, which need to be specified, by optimizing the focal length.

Therefore, when it comes to the design of a SMF at the focus of a telescope, one must choose a wavelength and find the f-number which maximizes the coupling efficiency at this wavelength. Generally, it is convenient to optimize the coupling efficiency for the middle of the wavelength range [53]. For this study since it is proposed the operating waveband [3-7] μm, the coupling efficiency is optimized at 5 μm.

Now, the core radius of the fiber must be designed. In this case the core radius is chosen in order to work in the single mode regime for the all bandwidth of observation. It means that, in order to propagate only the fundamental mode of the fiber, the normalized frequency needs to be smaller than the cutoff one. It means that

$$\lambda > \lambda_c = \frac{2\pi a NA}{2.405} \tag{6.10}$$

Then, by imposing $\lambda_c = 3\ \mu m$, it allows to stay in single-mode condition in all the waveband of observation $[3-7]\ \mu m$. It means that the core radius is given by

$$a = \frac{3 * 2.405}{2\pi NA}\mu m = 7.18\mu m \tag{6.11}$$

Contrary to before, the normalized frequency V is not constant but takes value between [1.03-2.405].

Now that the core radius is fixed, the coupling efficiency depends on the wavelength and the optimal f-number too. The effect of the wavelength on the optimum f-number can be seen in Figure 6.11.
The figure shows that the the optimum f-number increases when λ increases. Also f/D increases when the obstruction ratio increases.

Moreover, the figure highlights the fact that at $\lambda = 5\ \mu m$ the optimum $f/D = 3.82$ is larger than the f-number obtained previously for an adaptive core radius. Indeed, when a was artificially adjusted such that $V = 2.405$ for all λ, the f-number was $f/D = 3.68$.
This is coherent with the fact that the optimum coupling efficiency, for a some obstruction, occurs at one $\beta = \beta_{opti}$. Since $\beta = \frac{\pi}{2}\frac{D}{\lambda}\frac{\omega_0}{f} \sim \frac{D}{f}(0.65 + \lambda^{1/2} + \lambda^5)$. That means that for $\lambda > \lambda_c = 3\mu m$, f/D needs to increase to stay at this β.

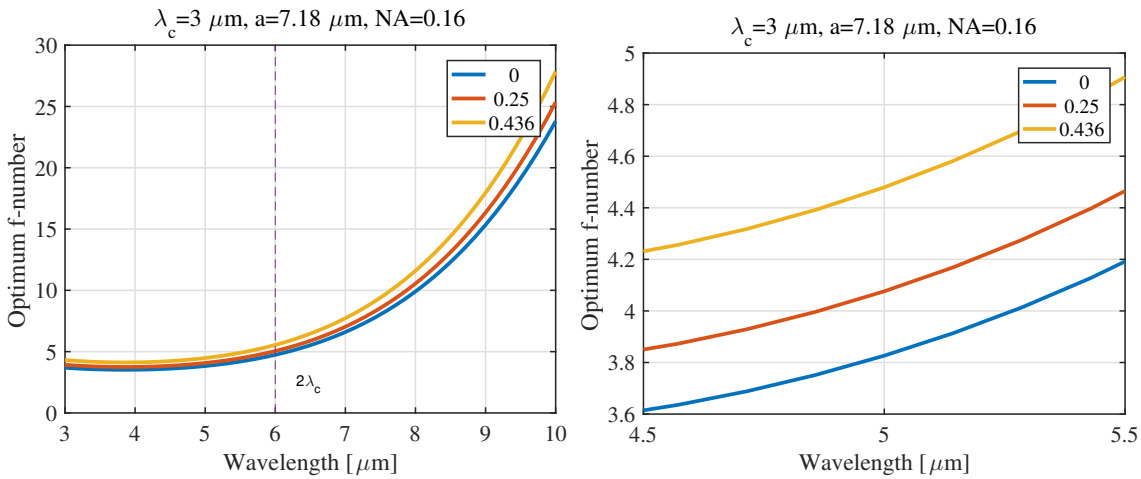

Figure 6.11: Optimum f-number in function of the wavelength λ for different value of the obstruction α.

Table 6.1 summarizes the results of the optimum f/D that maximizes the coupling efficiency.

	$\lambda = \lambda_c = 3\mu m$	$\lambda = 5\mu m$
$\alpha = 0$	$f/D = 3.68$	$f/D = 3.82$
$\alpha = 0.25$	$f/D = 3.93$	$f/D = 4.08$
$\alpha = 0.436$	$f/D = 4.31$	$f/D = 4.48$

Table 6.1: Comparison of f-number

In Figure 6.12 the coupling efficiency in function of the wavelength is displayed for different values of the obstruction when the f-number is optimized at $\lambda = 5\ \mu m$. It shows that the maximum occurs effectively at $\lambda = 5\ \mu m$ as it was designed. Moreover the optimum coupling efficiency seems to be constant over $[\lambda_c\ 2\lambda_c]$ and starts to decrease greatly.

For $\alpha = 0$ the maximum coupling efficiency drops from 81.45% at $\lambda = 5\ \mu m$ to 51% at $\lambda = 7\ \mu m$. For $\alpha = 0.25$ it drops from 70% at $5\mu m$ to 39% at $7\mu m$. Finally for $\alpha = 0.436$ it drops from 52% to 25.4%.
To end this study note that the coupling efficiency drops to zero for $\lambda > 3\lambda_c$ for central obstructions higher than 0.25.

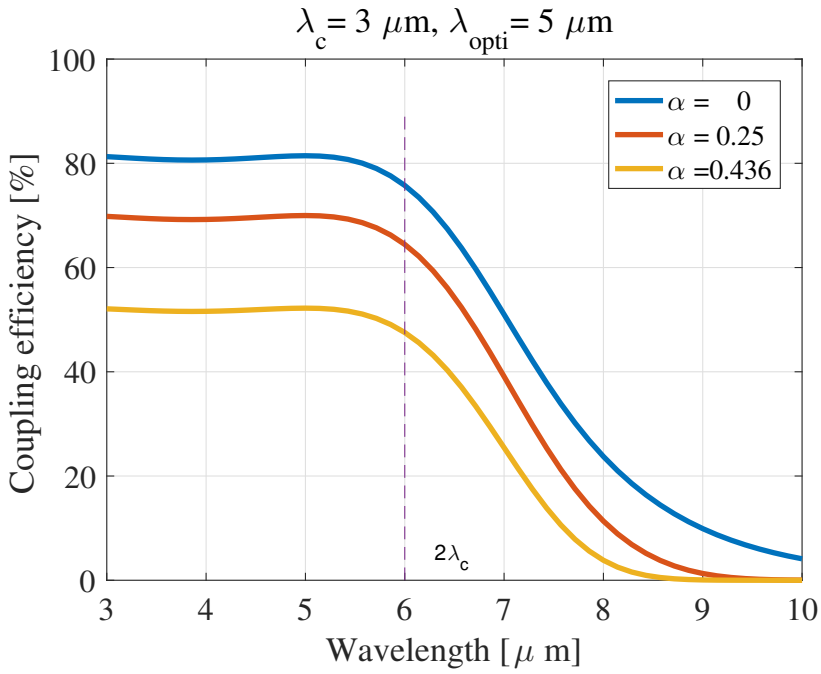

Figure 6.12: Coupling efficiency in function of wavelength for different values of the obstruction α.

6.3 Conclusion

In this chapter the coupling efficiency of a single mode fiber placed at the focus of a telescope was studied. The effect of a central obstruction was analysed and revealed to be the first limiting parameter of the performance. The simulations showed that under the Gaussian approximation the maximum coupling efficiency achievable was 81.45% when there is no central obstruction.
The effect of the wavelength was also studied when the fiber is optimized at the middle of the waveband : 5 μm. The simulations showed that a significant drop of the coupling efficiency takes place when $\lambda > 2\lambda_c$. For example at the extremity of the waveband, $\lambda = 7$ μm the coupling efficiency is 50% for a pupil with no central obstruction.

Chapter 7

Study of static aberrations

In this chapter the effect of static aberrations on the coupling efficiency is studied. The aberrations considered here are the Zernike polynomials $Z_i(r, \theta)$ as introduced in chapter two. The strength of the aberration is represented by the Zernike expansion coefficient a_i and equals to the root mean square σ_{rms} if the aberration is the only one affecting the wavefront.

Here the coupling efficiency are normalized by the optimized value obtained in the diffraction limited case when $\alpha = 0$: 81.45 %.

Also, the normalized coupling efficiency are compared to an analytical approximation given by [43]. This approximation, valid for small aberrations, states that

$$\rho = \rho_0 \exp(-\sigma_{rms}^2) \tag{7.1}$$

with ρ_0 the coupling efficiency when the system is not aberrated.

The chapter starts by a study of the effect of the RMS wavefront error (σ_{rms}) for differents aberrations. Then the effect of the obstruction is analysed. Next the effect of the wavelength. Finally the system is analysed when the wavefront has a phase map typical of the one encountered in space. The effect of the correction of some Zernike polynomials by a deformable mirror is also analysed.

7.1 Effect of the aberration's strength

In this section the effect of σ_{rms} for several aberrations is analysed.

The pupil is not obstructed ($\alpha = 0$) and the SMF is optimized. The simulations are done at the wavelength where the fiber is optimized: 5 μm.

7.1.1 Piston

The piston is the only aberration that is not corrected by the single mode fiber. Indeed, the piston only introduces a phase delay to a wave plane. Therefore, the electric field at the input of the fiber is injected in the same way than a wave plane and the coupling efficiency equals to the one obtained in the diffraction limited case.

7.1.2 Tip/Tilt

Tip/tilt aberrations are the ones who shift the PSF in the two orthogonal directions on the focal plane. Therefore, they represent aberrations like misalignment or pointing errors. In Figure 7.1 the point spread function of a unobstructed circular pupil aberrated by a tilt is represented and compared to the diffraction limited PSF.

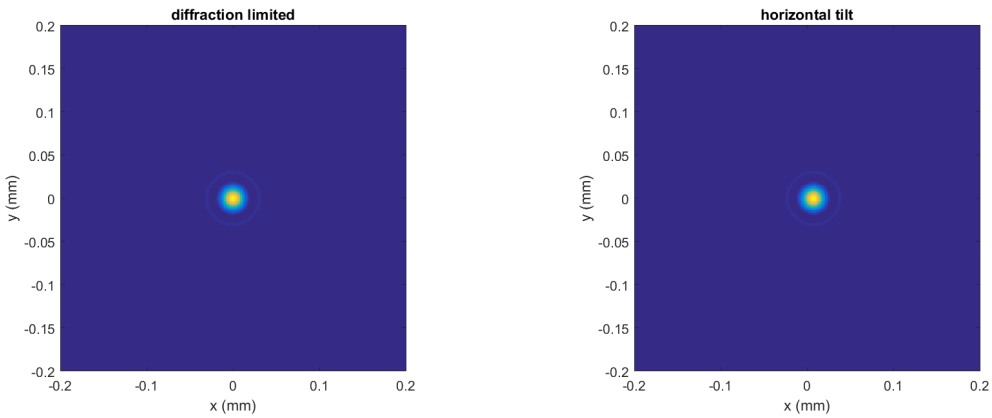

(a) Point spread function of an unobstructed circular pupil when the system is not aberrated.

(b) Point spread function of an unobstructed circular pupil when the system has a horizontal tilt (tip).

Figure 7.1: Comparison of the PSF of unobstructed circular pupil when the system is not aberrated and aberrated by a tilt. The only effect of the tilt is to shift the PSF.

This shift of the center of the PSF induces necessarly a loss of coupling efficiency. The effect of horizontal tilt can be seen on Figure 7.2. It shows that the coupling efficiency decreases slowly when $\sigma_{rms} < 0.5\ rad$. Then the coupling efficiency decreases linearly until $\sigma_{rms} = 1.5\ rad$. After this RMS value, the coupling decreases slowly.

Note that the effect of horizontal and vertical tilt are the same on the coupling efficiency. Indeed, in Figure 7.3 the two curves are superposed. This due to the

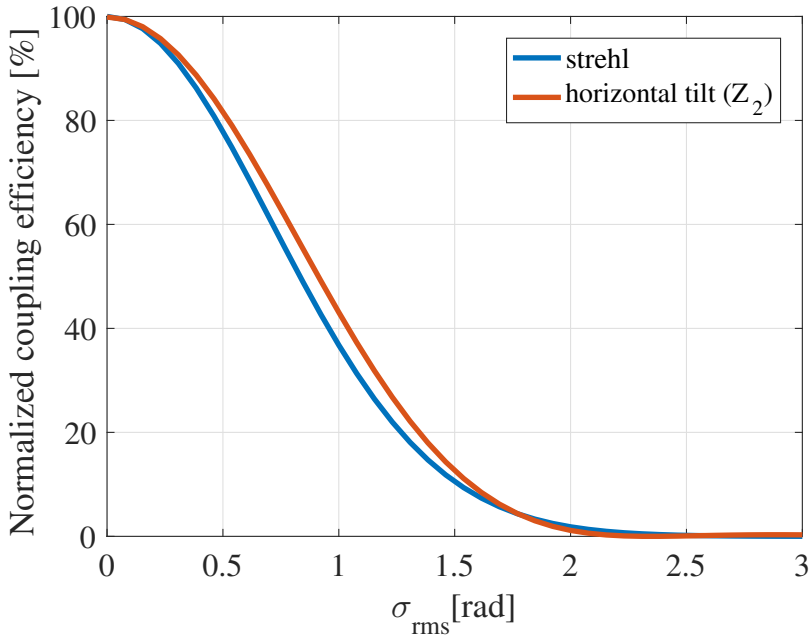

Figure 7.2: Normalized coupling efficiency in function of the RMS wavefront error for horizontal tilt.

symmetry of the Gaussian shape of the fundamental mode.

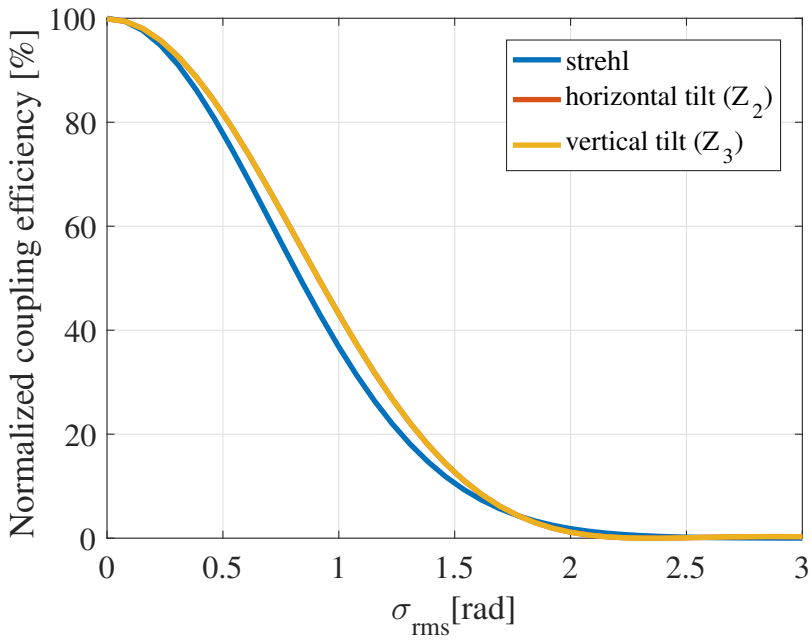

Figure 7.3: Normalized coupling efficiency in function of the RMS wavefront error for horizontal and vertical tilt.

7.1.3 Defocus and spherical aberrations

Another types of aberrations considered are defocus Z_2^0 and spherical aberrations Z_4^0. Theses aberrations are independent of the angular coordinate θ. Indeed, they are characterized by an azimutal order $m = 0$ which implies

$$Z_i(r, \theta) = \sqrt{n+1} R_0^n(r) = Z_i(r, \theta) \tag{7.2}$$

In Figure 7.4 the PSF of an unobstructed circular pupil when the system has defocus and spherical aberration is displayed. It shows that the PSF are circularly symmetric.

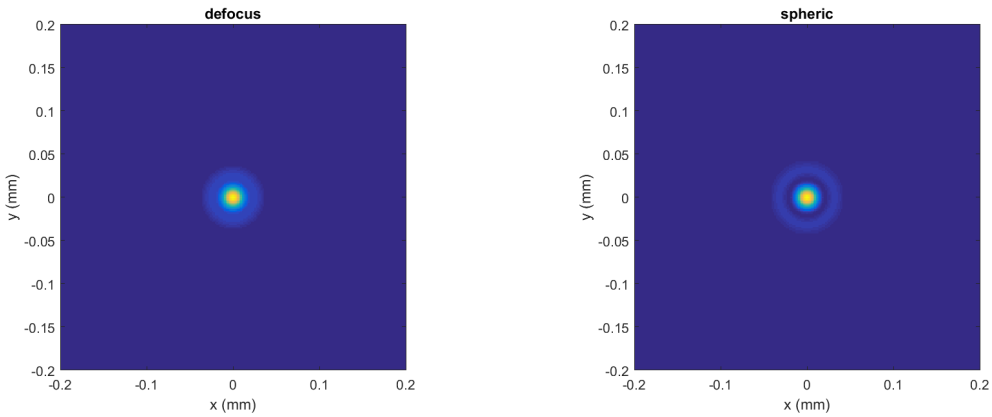

(a) Point spread function of an unobstructed circular pupil when the system has defocus aberration.

(b) Point spread function of an unobstructed circular pupil when the system has spherical aberration.

Figure 7.4: Comparison of the PSF of unobstructed circular pupil when the system has a defocus and a spherical aberration. The two PSF preserve their symmetry.

The effect of defocus and spherical aberration on the normalized coupling efficiency is displayed in Figure 7.5. It shows that for $\sigma_{rms} \leq 1.5\ rad$ the two aberrations have the same effect. Moreover they closely follow the Strehl approximation. Beyond $\sigma_{rms} = 1.5$, the effect of the aberrations seems to differ. Indeed, the effect of the defocus is stronger than the spherical aberration.

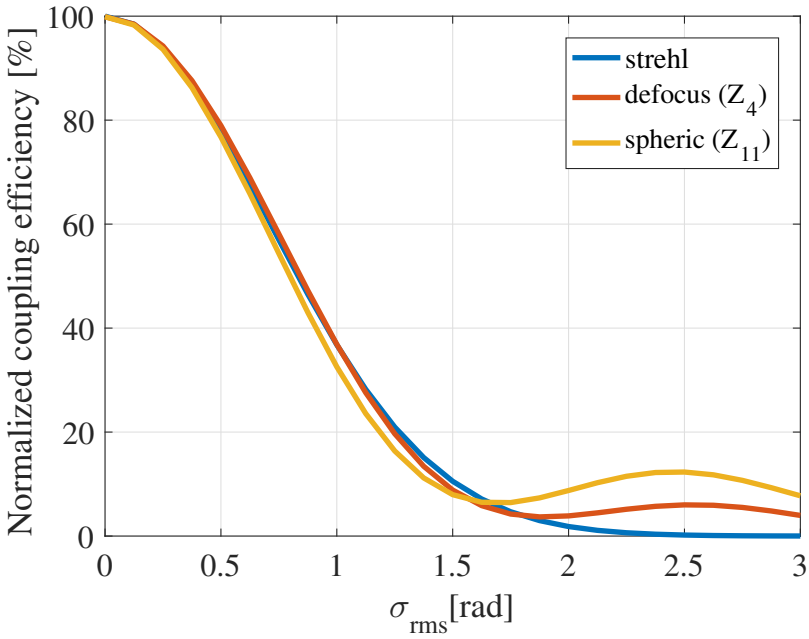

Figure 7.5: Normalized coupling efficiency in function of the RMS wavefront error for defocus and spheric aberration.

7.1.4 Coma aberrations

Here the effect of coma is analysed. In Figure 7.6 the PSF of an unobstructed circular pupil when the system has horizontal coma and 2nd-order coma is displayed. It shows that the PSF are asymmetric. Their effect on the coupling efficiency is displayed in Figure 7.7. The figure shows that these two aberrations have the same effect on the coupling efficiency. Also they closely follow the Strehl approximation.

In Figure 7.8 the effect of the two 2nd-order coma is displayed. It shows that the two aberrations have exactly the same effect since the curves are superposed. Therefore, this behaviour is the same as for the tilt. In fact, the symmetry of the Gaussian shape of the fundamental mode makes any Zernike polynomials, with same radial order and opposite azimutal order, to have the same effect on the coupling efficiency. Indeed, two Zernike polynomials Z_n^m and Z_n^{-m} have the same radial function R_n^m

$$R_n^m(r) = \sum_{l=0}^{(n-m')/2} \frac{(-1)^l (n-l)!}{l!\Big[(n+m')/2-l\Big]!\Big[(n-m')/2-l\Big]!} r^{n-2l} \tag{7.3}$$

with $m' = |m|$. On the other hand, the angular function is

$$\begin{aligned} Z_i(r,\theta) &= \sqrt{n+1} R_n^m(r) \sqrt{2} \cos(m'\theta), \quad \text{if } m > 0, \text{ i even} \\ Z_i(r,\theta) &= \sqrt{n+1} R_n^m(r) \sqrt{2} \sin(m'\theta), \quad \text{if } m < 0, \text{ i odd} \end{aligned} \tag{7.4}$$

These two functions are the same but shifted by $\pi/2$. Therefore, when it comes to the projection on the LP_01 mode and the integration over $[0-2\pi]$ it gives the same results.

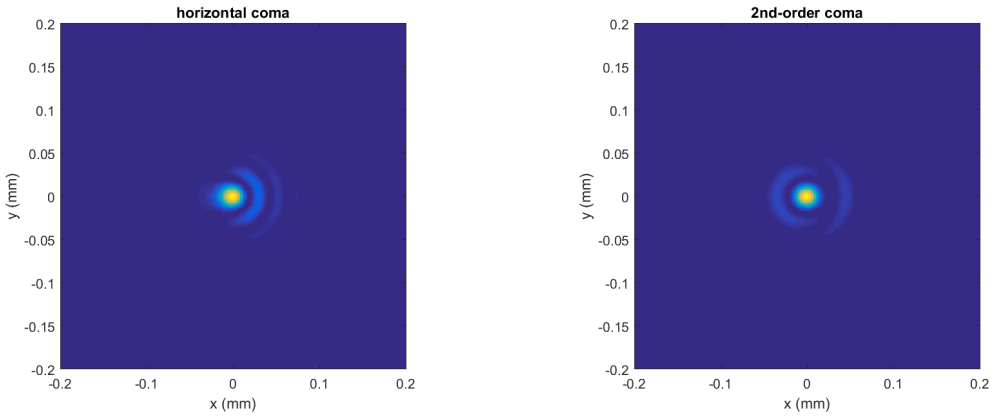

(a) Point spread function of an unobstructed circular pupil when the system has horizontal coma.

(b) Point spread function of an unobstructed circular pupil when the system has 2nd-order coma.

Figure 7.6: Comparison of the PSF of unobstructed circular pupil when the system has a defocus and a spherical aberration. The two PSF preserve their symmetry.

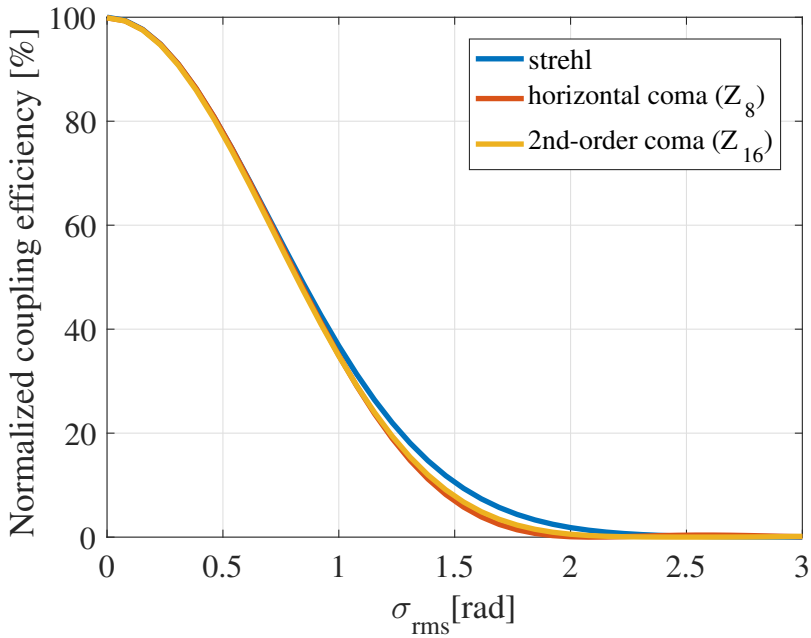

Figure 7.7: Normalized coupling efficiency in function of the RMS wavefront error for horizontal coma and 2nd-order coma.

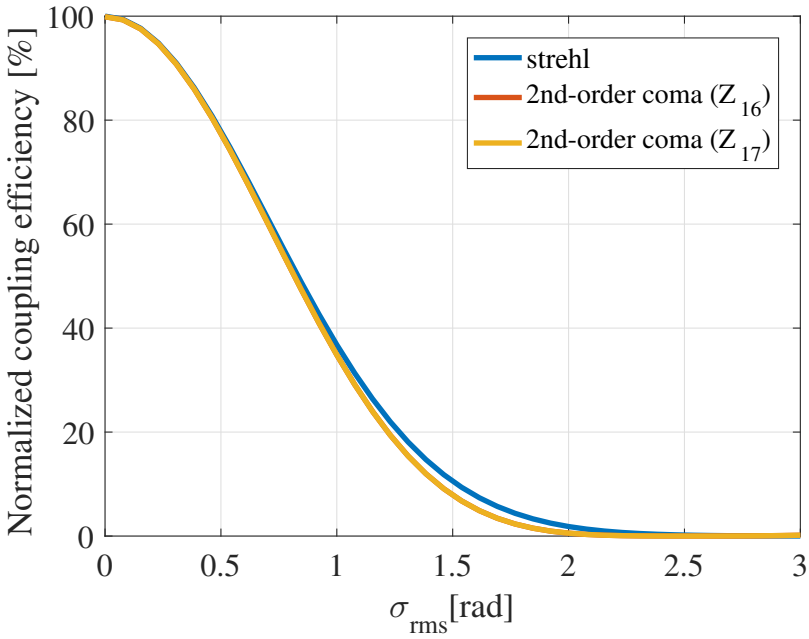

Figure 7.8: Normalized coupling efficiency in function of the RMS wavefront error for 2nd-order coma.

7.1.5 Astigmatism aberrations

In Figure 7.9 the PSF of an unobstructed circular pupil when the system has oblique astigmatism and vertical 2nd-order astigmatism is displayed. In Figure 7.10 the effect of oblique astigmatism and vertical 2nd-order astigmatism is displayed. It shows that 2nd-order astigmatism closely follows the Strehl approximation. On the other side the coupling efficiency is less affected by oblique astigmatism.

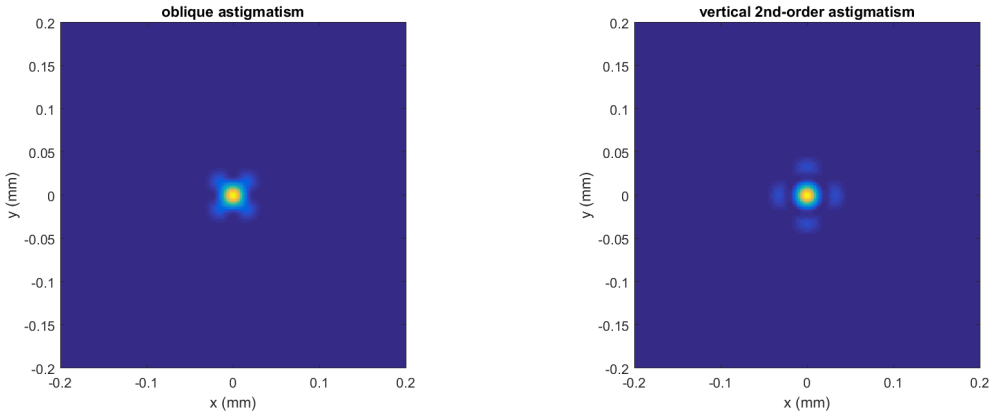

(a) Point spread function of an unobstructed circular pupil when the system has oblique astigmatism.

(b) Point spread function of an unobstructed circular pupil when the system has vertical 2nd-order astigmatism.

Figure 7.9: Comparison of the PSF of unobstructed circular pupil when the system has oblique astigmatism and vertical 2nd-order astigmatism.

7.1.6 Other types of aberrations

In Figure 7.11, is displayed the PSF of an unobstructed circular pupil when the system is subjected to oblique trefoil, quadrafoil and pentafoil. The effect of these aberrations on the coupling efficiency is visible in Figure 7.12. It shows that the aberrations are significantly less impacting the coupling efficiency. For example for $\sigma_{rms} = 1.5\ rad$ the coupling efficiency is 40% for a quadrafoil and 10% for the Strehl approximation. Also, the effect of the aberration seems to be weaker when the order j of the polynomial Z_j increases.

7.1.7 Conclusion

In conclusion the coupling efficiency seems to be more affected by circular symmetric aberration like defocus and spherical aberration, tilt, coma and 2nd-order astigmatism.

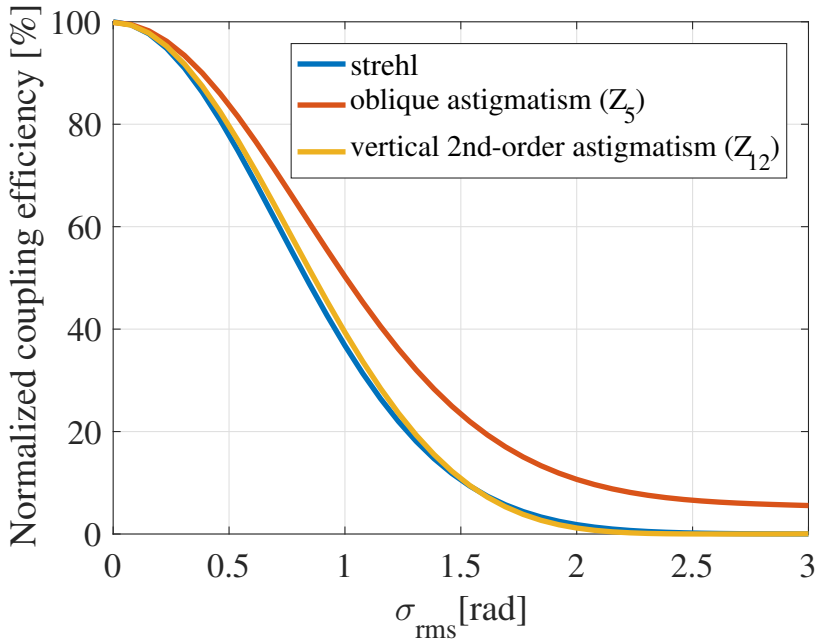

Figure 7.10: Normalized coupling efficiency in function of the RMS for oblique astigmatism and vertical 2nd-order astgmatism.

A summary of the effect of static aberrations on the coupling efficiency is visible in Figure 7.13.

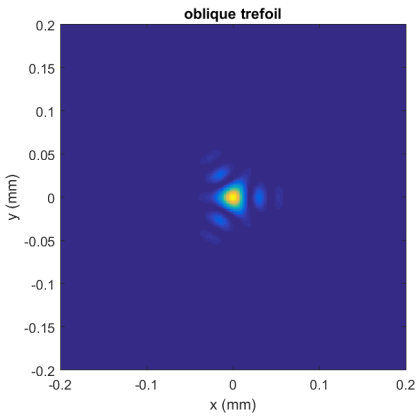

(a) Point spread function of an unobstructed circular pupil when the system has oblique trefoil aberration.

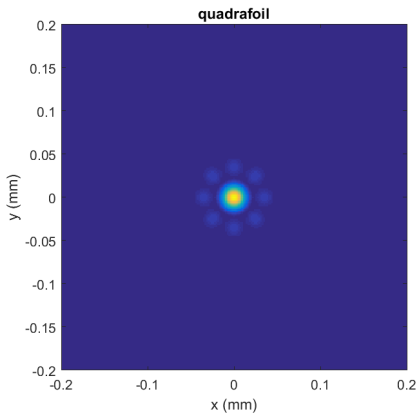

(b) Point spread function of an unobstructed circular pupil when the system has quadrafoil aberration.

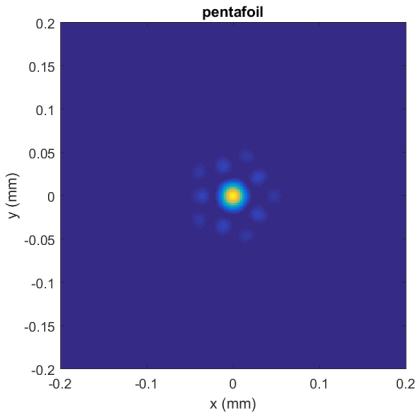

(c) Point spread function of an unobstructed circular pupil when the system has pentafoil aberration.

Figure 7.11: Comparison of the PSF of unobstructed circular pupil when the system has a defocus and a spherical aberration. The two PSF preserve their symmetry.

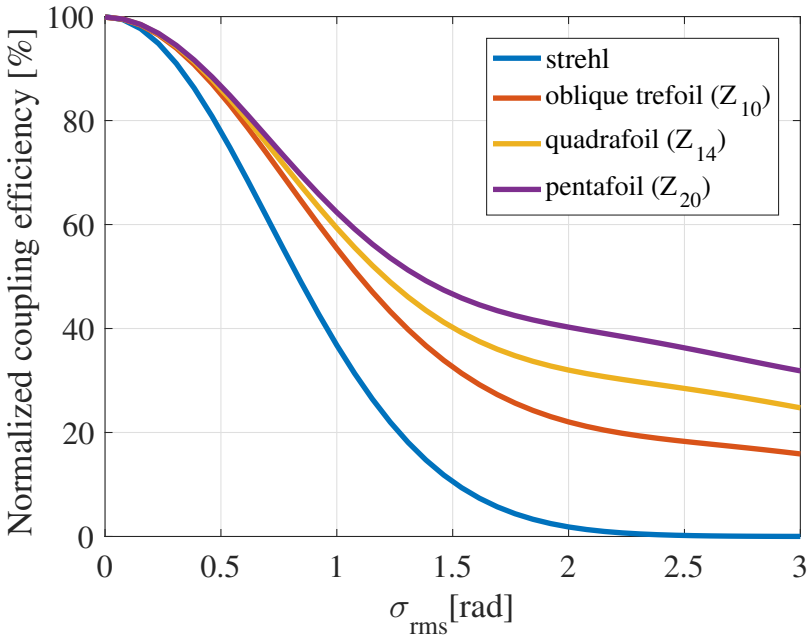

Figure 7.12: Normalized coupling efficiency in function of the wavefront RMS error for oblique trefoil, quadrafoil and pentafoil.

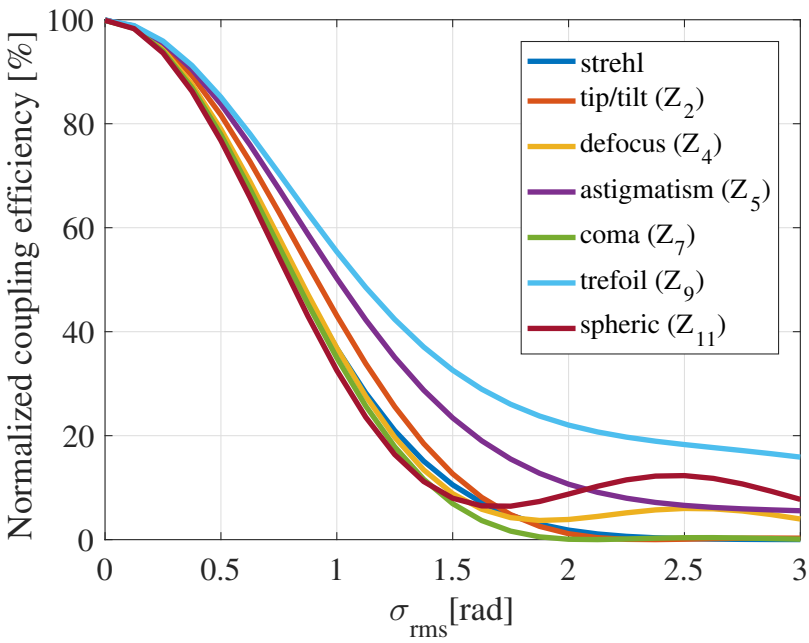

Figure 7.13: Normalized coupling efficiency in function of the wavefront RMS error for different types of aberrations.

7.2 Effect of the obstruction

In Figure 7.14 the coupling efficiency in function of the RMS wavefront error, when a central obstruction α is present, is analysed. It shows that the obstruction has the effect of increasing the strength of some aberrations. Indeed, when $\alpha = 0$ the trefoil is the less affecting aberration. However, when $\alpha = 0.436$ the less affecting aberration seems to be the spherical aberration. The effect of the central obstruction for each aberration is displayed in Figure 7.15. It shows that around $\alpha = 0.4$ the spherical aberration is less dominant than it was for no central obstruction.

In Figure 7.16 the convergence to the diffraction limited case is displayed. It shows that for $\sigma_{rms} \leq 0.1$ the curves are superposed with the ideal case. Therefore, in terms of coupling efficiency the diffraction limited performance is obtained for RMS wavefront error below 0.1 rad.

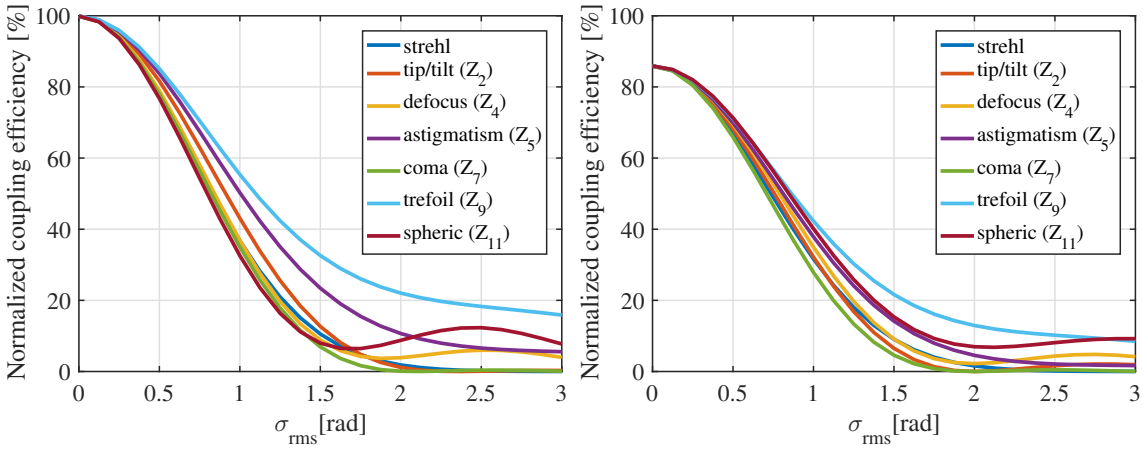

(a) $\alpha = 0$

(b) $\alpha = 0.25$

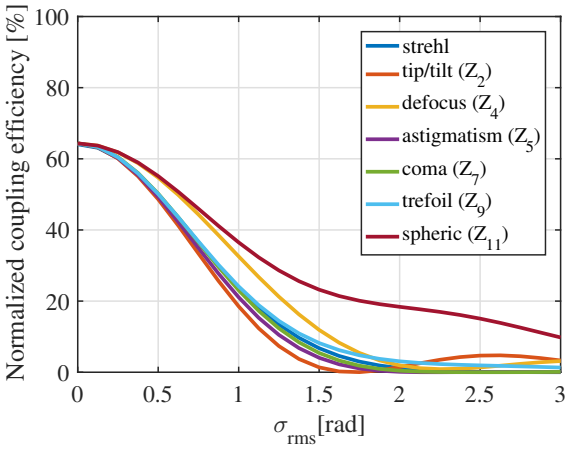

(c) $\alpha = 0.436$.

Figure 7.14: Normalized coupling efficiency in function of the wavefront RMS error for different types of aberrations and different values of the obstruction.

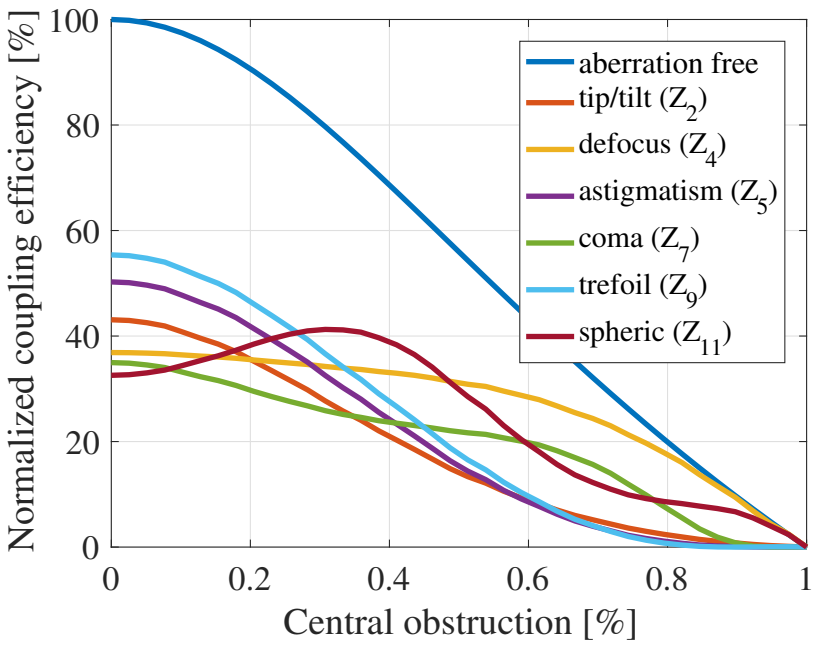

Figure 7.15: Normalized coupling efficiency in function of the central obstruction for different types of aberrations. The strength of the aberration is fixed to 1 rad.

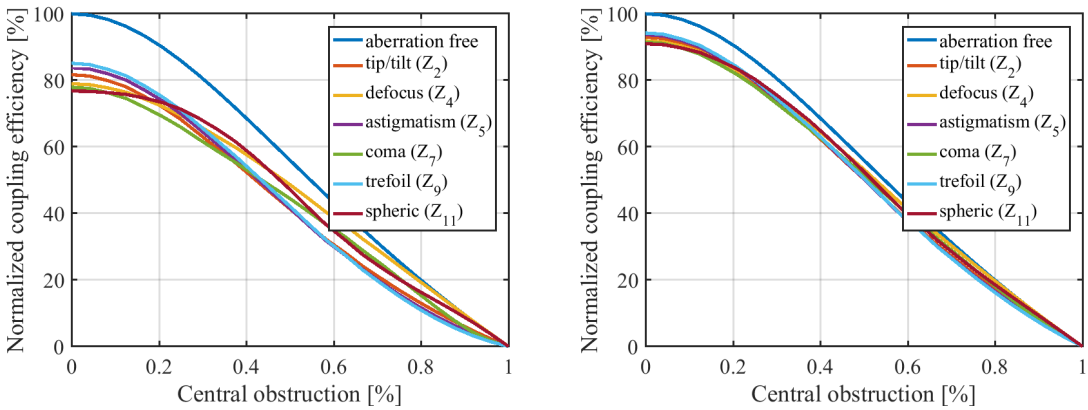

(a) $\sigma_{rms} = 0.5$

(b) $\sigma_{rms} = 0.3$

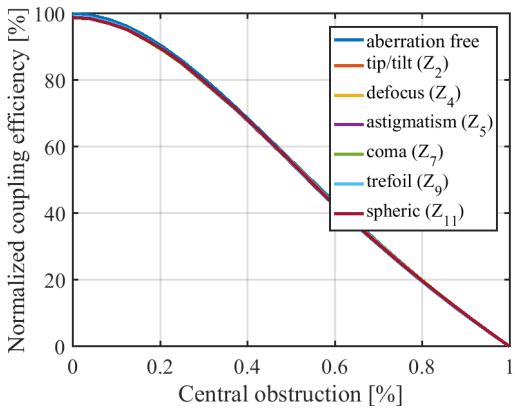

(c) $\sigma_{rms} = 0.1$

Figure 7.16: Normalized coupling efficiency in function of the central obstruction for different types of aberrations and different values of wavefront RMS error.

7.3 Effect of the wavelength

Here the coupling efficiency in function of the wavelength is displayed. The Figure 7.17 shows that with the presence of an aberration the coupling efficiency is no longer maximum at $\lambda = 5\ \mu m$. Indeed, at $\alpha = 0$ and for a trefoil, the coupling efficiency is maximum at $\lambda = 6\ \mu m$. In fact the wavelength where the coupling efficiency is maximum is always bigger than $\lambda = 5\ \mu m$. This effect is less true when σ_{rms} gets smaller. In Figure 7.18 the RMS wavefront error is set to $\sigma_{rms} = 0.5$ rad. It shows the converge towards the diffraction limited case. Also, it can be noticed that the central obstruction flattens the curves.

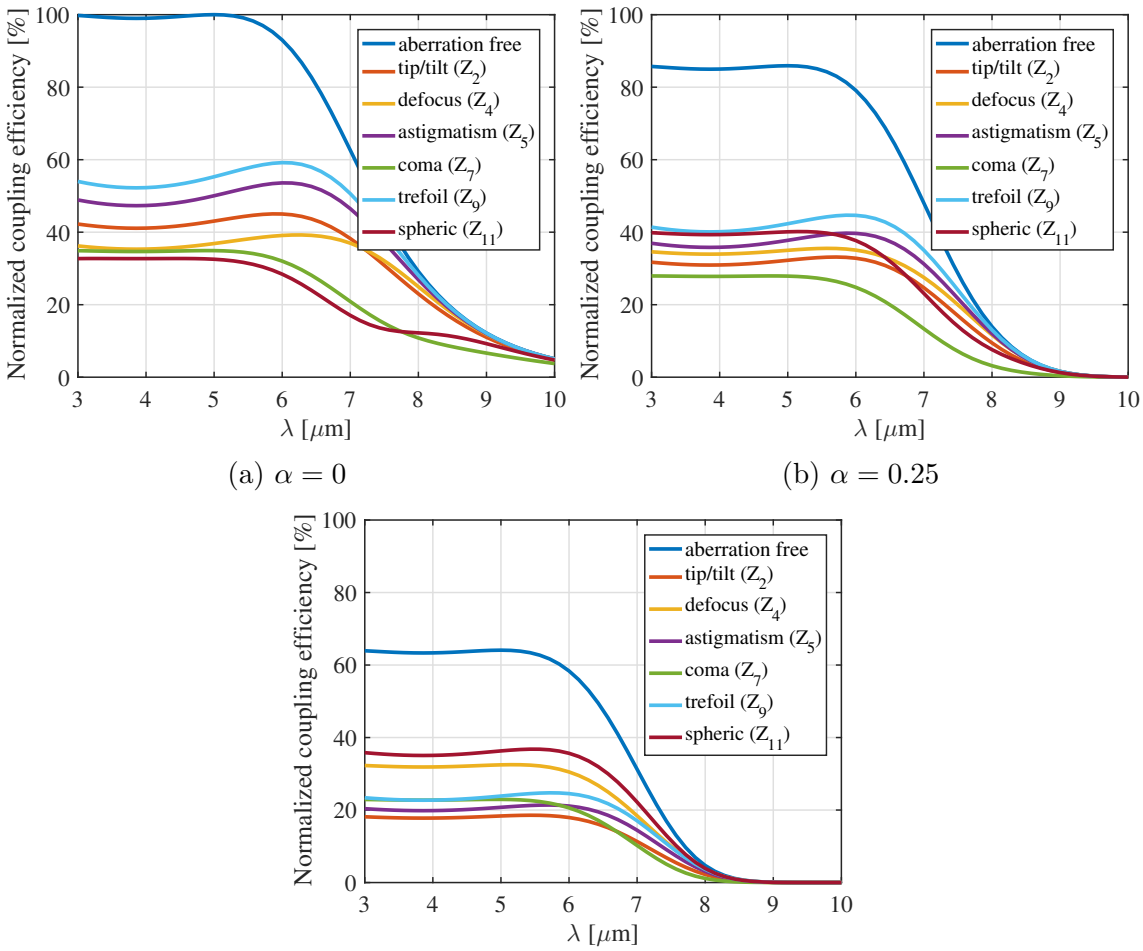

(a) $\alpha = 0$

(b) $\alpha = 0.25$

(c) $\alpha = 0.436$

Figure 7.17: Normalized coupling efficiency in function of the wavelength when $\sigma_{rms} = 1$ rad for different values of the central obstruction.

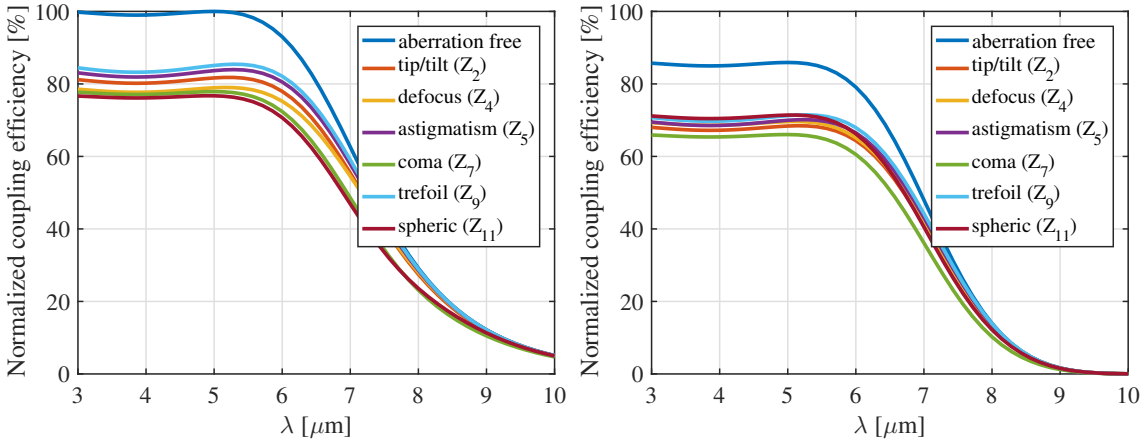

(a) $\alpha = 0$

(b) $\alpha = 0.25$

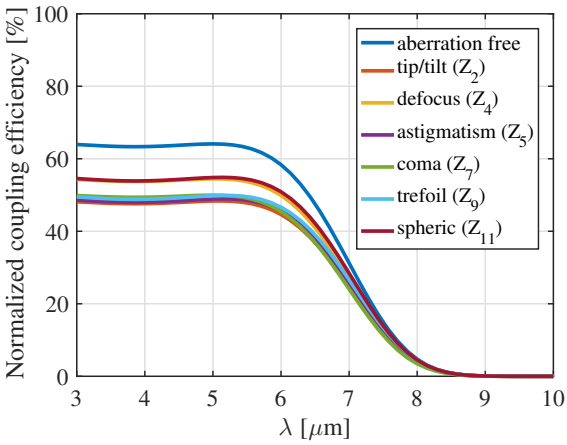

(c) $\alpha = 0.436$

Figure 7.18: Normalized coupling efficiency in function of the wavelength when $\sigma_{rms} = 0.5$ rad for different values of the central obstruction.

7.4 Non-common path aberrations and their correction

Now that single aberrations have been studied the effect of multiple aberrations are considered.

Indeed, any wavefront Φ can be decomposed in the basis of Zernike polynomials

$$\Phi = \sum_{i=1}^{\infty} a_i Z_i(r, \theta) \tag{7.5}$$

To reproduce numerically typical aberrations encountered in space like misalignements, polishing errors or thermal distorsions, the first 120 Zernike polynomials are used. Then their coefficients are randomly generated and divided by their radial order. Such aberrations are known as non common path aberrations (NCPA). An example of such Zernike coefficients distribution is given in Figure 7.19 and the phase map associated is given in Figure 7.20.

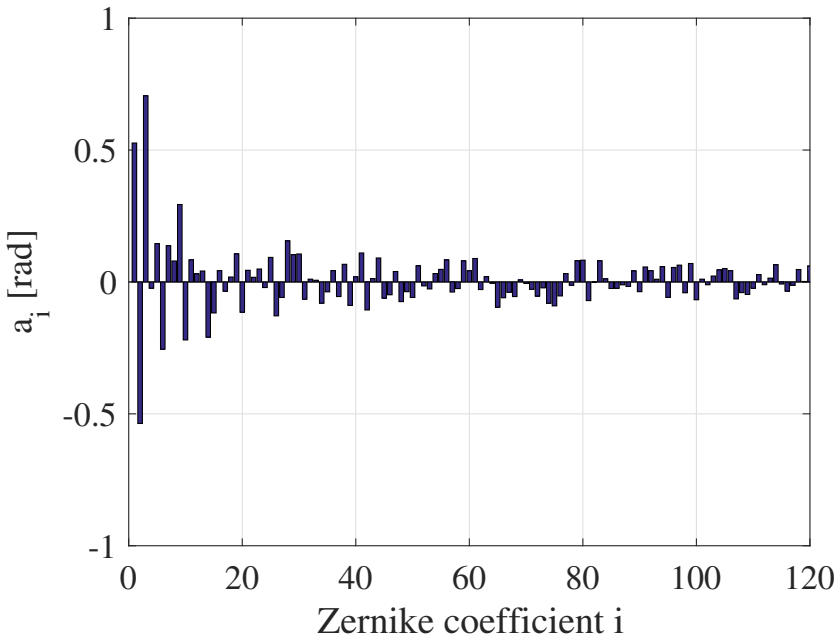

Figure 7.19: Example of randomly generated Zernike coefficients for non common path aberrations.

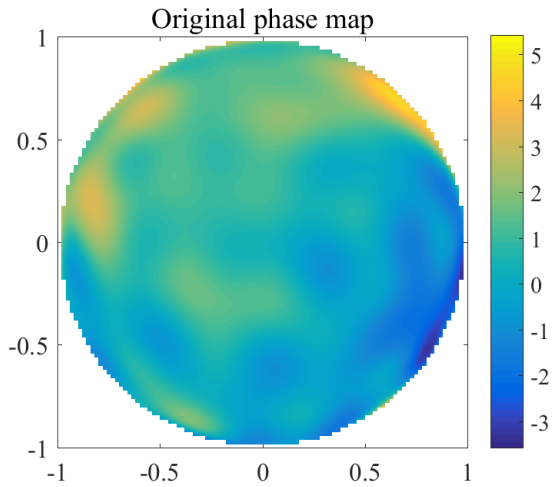

Figure 7.20: Example of phase map for aberrations encountered in space.

Remember that the root mean square for a single aberration is given by its Zernike coefficient while for multiple aberrations it is given by

$$\sigma_{rms} = \sqrt{\sum_{i=1}^{\infty} a_i^2} \tag{7.6}$$

For this phase map the root mean square is $\sigma_{rms} = 1.31$ rad and the coupling efficiency is $\rho = 30$ %. It means that in space, without a system that corrects the aberrations, the coupling efficiency is divided by three. Therefore, in order to have a root mean square less that 0.1 rad, the use of a deformable mirror is mandatory.

The quality of a deformable mirror is measured by its faculty to reproduce Zernike polynomials. Indeed a deformable mirror can reproduce only a finite number of Zernike modes, such that there is always a residual aberration [51]. If the deformable mirror can reproduce perfectly the first N Zernike polynomials, then the residual phase Φ can be expressed by

$$\Phi = \sum_{i=N+1}^{\infty} a_i Z_i(r, \theta) \tag{7.7}$$

In Figure 7.21 the phase maps obtained after corrections of some Zernike polynomials are displayed. It shows that the system needs a deformable mirror capable of reproducing the first 115 Zernike modes in order to get a RMS below 0.1 rad.

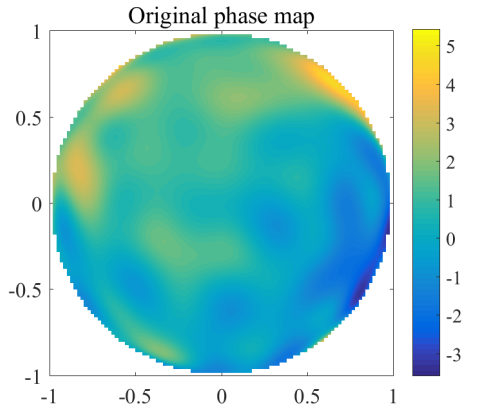

(a) $\sigma_{rms} = 1.31$ rad

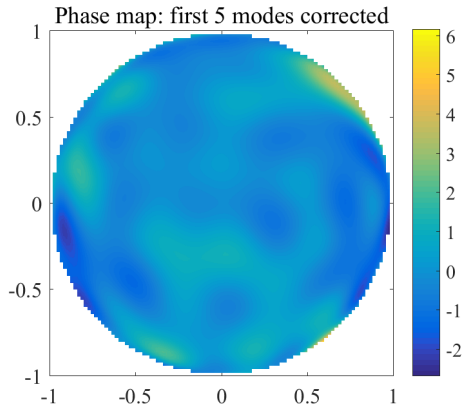

(b) $\sigma_{rms} = 0.8$ rad

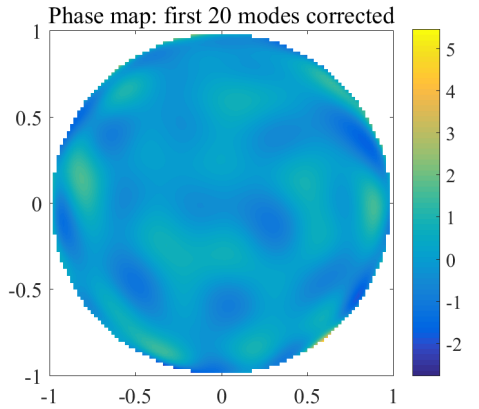

(c) $\sigma_{rms} = 0.57$ rad

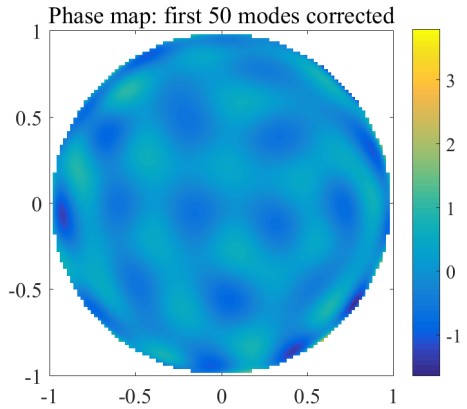

(d) $\sigma_{rms} = 0.4$ rad

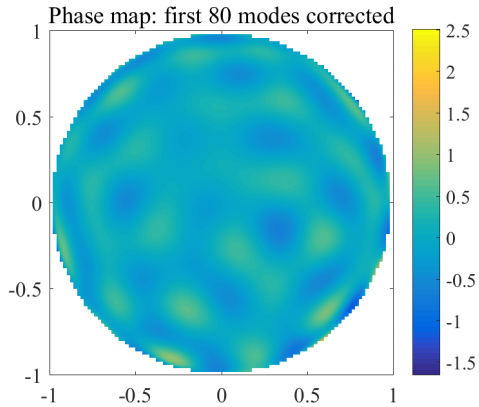

(e) $\sigma_{rms} = 0.27$ rad

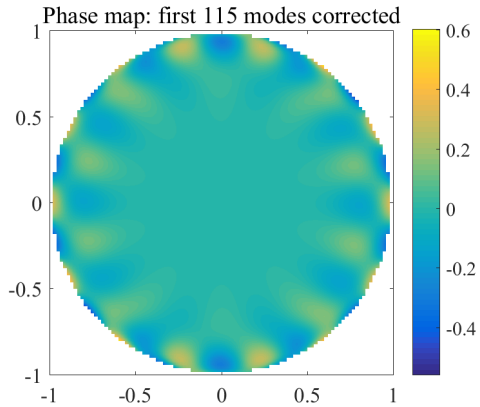

(f) $\sigma_{rms} = 0.086$ rad

Figure 7.21: Residual phase map after correction by a deformable mirror. A RMS wavefront error $\sigma_{rms} < 0.1$ rad is obtained when the first 115 Zernike polynomials are corrected.

Chapter 8

Conclusion

In conclusion, in this master thesis, a mathematical model of the coupling efficiency of a single mode fiber placed at the focus of a telescope was developed. The model is based on the Gaussian approximation of the fundamental mode LP_{01} that is propagated in the single mode fiber. Since the coupling efficiency also depends on the electric field at the input of the fiber, Zernike polynomials are used to describe the aberrations of the incoming light. The study is performed in the waveband $[3-7]$ μm in order to develop a nulling interferometer for exoplanets detections. Guiding principles for designing the telescope/SMF were discussed during the diffraction limited study. Then, the study of static aberrations is performed and the performance of the system for non-common path aberrations and their corrections by a deformable mirror is introduced. The simulations demonstrate the necessity of using a deformable mirror in a space-based nulling interferometer in order to achieve a sufficient wavefront quality. Indeed, the simulations show that, in order to compensate NCPA (first 120 Zernike polynomials), a deformable mirror capable of reproducing the first 115 Zernike polynomials is needed.

Bibliography

[1] M Mayor and D Queloz. "A Jupiter-mass companion to a solar type star". Nature, 378 :355–359, 1995

[2] https://exoplanetarchive.ipac.caltech.edu/exoplanetplots/

[3] D. Defrère et al. "Space-based infrared interferometry to study exoplanetary atmospheres". en. In: Experimental Astronomy 46.3 (Dec. 2018). arXiv: 1801.04150, pp. 543–560. issn: 0922-6435, 1572-9508. doi: 10.1007/s10686- 018 - 9613 - 2.

[4] https://www.gemini.edu/instrumentation/current-instruments/gpi

[5] https://www.amnh.org/research/physical-sciences/astrophysics/research/gemini-planet-imager

[6] http://planetimager.org/

[7] https://www.eso.org/public/teles-instr/paranal-observatory/vlt/vlt-instr/sphere/

[8] Angel, J. Woolf, N.. (2009). "An Imaging Nulling Interferometer to Study Extrasolar Planets". The Astrophysical Journal. 475. 373. 10.1086/303529.

[9] Michael Perryman. "The exoplanet handbook". Cambridge University Press, 2011.

[10] FRIED, D. L. (1965). "Statistics of a Geometric Representation of Wavefront Distortion". Journal of the Optical Society of America. 55 (11): 1427–1435. Bibcode:1965JOSA...55.1427F. doi:10.1364/JOSA.55.001427

[11] Robert J. Noll. Zernike polynomials and atmospheric turbulence. J. Opt. Soc. Am., 66(3):207–211, Mar 1976.

[12] Jean Surdej. "Introduction to optical/IR interferometry". en. In: (), p. 39

[13] https://www.eso.org/sci/facilities/paranal/telescopes/vlti.html

[14] R. N. Bracewell, “Detecting nonsolar planets by spinning infrared interferometer” Nature 418 274(5673), 780 (1978). [doi:10.1038/274780a0]

[15] M. Ollivier and J. M. Mariotti, ”Improvement in the rejection rate of a nulling interferometer by spatial filtering” Appl. Opt. 36, 5340–5346 (1997).

[16] O. P. Lay, ”Systematic Errors in Nulling Interferometers”. Appl Opt, 43:6100-6123, novembre 2004.

[17] Absil, Olivier. (2006). ”Astrophysical studies of extrasolar planetary systems using infrared interferometric techniques”.

[18] M. Ollivier, ”Contribution à la recherche d’exoplanetes. Coronographie interférentielle pour la mission DARWIN”, Ph.D. thesis (Université de Paris XI, Orsay, 1999).

[19] Mennesson, B., Ollivier, M. and Ruilier, C., J. Opt. Soc. Am. A 19, 596 (2002)

[20] A. Sommerfeld. Optics, volume IV of Lectures on Theoretical Physics. Academic Press, New York, NY, 1954

[21] Allan, Gregory Douglas, Ewan Egan, Mark Furesz, Gabor Grunwald, Warren Gubner, Jennifer do Vale Pereira, Paula Stein, Abigail Cahoy, Kerri. (2018). ”The Deformable Mirror Demonstration Mission (DeMi) CubeSat: optomechanical design validation and laboratory calibration.”

[22] J. Loicq et D. Defrere : Space optics, chapter 4 : Space interferometry. Notes de cours, 2020

[23] Masen Lamb, David R. Andersen, Jean-Pierre Véran, Carlos Correia, Glen Herriot, Matthias Rosensteiner, and Jason Fiege. ”Non-common path aberration corrections for current and future ao systems.” volume 9148, page 914857, 07 2014

[24] http://www.bostonmicromachines.com/low-actuator-count.html

[25] Douglas, E. S., Mendillo, C. B., Cook, T. A., Cahoy, K. L., and Chakrabarti, S., ”Wavefront sensing in space : flight demonstration II of the PICTURE sounding rocket payload,” 4(1) (2018)

[26] Mendillo, Christopher Hicks, Brian Cook, Timothy Bifano, Thomas Content, David Lane, Benjamin Levine, Bruce Rabin, Douglas Rao, Shanti Samuele, Rocco Schmidtlin, Edouard Shao, Michael Wallace, James Chakrabarti, Supriya. (2012). "PICTURE: A sounding rocket experiment for direct imaging of an extra-solar planetary environment." Proceedings of SPIE - The International Society for Optical Engineering. 8442. 10.1117/12.926408.

[27] Madec, P.-Y. "Overview of deformable mirror technologies for adaptive optics and astronomy." In SPIE Astronomical Telescopes+ Instrumentation, pages 844705–844705. International Society for Optics and Photonics, 2012.

[28] Cousty, Raphaël Antonini, Tania Moreau, Aurélien Krol, Hélène Aubry, Marie. (2017). "Monomorph deformable mirrors: from ground-based facilities to space telescopes." 291. 10.1117/12.2296247.

[29] Wang, Yukun Xu, Huanyu Li, Dayu Wang, Rui Jin, Chengbin Yin, Xianghui Gao, Shijie Mu, Quanquan Xuan, li Cao, Zhaoliang. (2018). "Performance analysis of an adaptive optics system for free-space optics communication through atmospheric turbulence." Scientific Reports. 8. 10.1038/s41598-018-19559-9.

[30] Born and Wolf, "Principles of Optics", 1993

[31] E.-G. Neumann, "Single-Mode Fibers", Springer-Verlag, Berlin 1988

[32] Di Bartolomeo Samuel, "Master thesis : Mission analysis of an interferometric small-Sat to observe exoplanets", 2019

[33] https://www.rp-photonics.com/numerical_aperture.html

[34] https://www.rp-photonics.com/lp_modes.html

[35] https://www.newport.com/t/fiber-optic-basics

[36] https://www.rp-photonics.com/fibers.html

[37] https://www.rp-photonics.com/fluoride_fibers.html

[38] A. W. Snyder and J. D. Love, "Optical Waveguide Theory, Chapman and Hall", London (1983)

[39] D. Gloge, "Weakly guiding fibers", Appl. Opt. 10 (10), 2252 (1971), doi:10.1364/AO.10.002252

[40] Snyder A.W.: "Asymptotic expressions for eigenfunctions and eigenvalues of a dielectric or optical waveguide." IEEE Trans. MTT-11, 1130-1138, 1969

Marcuse D.: "Gaussian approximation of the fundamental modes of graded-index fibers." J. Opt. Soc. Am. 68, 103-109, 1978

Abramowitz M., Stegun LA.: "Handbook of Mathematical Functions." (Dover Pub!., New York), 1965

[41] https://questtel.com/wiki/numerical-aperture-in-fiber-optics

[42] https://www.sukhamburg.com/support/technotes/fiberoptics/cablebasics/NAeff.html

[43] C. Ruilier," A study of degraded light coupling into singlemode fibers, in Astronomical Interferometry, R. D. Reasenberg", eds., Proc. SPIE 3350, 319–327 (1998).

[44] Wallner, Oswald Winzer, Peter Leeb, Walter. (2002). "Alignment Tolerances for Plane-Wave to Single-Mode Fiber Coupling and Their Mitigation by Use of Pigtailed Collimators." Applied optics. 41. 637-43. 10.1364/AO.41.000637.

[45] S. Shaklan and F. Roddier, "Coupling starlight into singlemode fiber optics", Appl. Opt. 27, 2234–2338 (1988).

[46] Serabyn, E., 2000, "Nulling interferometry: symmetry requirements and experimental results", in Interferometry in Optical Astronomy (P. Léna A. Quirrenbach, eds.), Proc. SPIE, vol. 4006, 328–339.

V. N. Mahajan, "Strehl ratio for primary aberrations in terms of their aberration variance," J. Opt. Soc. Am. 73, 240–241 (1983).

[47] V. N. Mahajan, Zernike Polynomials and Beyond "Introduction to Aberrations", Zernike Lecture 12 April 12, College of Optical Sciences, University of Arizona

[48] Roddier, F. (Ed.). (1999). "Adaptive Optics in Astronomy." Cambridge: Cambridge University Press. doi:10.1017/CBO9780511525179

Robert Tyson, "Principles of Adaptive Optics" (Series in Optics and Optoelectronics), 3rd edn., 2011

[49] David Voelz. "Computational Fourier Optics." SPIE, Bellingham, Washington USA, 2011.

[50] J. W. Goodman. "Introduction to Fourier Optics." Toberts Company, Greenwood Village, CO, 2005.

[51] Schmidt, Jason D.. "Numerical Simulation of Optical Wave Propagation With Examples in MATLAB." (2010).

[52] Bechter, Andrew Crass, Jonathan Tesch, Jonathan Crepp, Justin Bechter, Eric. (2020). "Characterization of Single-Mode Fiber Coupling at the Large Binocular Telescope."

[53] Defrere, Denis, Absil, Olivier Foresto, V. Danchi, W. den Hartog, Roland. (2008). Nulling interferometry: "Performance comparison between space and ground-based sites for exozodiacal disc detection." Astronomy and Astrophysics. 490. 10.1051/0004-6361:200810248.

[54] Coudé du Foresto, V., Faucherre, M., Hubin, N., Gitton, P. 2000. "Using single-mode fibers to monitor fast Strehl ratio fluctuations." Application to a 3.6 m telescope corrected by adaptive optics. Astronomy and Astrophysics Supplement Series 145, 305–310.

[55] Tatiana Latychevskaia, "Lateral and axial resolution criteria in incoherent and coherent optics and holography, near- and far-field regimes," Appl. Opt. 58, 3597-3603 (2019)

[56] Matijevich, R., Johansson, E., Johnson, L., Cavaco, J., National Solar Observatory 2016, AAS Meet. Abstracts, 227, 146.21

[57] Buddy Nelson et all (Lockheed), "Hubble Space Telescope : Servicing Mission 4 Media Reference Guid", NASA, 2009, 132 p

[58] Colin Dandumont. "Feasibility study of an interferometric CubeSat for exoplanet science". en. In: (), p. 33.

[59] Arthur Scheffer, "Study of thermomecanical constraints on optical performances for an Interferometric Small Sat.", 2020

[60] Colin Dandumont, Denis Defrère, Jens Kammerer, Olivier Absil, Sascha P. Quanz Jérôme Loicq, "Exoplanet detection yield of a space-based Bracewell interferometer, from small to medium satellites.",(in press), 2020